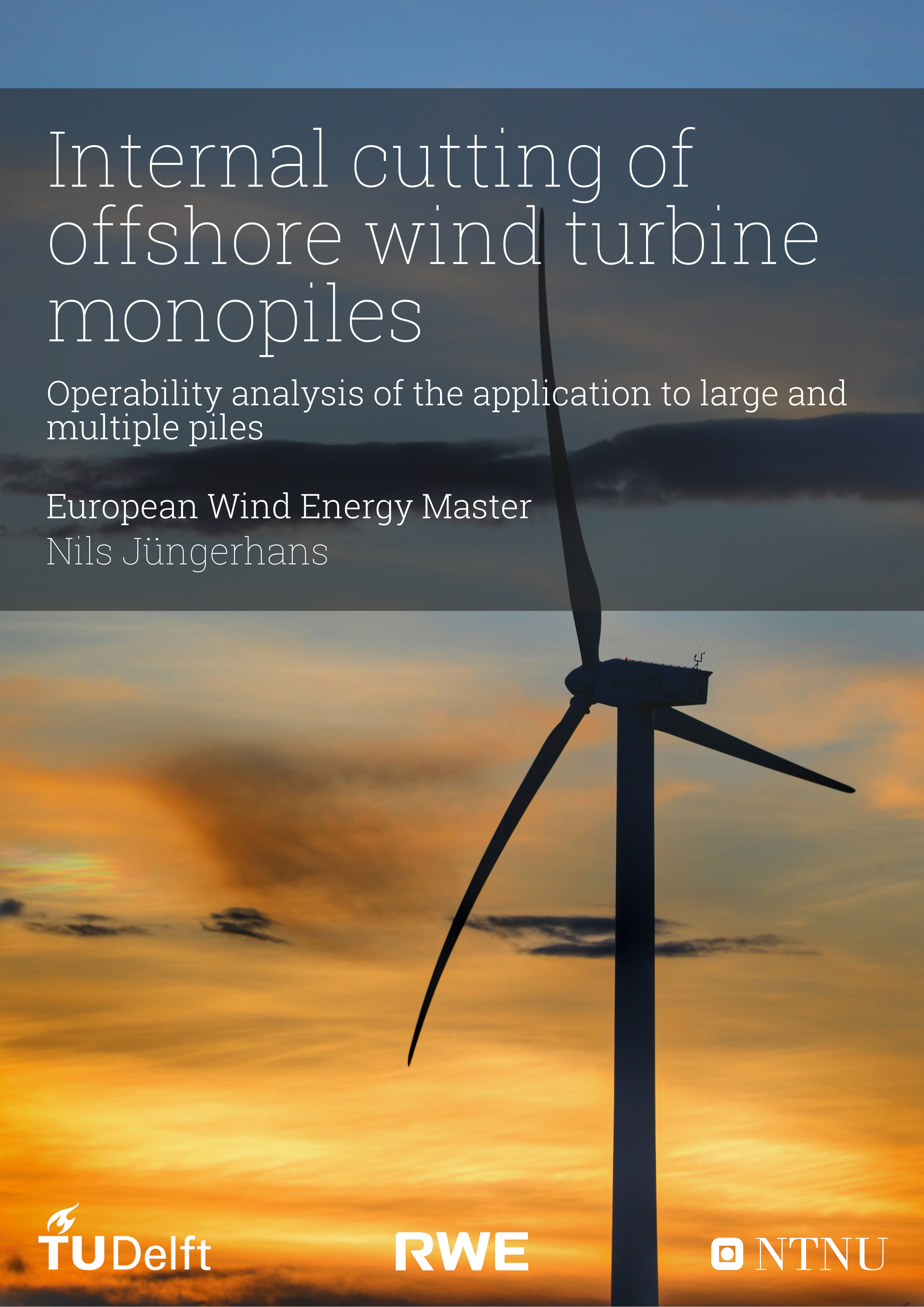

Internal cutting of offshore wind turbine monopiles

Operability analysis of the application to large and multiple piles

European Wind Energy Master

Nils Jüngerhans

TU Delft RWE NTNU

Internal cutting of offshore wind turbine monopiles

Operability analysis of the application to large and multiple piles

by

Nils Jüngerhans

to obtain the degrees

Master of Science
in Offshore Engineering
at the Delft University of Technology

&

Master of Science
in Technology - Wind Energy
at the Norwegian University of Science and Technology

To be defended publicly on Monday, the 19th of August 2024

TU Delft chair:	Pim van der Male
TU Delft supervisor:	Jeroen Hoving
NTNU supervisor:	Bernt Johan Leira
RWE supervisor:	Benjamin Haak

Cover: White windmill during daytime - Photo by Dev Kalidhasan on Unsplash

Abstract

Offshore wind energy is considered one of the most promising solutions for sustainably meeting the society's growing energy needs. This is why there are major construction projects and massive expansion plans for new offshore wind farms worldwide. In the North Sea in particular, the technology has been used to generate electricity for several years. Looking at the oldest wind farms still in operation, it will soon be time to decommission them once the turbines have reached their service life of 20 to 25 years. However, especially the removal of the foundations is considered challenging because not many comparable projects have already been realised. The most commonly used type of foundation is the monopile due to its simplicity. During installation, these long steel piles are driven deep into the seabed to provide a secure foundation over the entire service life. One option for decommissioning is to cut the piles from the inside a few metres below the seabed and then pull them out. So far, this procedure has mainly been used for individual small piles. Scaling up to several large monopiles of a wind farm involves uncertainties. On the one hand, it is unclear how larger monopiles will behave during the cutting process, and on the other hand, the operational performance of several piles that are removed one after the other is uncertain.

When cutting monopiles, theoretically no complete cutting progress can be achieved because the pile breaks off beforehand. In this work, a calculation model was developed that predicts the cutting progress at which a monopile fails due to the hydrodynamic forces acting on it. Based on an existing project in which the internal cutting technology was used, a minimum progress was defined that must be reached before failure is allowed to occur. This makes it possible to determine which sea states are permissible in order to achieve the specified cutting progress. With the calculation model, a parameter study was carried out to find out which structural and environmental parameters have the greatest influence on failure. Additionally, two real wind farms were considered as case studies to investigate realistic parameter sets. One of these wind farms has relatively small monopiles as foundations, while the other has much larger ones. An operability analysis was also carried out for these case studies in order to determine the duration of the foundation decommissioning operation and to be able to analyse the weather downtime. In addition to calculating when a monopile fails during the cutting process, the forces required to pull the pile out of the seabed afterwards were calculated. This allows to determine the required crane capacity of the working vessels used for the operation.

The results of the calculations show that larger monopiles fail at an earlier cutting process than smaller monopiles. However, this difference is not large, which is due to the fact that together with the hydrodynamic forces, which increase with the pile size and length, also the wall thicknesses increase. This means that larger forces can generally be withstood. The operability is good for both wind farms from the case studies. Furthermore, it was found that it is important for the operability how the connection between monopile and transition piece was realised and whether ROVs have to be used. The crane capacity of the vessels used can be lower than that of the vessels used during installation. The additional force required to pull the monopiles out of the seabed does not make up for the weight lost by leaving a large part of the foundation in the soil.

Preface

This master's thesis was written as part of the Offshore Engineering specialisation of the European Wind Energy Master (EWEM). It is the final assessment before two master's degrees are awarded: A Master of Science in Offshore Engineering by TU Delft and a Master of Science in Technology - Wind Energy by NTNU Trondheim. This thesis was written in co-operation with RWE Offshore Wind GmbH in Hamburg.

I would first like to thank my supervisors from TU Delft and NTNU Trondheim. Jeroen, I would like to thank you for stepping into the role of my main supervisor. In addition, you always steered me in the right direction regarding the research questions and provided valuable feedback during our meetings. Bernt, thank you for acting as the supervisor from the NTNU side. You also gave me constructive feedback in our progress meetings, not only during the master's thesis, but even before that during the project work in Trondheim. Pim, thank you for taking on the role of the chairman and thus completing my graduation committee. Alongside my two university supervisors, you also participated in the progress meetings and gave me useful feedback. In general, even though we were working from three different countries and therefore had to meet online, the meetings with the three of you were always enjoyable and helped me a lot in terms of content.

I would also like to thank my colleagues at RWE, especially the logistics department, where I was employed. You helped me a lot when I was writing my thesis, as you were there to give me advice on any questions I had. In addition, there was a great collegial atmosphere in the office and I was always happy to meet you there, chat during our lunch breaks or get to know you better at team-building events. Special thanks go to Benny for taking on the role of the supervisor from the company side. You made the work on this topic possible in the first place, gave me additional constructive feedback and dealt with all the organisational work.

I made a lot of new friends during my studies and even lived together with some of them during my last semester in Trondheim. We all faced the challenges of a master's degree and spent quite some time together, be it during project work or in our free time. I would like to thank each and every one of you for making this an unforgettable time and wish you all the best for the future.

Finally, I would like to thank my parents. Even though I was only home a few times during my studies, you were always my biggest supporters and helped me on my way. Without your support, understanding and financial assistance, none of this would have been possible. I am very grateful to have you.

Nils Jüngerhans
Hamburg, July 2024

Contents

List of Figures

List of Tables

Nomenclature

Abbreviations

Abbreviation	Definition
ASWJ	Abrasive suspension water jet
BEIS	Department for business, energy & industrial strategy
BSH	Bundesamt für Seeschifffahrt und Hydrographie
CAPEX	Capital expenditure
CAD	Computer-aided design
CD	Chart datum
CRFP	Carbon reinforced fiber polymer
DNV	Det Norske Veritas
DP	Dynamic positioning
FEM	Finite element method
GHG	Greenhouse gas
GRFP	Glass reinforced fiber polymer
HAT	Highest astronomical tide
IMO	International maritime organization
JONSWAP	Joint North Sea Wave Observation Project
LAT	Lowest astronomical tide
MHWN	Mean high water neaps
MLWN	Mean low water neaps
MHWS	Mean high water springs
MLWS	Mean low water springs
MSL	Mean sea level
OPEX	Operational expenditure
OWF	Offshore wind farm
OWT	Offshore wind turbine
P50	50% probability of non-exceedance
P75	75% probability of non-exceedance
P90	90% probability of non-exceedance
ROV	Remotely operated vehicle
RP	Recommended practice
RRE	Robin Rigg East
RRW	Robin Rigg West
SP	Scour protection
WDTX	Weather downtime express (ABPmer)
WTG	Wind turbine generator
WTIV	Wind turbine installation vessel

1

Introduction

This chapter introduces the general topic of offshore wind energy, followed by an explanation of what happens at the end of a wind farm’s life cycle. It describes the arising problems at this final stage and concludes with an overview of the thesis.

1.1. Offshore wind energy - why and how?

In 2015, the United Nations adopted the Paris Climate Agreement. The signatory states thereby undertake to counter the threats posed by the climate change. The main goal of the agreement is to limit the increase in the average global temperature to a maximum of 2 °C (in the best case 1.5 °C). The reference value for this is the pre-industrial temperature level [1]. One of the most important measures for achieving the target is to reduce greenhouse gas (GHG) emissions. This requires the expansion of renewable energies, with environmentally friendly offshore wind energy coming into play [2]. In Figure 1.1, it can be seen that alone in 2023 more than 3.7 GW of offshore wind energy has been installed in Europe.

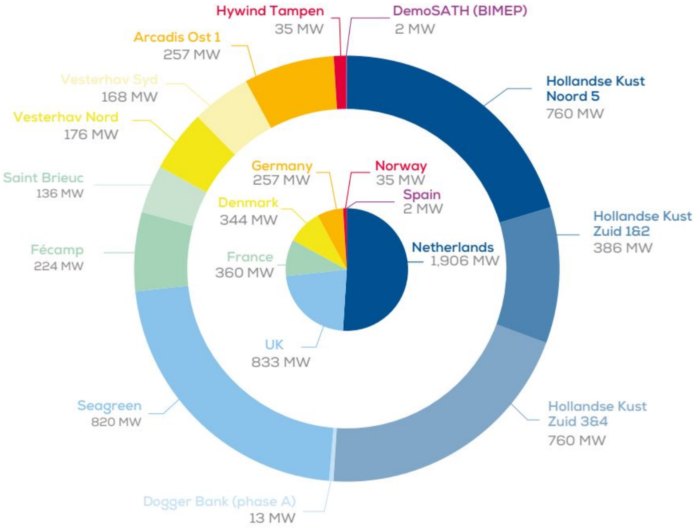

Figure 1.1: New offshore wind farms in Europe in 2023.

Source: [3]

These numbers show that the industry recognized the potential of offshore wind energy and is taking action. And there are good reasons for doing so: According to a report from WindEurope, between 2,600 TWh and 6,000 TWh of electricity per year could be generated economically competitive using offshore wind energy in Europe. This would be between 80% and 180% of the EU's annual electricity consumption [4]. Further reasons in favour of offshore wind energy become evident when compared with its onshore counterpart. Onshore, noise pollution and disfigurement of the landscape result in a lack of acceptance of wind turbines. Offshore, these problems hardly occur as the turbines are not located near people. In addition, the availability of more space offers the opportunity for larger projects. The turbines that can be built offshore are much larger compared to onshore turbines. And finally, the higher wind speeds at sea increase the amount of energy that can be generated per turbine [5]. The development of new and larger turbines is also continuing. In 2023, the average installed turbine size was 9.7 MW offshore and 4.5 MW onshore. This shows an annual increase, as these sizes were still 8 MW offshore and 4.1 MW onshore in 2022 [3].

The successful operation of an offshore wind farm (OWF) throughout its entire life cycle is ensured by many different components. The main parts of an offshore wind turbine (OWT) are the wind turbine generator (WTG), the substructure/foundation, the transition piece connecting the WTG with the foundation and the cables for power transmission. OWTs are often classified according to the type of substructure, as most variation can be observed here. An overview of three OWTs with different foundation types is given in Figure 1.2.

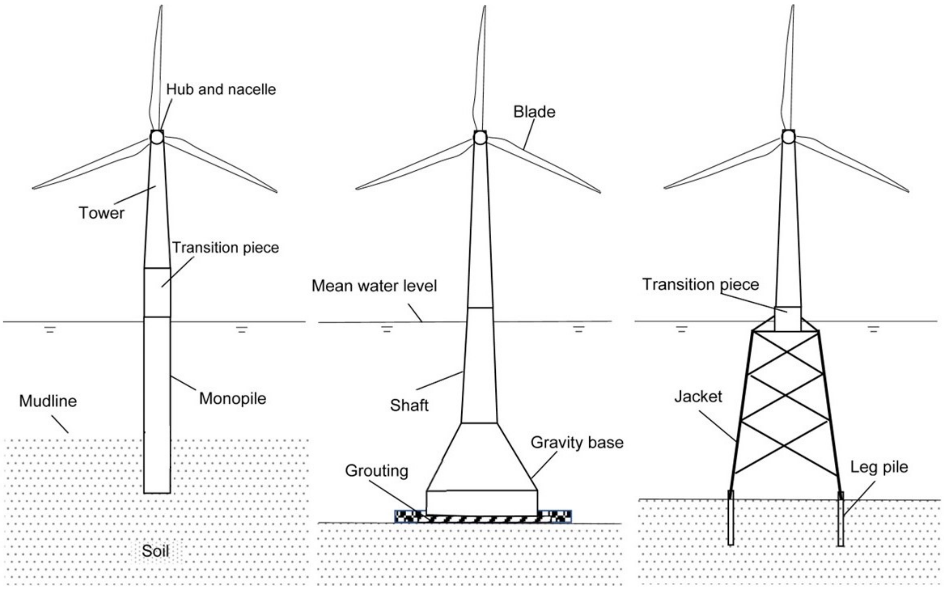

Figure 1.2: Schematic of monopile, gravity-based and jacket offshore wind turbines.

Source: [6]

The three foundation types shown are the monopile, the gravity-based foundation and the jacket. Monopiles and jackets require the piles to be driven into the seabed, while gravity foundations are not driven but simply placed on the ground. On any substructure, regardless of type, a transition piece is usually used to connect the foundation to the turbine tower. The connection between the foundation and the transition piece can be either bolted or grouted, while the connection to the tower is typically bolted. The hub and the nacelle are located at the top of the turbine tower. The hub connects the blades to the main shaft in the nacelle, where the rotational energy is converted into electricity via the generator. A gearbox is often used between the main shaft and the generator. The electricity from the generator is then transmitted via the cables to a converter station. Another important OWT component that is not shown in Figure 1.2 is the scour protection at the mudline. This is required to limit the subsidence of the seabed surrounding the foundation [7].

This thesis focuses on the foundations only, more precisely only on monopiles, as it is by far the most used foundation. According to 2023 statistics from WindEurope, monopiles make up 78% of installed foundations. Further statistical information can be seen in Figure 1.3.

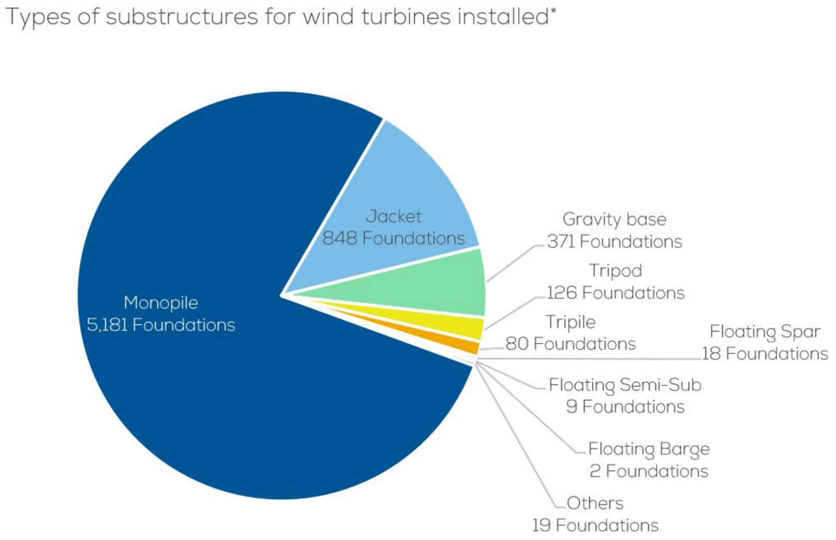

Figure 1.3: Number of foundations grid-connected by substructure type by end of 2023.

Source: [8]

The reason for the success of monopiles lies in the simplicity of their design, which makes them very cost-effective. As can be seen in Figure 1.2, monopiles are long piles made of steel. This design allows for mass production and robustness in most soil conditions [9]. The diameter of installed monopiles typically ranges from 3 m to 8 m, increasing with turbine size and deeper waters. The water depth is also the main limiting factor for the use of monopiles, as they have long been considered effective only in shallow waters up to 35 m. However, new calculations show that XL-monopiles with diameters greater than 9 m can be used for significantly deeper waters [10].

1.2. End-of-life of offshore wind farms

OWFs are usually designed for an operational life of 20 - 25 years. After this period, there are three options how to continue. The first one would be to extend the operational life. As part of the life extension, only the most critical worn components of the WTG are replaced. This reduces maintenance costs for the period after the actual service life. In other words, further operating expenditure (OPEX) can be reduced with relatively low capital expenditure (CAPEX). In addition, wind turbines built more than a decade ago were designed with more conservative safety coefficients than those of today. The probability that their service life can be extended is therefore reasonably high. [11]

The second option would be repowering which is based on the assumption that the substructures, cables and substations have a longer service life than the turbines [12]. The idea is to reuse the components, which still have a remaining useful life, and only replace the turbines, i.e. partial repowering. However, a complete repowering of all components could also be an option [13].

If extending the service life or repowering is not considered an attractive option, or if these measures have already been completed, an OWF must ultimately be decommissioned. The rest of the section focuses exclusively on this part of the end-of-life phase.

When decommissioning a wind farm, the site is to be left in as similar conditions as possible to those that existed before the farm was built. According to the Energy Act from 2004, this shall be achieved by adhering to the ”polluter pays” principle. This means that the companies to develop and own an offshore wind farm are responsible for covering the costs to decommission the construction and mitigate arising risks [14]. This applies at least to OWFs in the waters of the United Kingdom and Wales. The general rules may vary, so the entire section section 2.2 will provide an overview of the regulatory framework for decommissioning OWFs.

One of the reasons why the regulations are not yet completely clear is the lack of experience in the field of decommissioning. Figure 1.4 shows the number of OWTs reaching 20 years in operation each year from 2015 to 2040. As can be seen, only a few turbines have reached this mark so far (2024), compared to the numbers at the end of the decade. Also, from these turbines only a limited numbers has been decommissioned underlining the lack of experience. The few earlier carried out decommissioning projects will be discussed in subsection 2.1.3.

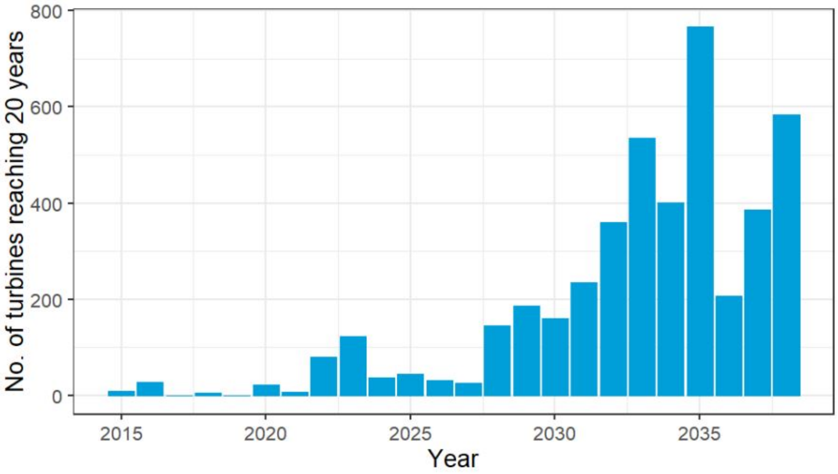

Figure 1.4: Number of offshore wind turbines reaching 20-years of operation annually in Europe.

Source: [15, 16]

However, as the number of turbines reaching the end of their service life by 2030 and beyond is increasing rapidly, decommissioning will become more important in the next years. In the 2030s, it must be carried out frequently and become a routine procedure like maintenance. It is therefore urgently necessary for developers to investigate decommissioning and start planning these projects. [15]

1.3. Thesis overview

In this section, the relevance of the work will be explained. To this end, the problem and the research objectives are presented, followed by an outline of the chapters.

1.3.1. Problem

Offshore wind farm decommissioning, especially of monopile foundations, is expected to pose considerable challenges in the coming years. Unlike WTGs, which can be dismantled in reverse order of installation, this is not the case for monopiles. Here, decommissioning is complicated by unclear legislation and a lack of guidance on the best technology for removing monopiles from the seabed. Internal water cutting of the foundations is seen as a possible solution to this problem, but the application of this technique is associated with challenges. The proposed method has only been used in small diameter piles associated to the oil and gas industry or meteorological masts. As scaling up the tools to be able to cut WTG monopiles with larger diameter is theoretically possible, it is not known how the operational performance is affected by larger piles. Next to scaling up the sizes of the structures, also the number of foundations to be removed has to go up when whole wind farms shall be decommissioned. Due to the upscaling to larger monopiles and the removal of several piles in succession, there are knowledge gaps that are to be filled with this work.

1.3.2. Research objectives

This thesis investigates the operability of decommissioning WTG monopiles by internal cutting. The ultimate goal is to create and analyse schedules for the successful decommissioning of monopiles from entire wind farms. To do so, the following research questions will be answered in the course of the work:

- What is the current state of monopile decommissioning and how is it regulated in Germany and the UK?

- How do the cutting tools work and what is important when decommissioning multiple monopiles?
- When in the cutting process do WTG monopiles lose their stability and fail?
- What crane capacities are required for successful monopile removal from the seabed after cutting?
- What parameters have the most influence on the monopile's stability during cutting and on the extraction hook loads?
- What schedules can be expected for the decommissioning of monopiles and what role does the cutting operation play in this?

Explicit answers to these questions are provided in section 6.2 in the concluding chapter.

1.3.3. Thesis outline

The scope of the thesis initially comprises a literature study in chapter 2, in which previously completed decommissioning projects, regulatory aspects, the decommissioning operation, water cutting technology and the recycling of components are considered. The projects that have already been carried out include foundations from the oil and gas sector, from meteorological masts and from old wind farms that have been decommissioned. The regulatory aspects are first described in general and then separately for Germany and the UK. The general procedure for decommissioning operations and how water cutting works are then explained. The section on recycling is intended to briefly show the potential and difficulties that arise when wind turbine components are reused.

In chapter 3, the calculations carried out are explained. This begins with the hydrodynamic calculations, which result in the loads on the monopile. This is followed by a description of the stress calculation in the cut and the calculation of the necessary crane capacities when the piles are subsequently lifted. In order to be able to analyse the operability, limits are set for the operation that must not be exceeded. The modelling software for the decommissioning schedules is then presented. The chapter ends with an overview of the simulations that are performed.

In chapter 4, the model is validated using a monopile decommissioning project that has already been carried out. To do this, the parameters of the completed project are entered into the model and the simulation results are compared with the real results. A parameter study is then carried out to visualise the parameters that have the greatest influence on the calculations. The chapter concludes with a first detailed discussion of the results obtained so far and the assumptions made.

In chapter 5, two case studies are then described and subsequently analysed using the calculation models. This gives an impression of the behaviour of the calculations with real parameter sets. For the case studies, in addition to the stress and extraction force calculations, the schedules for the decommissioning of their monopiles are also determined. These are examined in detail in order to visualise the influences of the various operations. The chapter concludes with a second discussion in which the new findings from the results of the case studies and the analysis of the decommissioning plans are addressed.

The thesis concludes with chapter 6. It summarises the works carried out once again and then presents the main results of the thesis. This is done in the form of explicit answers to the research questions listed above. The final section gives an indication of how the topic could be taken forward and what future work should focus on.

2

Offshore wind farm decommissioning

This chapter considers different aspects of the decommissioning of OWFs. Firstly, experience with decommissioning in the marine industry is described and previous projects are analysed. Then, the legal framework for the decommissioning process is reviewed. The main part of this chapter consists of a generalized description of the decommissioning operation with an extra section explaining the abrasive suspension water jet (ASWJ) cutting method. It concludes with a review of the recycling potential of the components.

2.1. Experience and earlier projects

This section considers decommissioning in the oil and gas sector, meteorological mast (met mast) removal and OWF decommissioning programmes that have already been successfully completed and provides an overview of potential learnings for future action.

2.1.1. Oil and gas industry

As the oil and gas industry predates the offshore wind sector, there are learnings that can be transferred. Smith and Lamont [17] have compared both industries and found similarities and differences in the decommissioning of their respective structures:

The most important technical similarities between the two sectors are the foundation types and the site conditions. Monopiles, jackets and gravity-based foundations are used in both, the oil and gas sector and the offshore wind industry. In addition, both have to deal with difficult conditions in terms of sea, weather and seabed. A large part of the marine experience gained therefore applies to both sectors. However, in the wind industry generally many smaller and lighter structures are used in comparison to the oil and gas sector. The latter usually involves individual but very large and heavy topside platforms. The vessels used will therefore differ at least in terms of their size and crane capacity. The underwater cutting methods used to date mostly in the oil and gas sector are also transferable to the offshore wind industry. However, due to the larger diameters of the wind turbine monopiles, adjustments must be made and larger tools used. In order to minimise the need for divers, the use of remotely operated vehicles (ROVs) can also be transferred from the oil and gas sector to the wind sector. Two advantages that ease the decommissioning of offshore wind farms are the significantly lower risk of hazards and pollution from hydrocarbon residues and the generally shallower water depths. This is due to the fact that OWFs are usually constructed closer to the shore than oil and gas platforms. [17]

2.1.2. Meteorological masts

Other offshore structures that are similar to WTG monopiles and have been decommissioned successfully already are met masts. Met masts are erected to collect live data on the wind/wave climate at a specific location offshore. In the following, the decommissioning operation of the met mast associated to Amrumbank West OWF shall be considered.

The operation was carried out by E.ON Climate and Renewables GmbH in January 2016 [18]. The MPI

Adventure jack-up vessel was hired and the work took a total of 10 days. The met mast was supported by a monopile and it was decided to cut the pile below seabed using an ASWJ cutter. Before the monopile could be removed from the seabed, the lattice tower had to be dismantled and the sand inside the pile had to be dredged out. After the preparations were completed the monopile was cut internally 2.8 m below the seabed. During the whole time the crane was attached but only taking 80% of the weight to not additionally pull on the pile. For the cutting and removal operation the wave limit was set to 2 m. The diameter of the monopile at the cutting depth was 3.5 m and the thickness was considerable at 78 mm. The ASWJ cutter took approximately 30 hours until the pile could be lifted. However, not full cutting was achieved as the remaining uncut sections broke off shortly before completing the cut. Upon recovery of the monopile it was confirmed that three equally spaced stitches were not fully cut [18]. Estimations of the cutting progress before the rupture occurred lead to a value of between 98% and 98.6%. One of the remaining stitches can be seen in Figure 2.1.

Figure 2.1: Uncut section of the Amrumbank met mast monopile.

Source: [18]

This observation means that after cutting through more than 98% of its circumference, the monopile was still able to support the upper part against breaking off due to the wave loads. When these works were carried out on the 24th January 2016, the significant wave height was 1.5 m [19].

This operation gives a first overview of the cutting operation. For this work it is especially interesting because this case can be used to validate the model to predict the failure of the monopile. However, when decommissioning the monopiles of a WTG, significant differences in the pile dimensions can be expected. In the above example a small but thick monopile was removed, with a diameter of 3.5 m and a thickness of 78 mm. WTG monopiles have larger diameters and smaller diameter/thickness ratios. Another important challenge when scaling up the operation to larger and multiple monopiles is to increase the cutting speed. As stated above, only the cutting and recovery of one pile took around 30 hours to complete. In section 2.4 the state of the art of water cutting for offshore applications is analysed to see what progress has been made from 2016 until today.

2.1.3. Early wind farms

To this date, only six European OWFs have been fully decommissioned. One in the UK and Denmark each, and two in Sweden and the Netherlands. An overview of these farms is given in Table 2.1.

For Yttre Stengrund, the monopiles were cut above the seabed, for Lely they were pulled out completely and for Utgrunden I, they were cut below the seabed [20]. As gravity-based foundations were used for OWF Vindeby, no cuts were required for the removal of the foundations. For the most recent projects, OWF Blyth in 2019 and the nearshore OWF Irene Vorrink in 2022, the monopiles were also cut below the seabed [21, 22]. It should also be noted that the six OWFs mentioned above are small either in terms of turbine size or number of turbines, or both. As mentioned before, the scaling of operations to larger turbines, foundations and wind farms in general has yet to be undertaken.

Table 2.1: Summary table of already decommissioned offshore wind farms.

Wind Farm	Country	Capacity [MW]	Foundation Type	Years of Operation	Decommissioning Year
Yttre Stengrund	Sweden	10 (5 × 2 MW)	Monopiles	15 (2001-2015)	2015
Lely	Netherlands	2 (4 × 0.5 MW)	Monopiles	20 (1994-2014)	2016
Vindeby	Denmark	4.95 (11 × 0.45 MW)	Gravity-based	26 (1991-2017)	2017
Utgrunden I	Sweden	10.5 (7 × 1.5 MW)	Monopiles	18 (2000-2018)	2018
Blyth	UK	4 (2 × 2 MW)	Monopiles	13 (2000-2013)	2019
Irene Vorrink	Netherlands	16.8 (28 × 0.6 MW)	Monopiles	26 (1996-2022)	2022

Source: [15, 16]

2.2. Regulatory aspects

This section divides the legal framework into general guidelines and then presents the country-dependent framework for Germany and the UK. The main focus will be on the regulations regarding full or partial foundation removal.

2.2.1. General guidelines

In 1989, the International Maritime Organization (IMO) published the ”Guidelines and Standards for the Removal of Offshore Installations and Structures on the Continental Shelf and in the Exclusive Economic Zone” [23]. These guidelines and their adoption by the German and British authorities are analysed below.

According to the IMO, decommissioned offshore installations must be removed from the sea as soon as possible. By default, full removal is favoured, but there are some exceptions where partial removal can be allowed. The coastal state responsible for the structure should decide on a case-by-case basis whether partial removal is possible. The following aspects on which this assessment should be based have been identified by the IMO:

- Possible impact on the safety of surface or subsurface navigation.
- Possible impact on the marine environment.
- Material degradation and the resulting future impact on the marine environment.
- Risk of shift of the installation from its original position.
- Costs, technical feasibility and potential harm to personnel.
- Establishment of a new purpose.

The coastal state always has the option of issuing more and stricter removal requirements. If partial removal is decided and parts remains in-situ, further measures include monitoring and possibly marking the site. [23]

2.2.2. Legal situation in Germany

In Germany, the Bundesamt für Seeschifffahrt und Hydrographie (BSH, *eng.: Federal Maritime and Hydrographic Agency*) issues permits for offshore activities such as the decommissioning of offshore structures like wind farms. According to the BSH, before an OWF reaches the end of its life, the owner of the turbine must submit a final decommissioning plan. This should be based on the decommissioning concept that is part of the technical proposal for development prior to the construction of the wind farm. Any technical developments between the original planning proposal and the final decommissioning plan should be taken into account. The BSH then reviews the plan and issues the authorisation to carry out the decommissioning work [24]. Further, the IMO guidelines are applied by the BSH and partial removal of the foundations can be allowed, with the minimum cutting depth being 1 m below the seabed. Before, an assessment and consideration of future sediment redistribution has to be conducted [25].

2.2.3. Legal situation in the UK

In the UK, decommissioning OWFs is regulated in the Energy Act from 2004. The British pendant to the BSH is the Department for Business, Energy & Industrial Strategy (BEIS) which regulates the decommissioning procedures through the before mentioned Energy Act. As a general rule, the ”polluter pays” principle holds. This means that a person or institution who constructs, owns or operates an installation is responsible for its decommissioning at the end of its life, especially with regard to the costs connected. Similar to Germany, a final decommissioning plan based on the initial development proposal must be created and approved by the secretary of state. As the Energy Act adopts the IMO guidelines, full removal of the foundations is favoured by the BEIS and should be the default methodology. Only in cases where full removal would pose unacceptable risks to the personnel or the environment, would not be technically possible or would cause extreme costs, exceptions may be considered. Arguments for partial decommissioning should be made individual for the site, with personnel and environmental safety concerns being the most relevant for the BEIS. [26]

As the BEIS guidance only applies to England and Wales, Scotland has its own guidance. However, this is effectively exactly the same as the BEIS. The only difference is that the issuing authority is the Scottish marine environment directorate, namely Marine Scotland [27].

2.3. Decommissioning sequence

This section discusses the decommissioning sequence of an OWF. Only the turbines, cables, transition pieces, foundations and scour protection are considered. Monopile foundations are assumed as they are the most prominent and used type of foundation (see Figure 1.3). It must be noted that each site is different in terms of bathymetry, soil or environmental conditions. Therefore, each decommissioning plan is individually adapted to the respective site. The following only is an approximate description of the most important parts to be removed and how the decommissioning generally can be done.

2.3.1. Turbines and cables

The decommissioning work begins with the turbines, which should be completely removed from the site. For the turbines, the principle of reverse installation can be applied, which means that the installation process is carried out in reverse order. Just as there are several installation methods, there are also multiple ones for decommissioning. These methods depend, among other things, on the vessel used with its crane lifting capacity and the deck space. However, the most likely solution would be to unbolt the rotor blades from the nacelle individually, lift them on deck, then lift only the nacelle on deck and finally dismantle the tower. The lifting operations can begin after the turbine has been disconnected from the electrical grid and the different parts have been unscrewed. If this is not possible, e.g. due to corrosion, the bolts can be cut with grinders or plasma cutters. In addition, liquids and chemicals (e.g. gearbox oils), which can harm personnel or the environment, must be drained if it is not certain that they will remain inside of the nacelle until it is unloaded onshore. [28, 29]

The subsea cables are directly connected to the turbines. Typically, both inter-array and export cables are buried at a depth of more than one meter below the seabed [30]. Options for cable removal include partial or complete extraction. Due to the considerable length of the cables, their full removal is regarded as very harmful to the environment as the extraction would cause significant damage to the seabed [31]. In addition, complete excavation is costly, so that partial removal is preferred. However, if partial removal is carried out, continuous monitoring and possible intervention are required if cables become exposed [32].

2.3.2. Foundations, transition pieces and scour protection

Once the turbines have been successfully dismantled, the transition pieces can be removed. Depending on the type of connection to the monopile, either bolted or grouted, the decommissioning process is different. In the case of a bolted connection, the transition piece can be unscrewed and lifted from the foundation. In the case of a grouted connection, the transition piece usually has to be cut off the foundation, making the operation more complicated. Another option would be to not remove the transition piece separately and to lift it together with the monopile. This would result in a smaller number of lifts, but with more weight being moved, and therefore needs to be assessed in terms of crane capacity and safety [28].

Regardless of whether the transition piece is still attached at the top or not, the monopile must be removed. As previously discussed, there are some uncertainties about this and the foundation is considered the most challenging part of OWF decommissioning. There are basically two options: Complete removal, e.g. using the vibratory extraction method, or partial removal, where the monopile is cut off below the seabed. As already seen in the regulations section, partial removal is only permitted under certain conditions and requires subsequent survey measures. Nevertheless, this method is considered the base case in almost all decommissioning plans [28]. The reason for this is that from today's perspective the environmental impact of removing the pile completely and the associated costs would be unreasonably high, as the penetration depth of the pile can be 40 m or more [29].

Partial removal can be carried out by internal or external pile cutting below the seabed. Internal cutting can be done by using an ASWJ or gas cutting tool, external cutting can also be done with the same or alternatively with a tool using tungsten or diamond wires [29]. The biggest difference is that for the external cutting good external access to the monopile is needed. However, when a cut is to be made below the seabed, this is easier to achieve on the inside of the pile. So, internal cutting has its advantages in this specific field of work [33].

The process of using an internal water cutting tool is described using Figure 2.2. It is important to note that the cut line in the figure is above the mudline, whereas in the actual application it is below. However, this adjustment does not change the overall process. Furthermore, the transition piece is removed separately from the monopile.

The cutting process is carried out in six steps. First, the transition piece, which was previously separated from the foundation, is lifted with a crane to expose the inside of the monopile. Larger debris and objects are pulled out of the monopile using a grab, followed by the removal of smaller dredged material and sludge using a dredging pump. These measures expose the inside of the monopile up to a few meters below the intended cutting line to allow space for the cutting tool. Optionally, the surface can be cleaned before the cutting phase. The cutting tool is then lowered into the monopile and fixed inside the foundation with hydraulic arms before the cutting process begins. Finally, the cut-off part of the monopile is lifted onto the vessel together with the cutting tool.

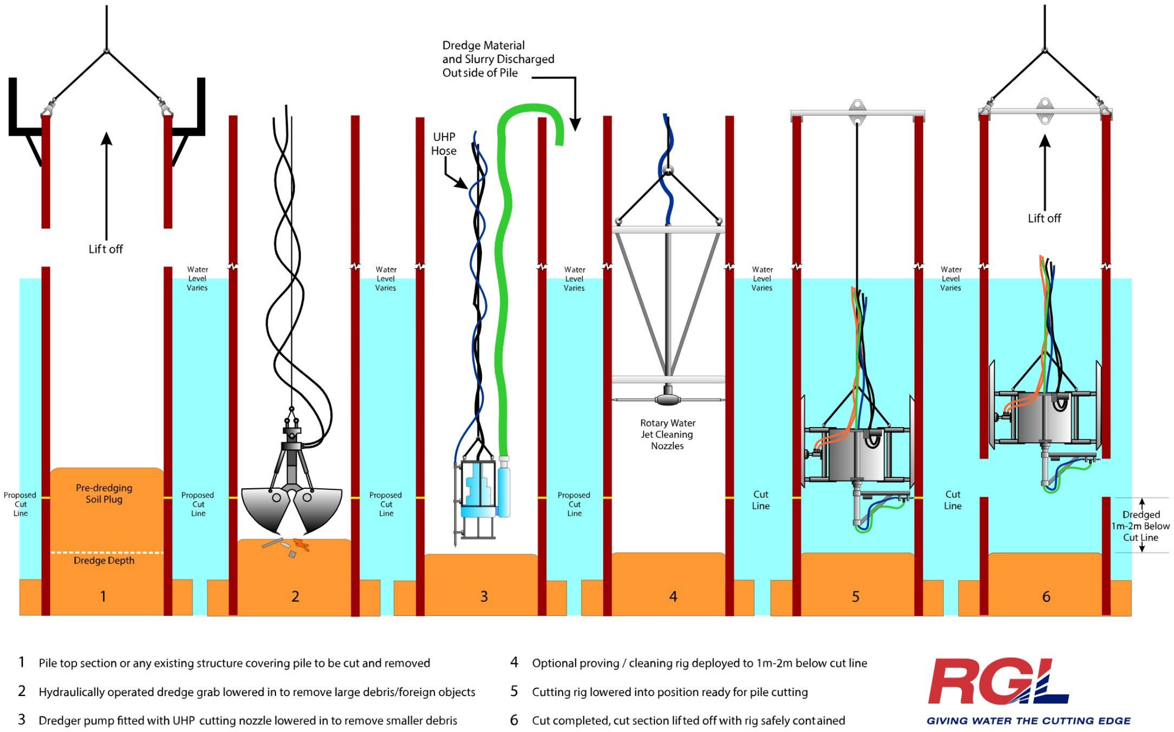

Figure 2.2: Underwater internal pile cutting.

Source: [34]

Due to the long service life of OWFs, it is likely that the scour protection has become a new habitat for marine life. Removing the scour protection would therefore also destroy this new habitat. Hence, it is assumed that it is acceptable to leave it on the seabed, especially if natural materials such as stones have been used as scour protection. Also concrete mats have already been designed to allow fishing above them and could remain in-situ. [29]

2.4. Water cutting technology

The most prominent technique for the subsea cutting of offshore structures is the ASWJ technology. This is because the technology is versatile and can be used for steel, composites and most other materials. Furthermore, large thicknesses of more than 300 mm can theoretically be cut. This and the operational safety and environmental friendliness make the ASWJ technology the preferred choice for monopile cutting. [35]

An ASWJ cutter uses a mixture of high-pressure water and abrasive material to cut through the material. First, the water is pressurised to more than 1000 bar by a pump and afterwards the abrasive is added. This takes place in a mixing chamber upstream of the actual cutting nozzle from which the water jet emerges [36]. A typical cutting head with an integrated mixing chamber is shown in Figure 2.3.

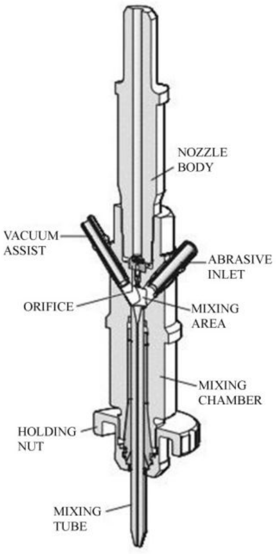

Figure 2.3: Cross-sectional view of an ASWJ cutting head.

Source: [36]

There are several different abrasives, some of which are also environmentally friendly [33]. This makes the technique non-polluting, as only water is used next to the abrasive. In addition, the material is not separated by heating as is the case with other methods. This and the fact that no flammable substances or other chemicals need to be stored on board make the method also safe for the people operating it [35].

Cutting with an ASWJ cutter requires a constant high pressure from the pump and a continuous flow of abrasive. These two factors make the ASWJ cutting process an expensive operation [36]. This effect is intensified by the fact that the cutting speeds for wall thicknesses of 50 mm or more are only 10 mm/min [37]. Cutting systems with multiple cutting nozzles are therefore used to shorten the duration of the operation and thus reduce costs [36]. Figure 2.4 shows an ASWJ cutting system with three cutting heads. The fixing mechanism with fixing pads inside a monopile is also shown.

With three cutting heads as presented, a threefold cutting speed can be achieved in comparison with only one nozzle. In addition to the shorter time that the system is in use, the time required for additional equipment, personnel and the working vessel is also reduced. Time thus is the most important factor in reducing costs [36]. This influence is particularly relevant for operations in which not just one monopile but several are decommissioned, i.e. several cuts are made. For these reasons, an ASWJ cutting system with three cutting heads is used in the further course of this work.

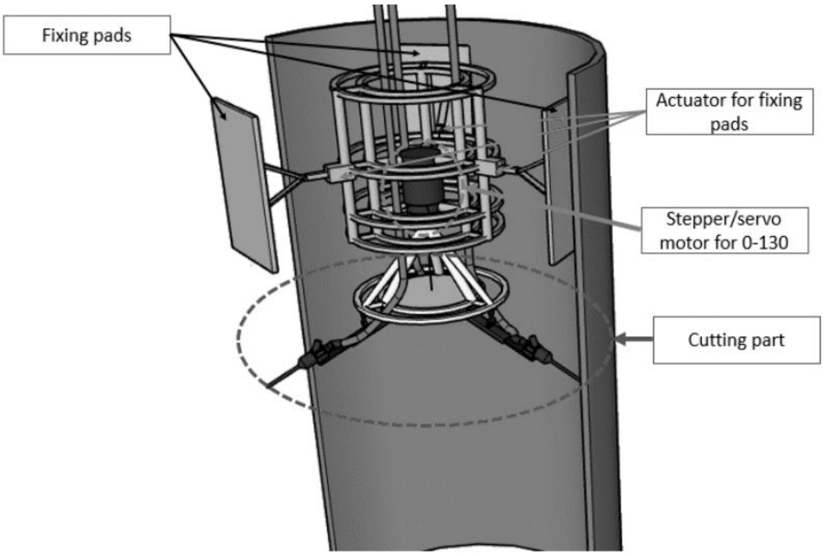

Figure 2.4: ASWJ cutting system with three cutting heads.

Source: [36]

Furthermore, it is important that the tool inside of the monopile does not hinder the lifting operation after successful cutting. Therefore, the tool should have an integrated lifting frame that allows for lifting the monopile with the tool still inserted. Once the pile has been recovered, the tool is then removed from the pile.

2.5. Recycling of components

The decommissioning of OWFs is accompanied by the recycling of the dismantled components. The most interesting materials for recycling are steel, cast iron and copper, all of which are dealt with separately in the following section [38].

Steel is mainly found in the turbines and foundations. According to Topham et al. [39], an average of 83% of the turbines (tower, nacelle, generator, gearbox, etc.) installed by 2019 is made of steel. Monopile foundations are made almost entirely of steel. By 2019, around 2 Mt of steel had been used for monopiles. This makes steel by far the largest material component in an OWF with a share of 88% (considering monopiles as foundation type).

Cast iron and copper contribute to significantly lower material quantities in the OWT. Cast iron is used in the wind turbine to support the rotor blades as a rotor hub. The turbines consist of estimated 11% cast iron, making it the second largest recyclable part of the turbine. Copper is by far the most valuable material of the three mentioned. It is found in the turbine and the subsea cables. Since the feasibility of decommissioning cables is at least questionable so far (see subsection 2.3.1), the copper from the cables was not taken into consideration in the above-mentioned study by Topham et al. However, the turbine was taken into account with a small amount of around 1% copper. [39, 40]

Considering the found quantities of steel, cast iron and copper, the values for the recycling of OWTs and monopiles were estimated and standardised per output. The materials of OWTs are valued at £ 17,690/MW and the steel in the monopiles is valued at £ 8,010/MW. With growing turbine and foundation sizes recycling becomes even more important. If large a turbine is compared with two smaller turbines that together have the same capacity of the larger turbine, the material requirement for the single larger turbine is greater. As the previously found values are from 2019, it is likely that this effect can already be observed today and the recycling potential could be greater. [39]

One major component that is difficult to recycle are the wind turbine blades which is due to the composite materials they consist of [41]. They are mainly made of glass fibre reinforced polymer (GRFP), which consists of approx. 60-70% of fibres and the rest of a polymer matrix. To a lesser extent, carbon fibre reinforced polymer composites (CRFP) are also used [42]. The advantages of these materials are their low weight, high strength and resistance to fatigue and corrosion [41]. The problem with recycling is that the polymers are irreversibly cross-linked during production and can no longer be separated from each other [42]. To avoid landfilling shredded blade material, Siemens Gamesa has invented the 'RecyclableBlade'. With the help of a special resin that can be dissolved from the fibres and other materials using an acidic solution, the materials can be separated again and recycled [43]. This is being used and commercially tested at RWE's OWF Kaskasi.

3

Modelling of the monopile removal operation

This chapter explains the approach to modelling the cutting with subsequent extraction of the monopiles and the resulting time schedule. The strategy consists of calculating the maximum hydrodynamic loads and applying them to the monopile. This is done to investigate the effects of different loads on the foundation that is cut below the seabed. In this context, the stresses in the cutting line are of interest, as they determine when the pile will fail after a certain cutting progress. This is relevant for the safety of the operation as a pile that suddenly looses stability poses considerable risks to operators, equipment and environment. After successful cutting, the extraction forces that occur due to the monopile still being slightly embedded in the soil are relevant for the loads on the crane. The crane loads largely determine which vessels can be used for the monopile decommissioning. From the findings during the technical analysis of cutting and extraction of the piles conclusions about the time schedule can be drawn.

Regarding the specific content of this chapter, first the calculation of the hydrodynamic forces is explained in section 3.1. Afterwards, the decommissioning is divided into the cutting (see section 3.2) and subsequent extraction (see section 3.3) of the monopile. These sections cover the used soil models and the calculation of forces and stresses in the cut and during extraction. The results are then compared and validated by using the Amrumbank met mast decommissioning project (see subsection 2.1.2) where the cutting was carried out successfully. Furthermore, the dynamic behaviour is also tested with a modal analysis of the monopile during different cutting progresses. A parameter study is used to analyse the influence of various variables on the developed models. This allows the most relevant parameters for the operation to be determined. All assumptions and simplifications made during modelling will be described as soon as they occur in the model. In section 3.4, the issues of the pile losing its stability and limiting criteria for the operation are further discussed. The modelling of schedules for offshore operations such as the one considered here depending on certain weather limits is explained in section 3.5. The chapter closes with an overview of all simulations that will be carried out using the developed models (see section 3.6). In the last section also all the used parameters for the case studies simulations are given.

3.1. Hydrodynamics

This section deals with the hydrodynamic models used in this work to calculate the wave dynamics and the resulting maximum forces on the monopiles. The section generally follows DNVs Recommended Practices (RP) on environmental conditions and loads [44]. Firstly, the wave dynamics are explained and then the calculation of the forces caused by these waves is described.

3.1.1. Wave dynamics

According to DNV, realistic ocean waves are best described using irregular wave models. An irregular wave is obtained by summing many regular waves of different random amplitudes, frequencies and directions. There are various wave models that can be used to generate irregular waves. The use and validity of these models depends on certain wave parameters. The validity of some wave theories can be seen in Figure 3.1 using dimensionless key figures.

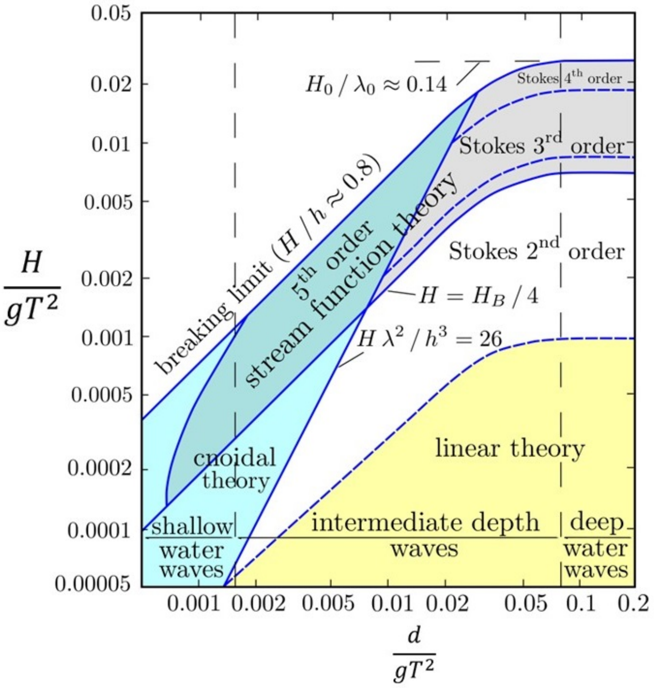

Figure 3.1: Validity of several theories for periodic water waves.

Source: [45]

Here, H stands for the wave height, d for the water depth, g for the gravitational constant and T for the wave period. Only two of the above wave theories are used in this work, namely the linear (airy) and the second-order Stokes wave. These models cover a wide range of sea conditions, especially in medium to deep water. The linear wave is the simplest theory and the second-order Stokes wave is an extension to it. A first-order Stokes wave corresponds to the linear wave theory. The difference is that linear waves have a pure sinusoidal shape, whereas Stokes waves are asymmetrical and have steeper crests and wider troughs [44]. In Figure 3.2, the different shape of the surface elevation η can be seen.

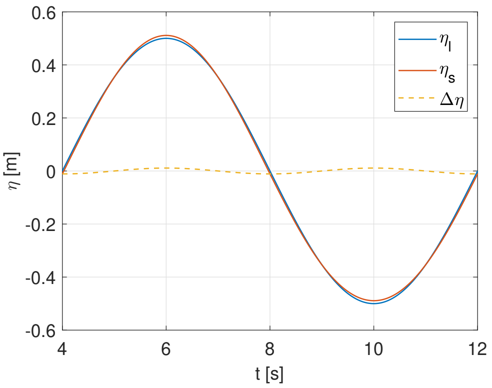

Figure 3.2: Differences between linear and second-order Stokes wave.

This wave has a height of 1 m, a period of 8 s and propagates in a water depth of 25 m. The surface elevation with the linear model is shown in blue and the surface elevation with the second-order Stokes model is shown in orange. The yellow line presents the difference. In terms of validity, the wave lies almost exactly on the boundary between the linear theory and the second-order Stokes wave. It can further be observed that for the wave above, the difference in η is only a few centimeters. However, later the theory-defining parameters H, d and T will not be constant which changes the theory to be used. Therefore, the difference between the waves for both models can increase. Thus, before determining the wave dynamics in the calculation model it is checked whether to apply the linear or Stokes model. The additional effort for the calculation by querying which theory must be used is minimal.

It has already been explained that irregular waves result from the summation of several regular waves. One way to obtain different waves all characterised by the same sea state is to use wave spectra. Sea states can be described by a combination of their significant wave height H_s and the peak period T_p. H_s describes the average of the highest third of the waves and T_p is the associated period. The resulting wave spectrum represents the power spectral density of the free surface elevation S_η. This means that it shows how the energy in the waves of the respective sea state is distributed depending on the frequency [44]. One widely used wave spectrum in the industry is the JONSWAP spectrum [46]. The JONSWAP spectrum for the waves with $H_s = 1$ m and $T_p = 8$ s is depicted in Figure 3.3.

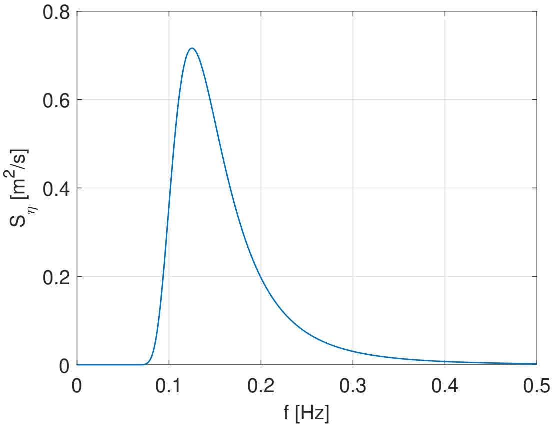

Figure 3.3: JONSWAP spectrum.

It can be seen that the energy is distributed over waves of different frequencies, but peaks at the peak frequency f_p, corresponding to T_p. The data from the spectrum can be used to calculate the amplitude ($\frac{H}{2}$) for waves of different frequencies. These waves of different amplitudes and frequencies are each additionally assigned a random direction ϵ between 0° and 360° and then added together. For an irregular wave created from the summation of linear waves, Equation 3.1 shows how the free surface elevation η_l is calculated.

$$\eta_l = \sum_{i=1}^{n} \frac{H_i}{2} \cos\left(\omega_i t + \epsilon_i\right) \tag{3.1}$$

Here, ω is the angular frequency calculated from the regular frequency f and t is the dimension of time. For a second-order Stokes wave, the equivalent to Equation 3.1 can be found in section A.1 in the appendix. The equations for the wave velocity and acceleration which are important for the force calculation in the next section can also be found in section A.1.

3.1.2. Hydrodynamic forces

The previously calculated wave dynamics are used for the computation of the hydrodynamic forces on the monopile. For this, especially the wave velocity u_w and acceleration $\dot{u}_w$ are of importance (see section A.1). For slender cylindrical structures, the Morison equation can be used to determine the acting forces. This assumption of slender cylindrical structures applies to many monopiles. However, there is a limiting criteria for the validity of the Morison equation. According to DNV, the wave length λ should be at least five times the diameter D of the monopile. This way the velocity gradients and the accelerations of the fluid particles perpendicular to the structure are negligible. When using the Morison equation, the result is the normal force f_N on a cross sectional element of the monopile (see Equation 3.2). The equation can be integrated along the vertical coordinate to find the total hydrodynamic force on the structure.

$$f_N(t) = \rho_{sw} C_M \frac{\pi D^2}{4} \dot{u}_w + \frac{1}{2} \rho C_D u|u| \tag{3.2}$$

Here, ρ_{sw} is the density of sea water, C_D is the drag coefficient, C_M is the inertia coefficient and u is the sum of the wave velocity u_w and a potential current velocity u_c. The first part of the equation is the inertia term and proportional to the acceleration of the fluid. The second part is the drag term and proportional to the square of the fluid's velocity. The drag coefficient depends on the relative surface roughness Δ of the structure.

$$C_D = \begin{cases} 0.65 & \text{for } \Delta < 10^{-4} \\ \frac{29+4\log(\Delta)}{20} & \text{for } 10^{-4} < \Delta < 10^{-2} \\ 1.05 & \text{for } \Delta > 10^{-2} \end{cases} \tag{3.3}$$

Since the considered monopiles in this work are decommissioned after 20+ years of ocean exposure, significant marine growth is expected. This largely increases the surface roughness compared to steel or even concrete [44]. Thus, the largest drag coefficient $C_D = 1.05$ is assumed for the calculations.

The inertia coefficient depends on the Keulegan-Carpenter number K_C which is calculated according to Equation 3.4.

$$K_C = \frac{u_{max} T}{D} \tag{3.4}$$

Here, u_{max} is the maximum fluid velocity, resulting from waves and current. For K_C numbers smaller than 3, C_M can be taken as 2. For larger K_C numbers, the inertia coefficient is estimated as follows.

$$C_M = \max \left\{ \begin{array}{c} 2 - 0.044(K_C - 3) \\ 1.6 - (C_D - 0.65) \end{array} \right\} \tag{3.5}$$

For short waves, when the limiting condition that the wavelength is at least five times the diameter of the monopile no longer applies, the Morison equation overestimates the loads on the structure. To remedy this, the MacCamy-Fuchs correction can be used in these cases. With this correction from 1954, the forces acting on a monopile can be calculated independently of the $\frac{\lambda}{D}$ limit [47]. Equation 3.6 shows the associated formula for determining the normal force on a cylindrical section.

$$f_N(t) = \frac{2\rho_{sw} g H}{k} \frac{\cosh(k(z+d))}{\cosh(kd)} A\left(\frac{D}{\lambda}\right) \cos\left(\omega t - \alpha\left(\frac{D}{\lambda}\right)\right) \tag{3.6}$$

Here, k is the wave number, z is the depth coordinate, and A and α are functions of the $\frac{\lambda}{D}$ ratio. The corresponding graphs for these functions can be found in section A.2 in the appendix. According to Malik, an equivalent inertia coefficient C_M^{eq} can be found by comparing Equation 3.2 and Equation 3.6. The found coefficient can be used in the regular Morison equation to account for the MacCamy-Fuchs correction in short waves [48].

$$C_M^{eq} = \frac{4A\left(\frac{D}{\lambda}\right)}{\pi^3} \left(\frac{\lambda}{D}\right)^2 \cos\left(\alpha\left(\frac{D}{\lambda}\right)\right) \tag{3.7}$$

Figure 3.4 presents a comparison of the constant inertia coefficient C_M and the equivalent coefficient C_M^{eq} found using the MacCamy-Fuchs correction. In short waves with $\frac{\lambda}{D}$ < 5 a significant difference can be observed.

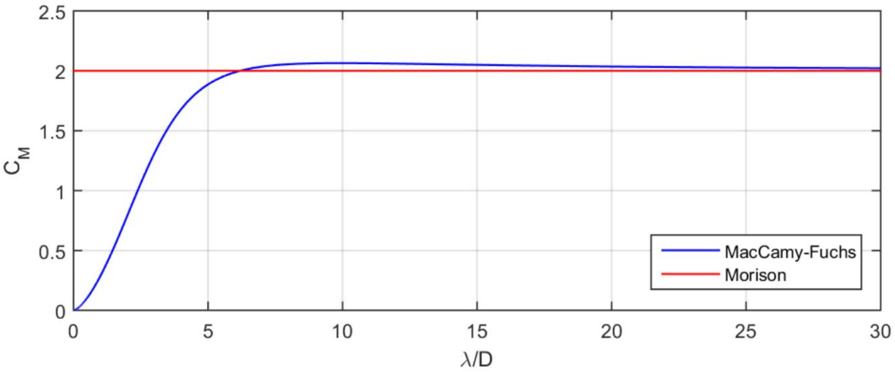

Figure 3.4: Inertia coefficients from Morison equation and MacCamy-Fuchs correction.

Source: [48]

3.2. Monopile cutting

This section gives an overview of the modelling of the monopile cutting. The modelling approaches are explained and it is shown how the stability of the monopile during cutting is calculated and evaluated. Furthermore, the modal analysis of the monopile is described.

3.2.1. Modelling approach for cutting

As already seen in section 2.4, it is of key importance to ensure a fast cutting process when decommissioning several monopiles. Therefore, three simultaneously operating cutting nozzles distributed in a circle with a spacing of 120° are assumed in this thesis. On the one hand, this ensures that the cutting speed is tripled and, on the other hand, that there are always three uncut sections left to support the part of the monopile to be cut off. The monopile receives additional support from the crane, which is connected to the pile for the entire cutting time. To avoid placing additional load on the cut-line and pulling on the monopile, only 80% of the weight of the monopile may be taken into the hook. Due to this it is assumed that the pressure resulting from the pile's self weight in the uncut sections is negligible compared to the stresses due to wave and current loading. In this configuration, the stresses in the cutting line are now calculated and analysed to see how they change as the cutting process progresses. This allows conclusions to be drawn about the stability of the pile during the cutting process. The stress calculations are carried out from a cutting process of 90% on. To better illustrate the cutting process, Figure 3.5 shows the progress with three cutting nozzles after 50%, 70% and 90% successful cutting.

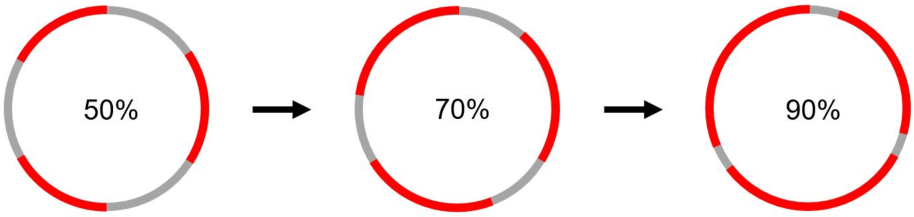

Figure 3.5: Cutting progress at different stages of the cut.

The stresses that are calculated in the cut line result from the maximum hydrodynamic forces that act on the monopile. To calculate these maximum loads, a time series has to be determined from which the maximum force is taken. Since the stress calculations are only carried out for the last 10% of the cutting process because failure is not assumed before, the time series is taken as the length it takes to cut through 10% of the pile's circumference. To find the maximum value with a larger safety, the time series is computed 10 times and the maximum across all series is taken. The effects of this approach will be analysed later.

In order to calculate these stresses, a simplified foundation model is used: the effective fixity model. This model states that the monopile is considered to be clamped at a certain depth of embedment below the seabed. For monopiles, the fixity depth should be around 3.5 times the outer diameter of the pile. With this model, the complicated soil-structure interactions can be significantly simplified. However, forces and stresses in the foundation can still be calculated accurately as long as they are below the seabed and above half the depth of the effective fixity. This is the case for the cut line and the model can be applied. Since the monopile is now considered to be fixed, the force and moment curves look as shown in Figure 3.6. It should be noted that it is assumed that a transition piece had to be cut off so that the pile head is below mean sea level (MSL).

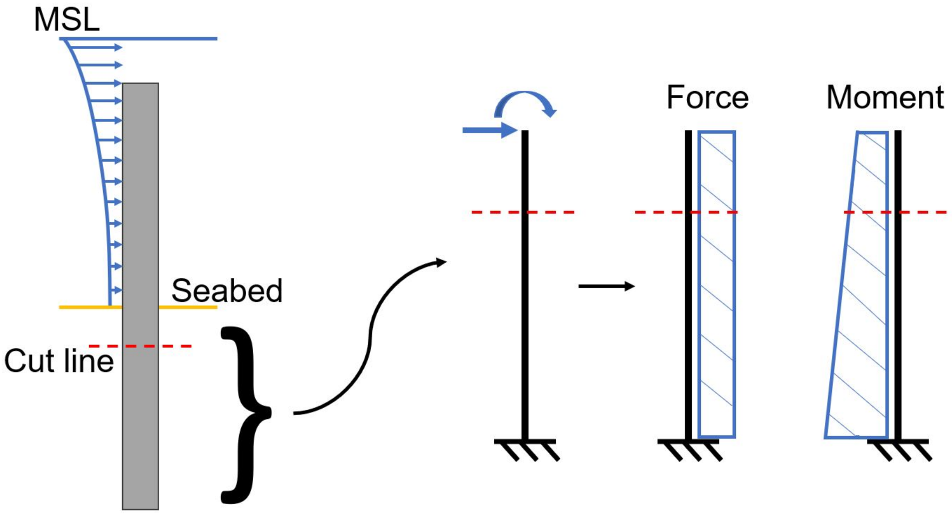

Figure 3.6: Model simplification with force and moment line.

The loads in the cut line are calculated on the basis of the horizontal force and the overturning moment. The considered stresses are the maximum normal stress and the shear stress. The maximum normal stress occurs due to the bending moment if only one uncut section is loaded in tension and the other two in compression. The shear stress occurs due to the horizontal force, which is taken by the area of the three remaining uncut sections. Figure 3.7 shows these two types of stress. The direction of the hydrodynamic load, which is assumed to generate the maximum tensile stress, can also be seen.

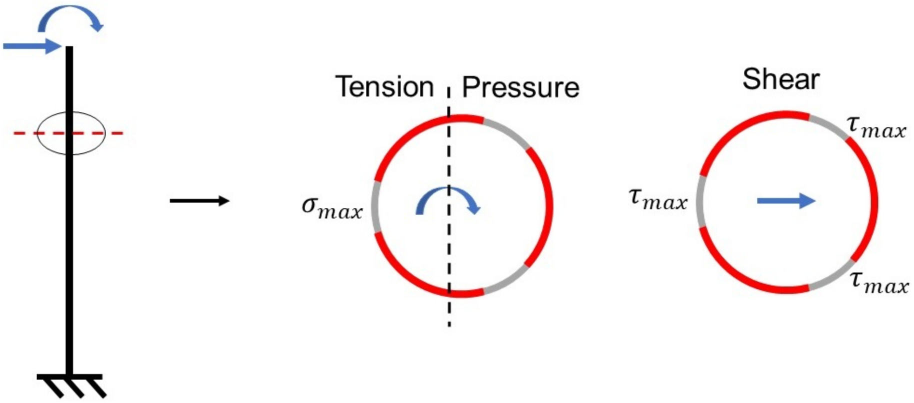

Figure 3.7: Maximum tensile and shear stresses in the model.

It can be seen that the line through which the moment is equally split into a tensile and a compressive force is not in the centre of the monopile, but is shifted slightly to the left. In order to determine the share X of the pile diameter D that splits the moment, the distance between the centre line and the middle part of the two uncut compressive sections is calculated. Figure 3.8 gives an overview of how this distance is calculated. The dash-dot line represents the centre line and the dashed line is the line over which the moment is split. It should be noted, that the sketch is not true to scale and that the sizes of the uncut sections are exaggerated.

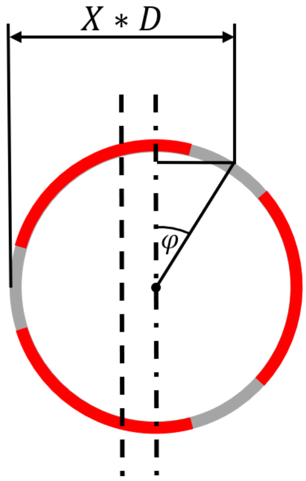

Figure 3.8: Calculation of the share of the diameter that splits the moment.

Since the worst case loading direction is always assumed, the centre of the two compressed uncut sections always remains at the same distance from the centre line, regardless of the cutting progress. This can be described by the angle φ, which is 30°. If the centre points of the uncut sections are taken, possible stress variations across the cross-sections are neglected. However, since only the last 90% of the cutting are of interest, these sections are small compared to the diameter. This assumption improves further as the cut progresses and the minimum and maximum values of X can be seen in Table 3.1. The value of X when taking the centre points of the uncut sections is 0.75. This assumption is also discussed in section 4.3.

Table 3.1: Minimum and maximum values of X with increasing cutting progress.

Progress [%]	X_{min}	X_{max}
90	0.7	0.794
92	0.711	0.785
94	0.721	0.777
96	0.731	0.768
98	0.741	0.759

The calculated stresses are analysed as part of the strength analysis to assess the stability of the monopile during cutting. Two values from the stress-strain diagram are used for the permissible tensile stress: the yield strength and the ultimate tensile strength. The yield strength describes the stress value above which plastic deformation occurs. The ultimate tensile strength describes the maximum stress that a material can withstand before failure. An example stress-strain diagram for steel can be found in section A.3 in the appendix. In order to evaluate the calculated shear stress equally, the ultimate shear strength of the material must be taken into account. For steel, this is usually given as 80% of the ultimate tensile strength.

3.2.2. Stress calculation

The stress calculation with analytical formulae will now be shown. Firstly, the tensile stress calculation is described, followed by the determination of the shear stress. The horizontal base shear force F_B and the overturning moment M_O at the seabed calculated using the hydrodynamic model are converted into an axial force P_a in the tensile loaded section and two axial forces half as large in the compression-loaded section (see Figure 3.7). Here, only the tension-side is of interest. To find the distance that splits the moment into the axial forces, according to Figure 3.8, Equation 3.8 can be used.

$$X = \frac{\frac{D}{2} + \sin(\varphi)\frac{D}{2}}{D} = \frac{1}{2}(1 + \sin(\varphi)) \tag{3.8}$$

For a previously determined constant angle φ of 30°, the value of X is 0.75. The calculation of the force P_a in the tensile loaded section due to the base shear force F_B and the overturning moment M_O then becomes:

$$P_a = \frac{F_B d_c + M_O}{0.75D} \tag{3.9}$$

Where d_c is the cutting depth below seabed. The maximum tensile stress σ_{max} is now determined by relating the axial force to the area of this third of the cut line.

$$\sigma_{max} = \frac{3P_a}{A_c} \tag{3.10}$$

Where A_c is the total area of the remaining steel in the cut line. The maximum shear stress is calculated by distributing the base shear over the three uncut sections remaining in the cut-line.

$$\tau_{max} = \frac{F_B}{A_c} \tag{3.11}$$

The effects of this simplified calculation method are further discussed in section 4.3.

3.2.3. Modal analysis

A modal analysis is carried out to determine the change of the monopile stiffness with an increasing cutting progress. The principle of a modal analysis is to solve the eigenvalue problem of a structure. This can be exemplary seen in Equation 3.12.

$$[\boldsymbol{K} - \boldsymbol{\omega}^2 \boldsymbol{M}]\boldsymbol{\phi} = \boldsymbol{0} \tag{3.12}$$

Here, $\boldsymbol{K}$ is the stiffness matrix and $\boldsymbol{M}$ is the mass matrix of the structure. The solution consists of the eigenfrequencies $\boldsymbol{\omega}$ and the eigenvectors $\boldsymbol{\phi}$, which describe the dynamic behavior of the considered system. Each eigenfrequency ω_i has one associated mode shape $\boldsymbol{\phi_i}$. The eigenfrequencies are the frequencies at which the structure oscillates with the respective mode shape. The true shape of the vibration is a superposition of all mode shapes. However, due to the stiffness of the structure, the mode shapes that are assigned to the lowest natural frequencies are usually decisive for the true mode shape. [49]

For the monopile at hand with the cut progressing through it, the Equation 3.12 cannot be solved analytically in an easy manner. Therefore, a finite-element-method (FEM) software is used to conduct the modal analysis. Here, Autodesk Inventor is used. The software allows for the creation of a CAD model of the monopile with subsequent modal analysis. To carry out the analysis using the FEM, the CAD model is divided into a finite number of small sub-elements, in this case tetrahedra. The physical behaviour of each individual tetrahedron can be calculated using a shape function of a certain order. In this case quadratic shape functions are used. Continuity conditions determine how this behaviour is propagated from one element to the next. In this way, the behaviour of each element and thus of the entire structure can be determined step by step. Figure 3.9 depicts the FEM model with its generated mesh, a close up of the mesh around the cut and the used quadratic tetrahedral element with 10 nodes.

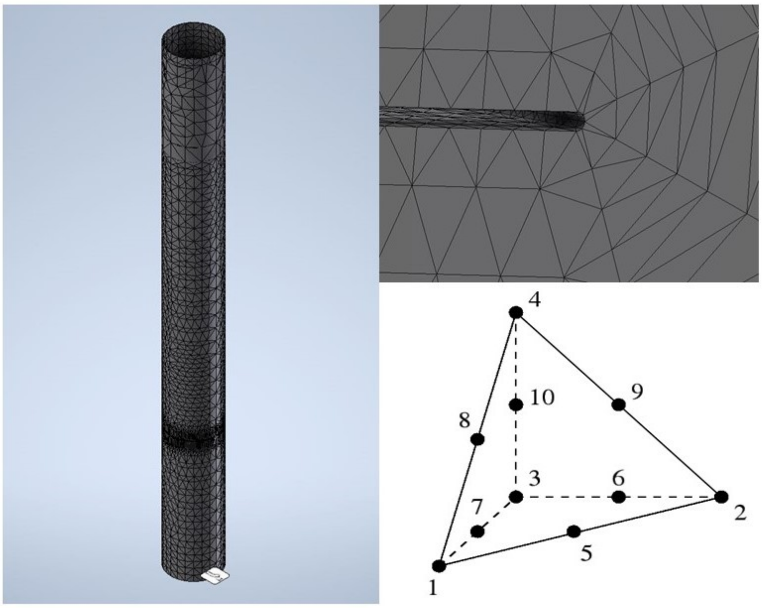

Figure 3.9: FEM model and quadratic tetrahedral element.

Source: [50]

It can be seen that the the mesh is refined around the cut because there the main point of interest is expected. Furthermore, the edge of the cut line is modelled with a radius. This is done to mitigate the risk of an occurring singularity. These can appear at sharp edges, as the cutting edge without the introduced radius would be. This poses problems regarding the convergence of the FEM solution. In the singularity points the calculated deformations increase towards infinity if the mesh is further refined. Normally, with increasing mesh fineness, the FEM solution should converge towards a value. The influence of the mesh density on the results of the modal analysis is therefore analysed in a mesh convergence study.

The modal analysis is carried out for different stages of the cutting to be able to show the variation of the dynamic properties with increasing cut progress. The results of the modal analysis and the underlying assumptions are discussed in section 4.3.

3.3. Monopile extraction

This section gives an overview of the calculation of the forces required for the monopile extraction and the resulting crane hook loads. The approach to modelling the interaction of different loads on the crane is described, together with an explanation of the modelling choices. Then, the calculations for determining the remaining monopile weight and the axial soil bearing capacity are explained.

3.3.1. Modelling approach for extraction

The force required to pull the monopile out of the seabed is made up of different parts. These include the weight of the monopile and the remaining friction between the soil and the pile (see Figure 3.10). The weight also includes secondary elements such as sacrificial anodes or marine growth that has accumulated over the years. For a conservative estimate, it is assumed that the soil on the outside of the monopile is not disturbed by the previous cutting and still applies frictional resistance. This way the maximum possible extraction forces can be determined. The values are converted into masses with the unit tonne, as this is the usual specification for the capacity of cranes.

The required crane capacities are of particular importance when a vessel is selected for the decommissioning operation. However, additional analyses would have to be carried out for a holistic investigation of the heavy lifting operation. These include the forces and dynamics of lifting the monopile at any time during the operation, especially when lifting through the air and setting it down on board. The determination of possible slack loads that may occur during extraction must also be analysed. However, these calculations are not part of this work. The same applies to the design of the lifting equipment and possible attachment points on the monopile. Here, an estimate of the required maximum crane capacity is deemed sufficient to determine a possible vessel that can be used to carry out the decommissioning. Furthermore, using this approach, the influence of different structural and environmental parameters on the required crane capacity can be investigated. Further information on these variations can be found in section 3.6.

3.3.2. Monopile weight

The weight of the monopile can be calculated using simple formulae, which will not be explicitly stated here. The pile itself consists exclusively of steel, which means that the weight calculation can be carried out using volume and density. The water displaced by the steel must be subtracted from the weight of the monopile. In addition to the buoyant weight of the monopile, there is also the weight of the tool, which is negligible compared to the monopile, and the weight of the marine growth that has accumulated over time. This is deposited on the outside of the monopile and can also be calculated using the volume and density. Numerical information on all densities, weights and the thickness of the marine growth can be found in section 3.6, where values for all parameters are given.

3.3.3. Axial soil resistance

In Figure 3.10, the two general failure modes for a pile under axial loading can be observed. On the left unplugged failure and on the right plugged failure is depicted. However, since the monopile is dredged internally before the cutting process is started, no soil is inside the pile. Therefore, it is impossible that plugging occurs and only the unplugged failure mode is considered.

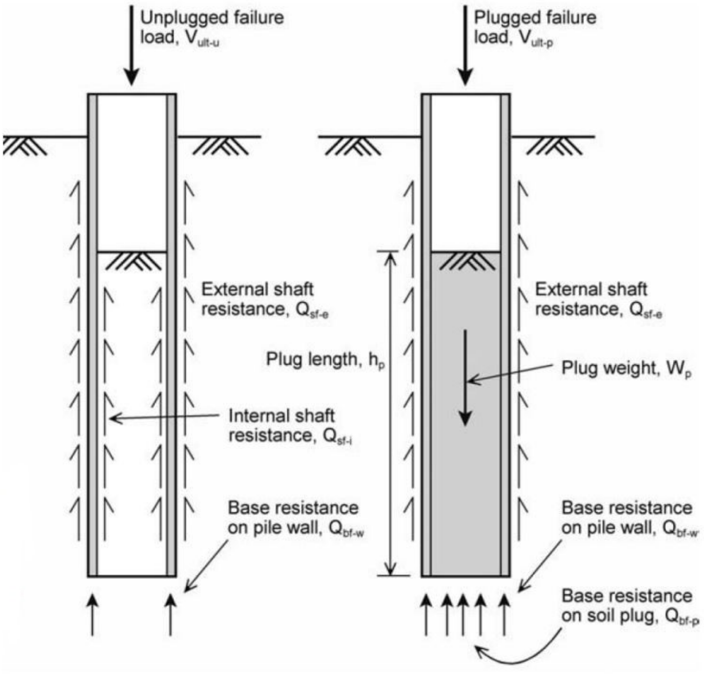

Figure 3.10: Unplugged and plugged behaviour of axially loaded piles.

Source: [51]

The unplugged failure mode can be further simplified as the remaining axial soil resistance can be reduced to only the external shaft friction $Q_{sf,e}$. Due to the dredged monopile, the internal shaft friction and the base resistance can also be neglected. Now, two different soil types are considered for the calculation of the axial capacity: clay and sand. The following equations are based on guidelines provided by the American Petroleum Institute (API) [52]. In general, the external shaft resistance can be calculated according to Equation 3.13.

$$Q_{sf,e} = \pi D \int_0^L \tau_{sf} \, dz \tag{3.13}$$

Where, L is the embedded length of the monopile, z is the depth coordinate and $\tau_{s,f}$ is the skin friction along the pile which depends on the type of soil. Equation 3.14 presents the terms for $\tau_{s,f}$ under different soil conditions, for soft clay, stiff clay and sand.

$$\tau_{sf,e} = \begin{cases} \frac{1}{2}\sqrt{s_u \gamma_c' z} & \text{for soft clay} \\ \frac{1}{2} s_u^{0.75} (\gamma_c' z)^{0.25} & \text{for stiff clay} \\ \beta \gamma_s' z & \text{for sand} \end{cases} \tag{3.14}$$

Where s_u is the undrained shear strength of the material, γ' is the buoyant unit weight of the soil and β is the shaft friction factor. In section A.4 in the appendix, tables with data for typical values for the soil parameters s_u, γ' and β are provided.

3.4. Limiting criteria

This section is about defining a methodology for finding appropriate limits for carrying out the monopile cutting and subsequent extraction operations. DNV provides a flow chart to determine whether an operation is weather limited and if so how to find the start and interrupt criterion OP_{WF}. [53]

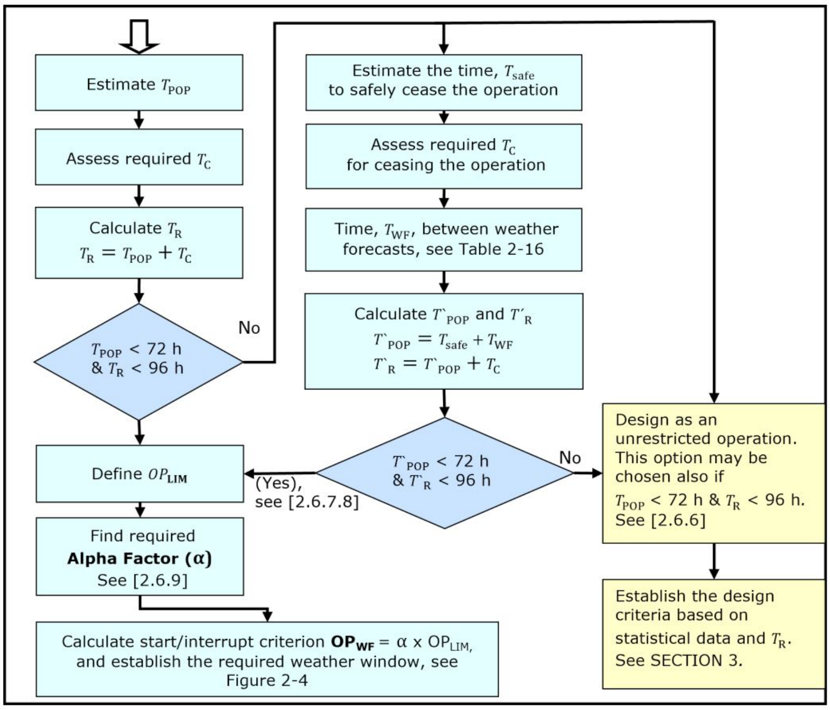

Figure 3.11: Flow chart to find the start/interrupt criterion of a marine operation.

Source: [53]

The first input value is the planned operation period T_{POP}. This is the net time needed to carry out a certain task. To account for general uncertainty in T_{POP}, unproductive time during the operation and possible contingency situations another period is introduced, the estimated contingency time T_C. In most cases it is acceptable to set T_C as half of T_{POP}. This results in the operation reference period T_R which is the sum of the net time T_{POP} and the contingency time T_C. For the tasks during the decommissioning of monopiles the provided thresholds of T_{POP} < 72 h and T_R < 96 h are not exceeded. Because of that, the exceedance case which results in designing a weather unrestricted operation is not considered. Therefore, the next step would be to define the operational limits OP_{LIM} for the task. According to DNV, these limits depend on the weather conditions and other environmental influences. The following criteria must be considered.

- The maximum design environmental conditions.
- Weather restrictions for the safe working of personnel and handling of objects/equipment.
- Weather restrictions for equipment such as ROVs or cranes.
- Weather restrictions for diving (if necessary).
- Weather restrictions for the vessel(s) and especially position keeping systems.
- Weather restrictions for the execution of emergency plans.

The global limit should then be the lowest of these limits. The methodology for finding these limits for the cutting and extraction of the monopiles is explained in subsection 3.4.1 and subsection 3.4.2. Since only the cutting and extraction are regarded as new tasks only their limits are calculated. For the other, more routine tasks of the decommissioning, experience values from already carried out marine operations are taken.

Regarding Figure 3.11, the found operational limits OP_{LIM} are not the final values that determine when to start or stop an operation due to weather restrictions. When on-site, weather forecasts have to be used to predict the weather windows for carrying out the work. To account for the uncertainty in the weather forecasts, an alpha factor (α) has to be applied. The alpha factor is multiplied to the calculated operational limit OP_{LIM} and reduces this to the start/interrupt criterion OP_{WF}. This is the final value to check against the weather forecast, when on-site. In Table 3.2, the alpha factors for the wave limits of the model are given.

Table 3.2: Alpha factors for wave limits.

Alpha factors	H_s = 1 m	H_s = 2 m	H_s = 4 m	$H_s \geq$ 6 m
$T_{POP} \leq$ 12 h	0.68	0.8	0.83	0.84
$T_{POP} \leq$ 24 h	0.66	0.77	0.80	0.82
$T_{POP} \leq$ 36 h	0.65	0.75	0.77	0.80
$T_{POP} \leq$ 48 h	0.63	0.71	0.75	0.78
$T_{POP} \leq$ 72 h	0.58	0.66	0.71	0.76

Source: [53]

The alpha factors decrease with increasing duration of the operation. Thus, with longer operations, the start/interrupt criterion OP_{WF} decreases. To find the factors in between the values for the given wave limits, linear interpolation should be applied. The alpha factors for the wind limits of the operation are given in Table 3.3.

Table 3.3: Alpha factors for wind limits.

Alpha factors	$V_w <$ 0.5 $\times V_{w,10yr}$	$V_w >$ 0.5 $\times V_{w,10yr}$
$T_{POP} \leq$ 1 h	0.90	0.95
$T_{POP} \leq$ 24 h	0.80	0.85
$T_{POP} \leq$ 48 h	0.75	0.80
$T_{POP} \leq$ 72 h	0.70	0.75

Source: [53]

V_w is the design wind limit for the operation, similar to the design wave limit for which a value of H_s is calculated. $V_{w,10yr}$ is the 10 year wind speed.

3.4.1. Cutting

During the decommissioning operation considered in this thesis, the monopile is partially destroyed by the cutting process before being recycled on land. In the recycling process, the original pile is then completely destroyed. This means that the monopile can be handled much more roughly during the removal operation than during installation.

This work is based on the assumption that the monopile cannot be cut completely and from a certain cutting progress and under specific external conditions will break off beforehand. At a certain point, the remaining uncut sections are no longer able to connect the part to be cut with the part that remains below the seabed. Even if the pile itself can be destroyed, it is not desirable for this rupture of the upper part of the monopile to happen too early and unplanned. There are several reasons for this: Firstly, it is important for the operation and especially for the crane operator to have a controlled process. When the monopile comes lose, be it by fully cutting or by premature rupture, the soil around the pile cannot keep the pile in position and it starts moving. This state is undesirable, as this poses horizontal loads on the crane. To minimise the time of this, the crane operator should increase the hook load as soon as possible after the pile is severed to recover it on board. It is therefore of interest to know at what cutting progress and under which environmental conditions a rupture can be expected in order to be prepared for the change in the system. Secondly, the rupture should be straight and follow the cutting line. This ensures that the minimum cutting depth below the seabed required by the authorities is maintained. If a rupture occurs relatively early in the cutting process, it is possible that the cut-line will not be horizontal, causing parts of the monopile to protrude higher than the desired cutting depth. This could easily be mitigated by setting the cut deeper than the required minimum cutting depth. However, this would in turn lead to an increase in extraction forces. The more important reason for a straight rupture that follows the cutting line is the safety of the cutting tool. After the separation of both parts of the monopile, the cutting nozzles are located directly next to the broken sections. If these are not horizontal and the upper part of the pile starts moving, the nozzles can be pressed against the the steel and damaged as a result. When removing a single pile, this could still be considered acceptable as there is sufficient time to repair the tool afterwards. However, when decommissioning the piles of an entire wind farm, the tool should be damaged as little as possible in order to minimise the additional costs of repairs and lost time.

For these reasons, it is necessary to have a controlled operation and produce a straight and horizontal cut for as long as possible. However, due to limited experience and no guidance on this topic, the definition of a cutting progress that must be reached before potential rupture is difficult. To still give a limit, the Amrumbank met mast decommissioning is considered again (see subsection 2.1.2). During the cutting of the monopile of this project, the three remaining uncut sections broke off at a cutting progress of between 98% and 98.6% (Figure 2.1). The operation was successful because the monopile was recovered. Furthermore, the cutting line was almost horizontal and the tool remained undamaged. Therefore, a minimum cutting progress of 98% is assumed as a limit value before the occurrence of a rupture is allowed. It will be calculated what metocean conditions can be allowed, so that the monopile does not fail before this value. However, this might be an overly conservative limit because it is not known if a rupture that occurs before this limit would lead to another outcome and potential tool damage. The influence of this limit will become apparent in the following chapters and the value will be discussed in detail.

3.4.2. Extraction

When extracting the monopile, it is less about finding a fixed load limit that must not be exceeded, but rather an indicator of what crane capacity is required. This determines which vessel can be used for the operation. As already described in section 3.3.1, the loads on the crane are made up of the weight of the monopile with any secondary material such as marine growth and the remaining soil friction. If the capacity of a vessel's crane is exceeded due to these loads, a vessel with a larger crane can be used. Therefore, extraction is more dependent on the operational limits of the vessel and the crane itself. These include, above all, currents and wave limits when jacking-up or positioning and wind restrictions during crane operations. These exact limits will be dealt with later in section 5.4.

3.5. Operation schedule

The software used for the schedule modelling in this thesis is ABPmer's weather downtime express (WDTX) [54]. It allows to model the operation in a sequential approach. This means that the whole decommissioning operation is made up as a task list, e.g. cutting is a task but also transit of the vessel or sea fastening of the recovered foundations. All tasks will be described in chapter 5 where the schedule modelling for two case studies is carried out. Every task in the WDTX input list has its own limits and duration. One entry in this task list, i.e. one task, consists of the following information:

- The name of the task (e.g. pile cutting operation)
- The exact location (longitude and latitude)
- The net task duration
- The weather window needed
- Wave height/period limits
- Wind speed limit (with a reference height)
- Current velocity limit (depth-averaged)

More limits can be defined, like "daylight working only" for example. However, for the work at hand the mentioned limits are sufficient. Most of the time, the wave limits are only characterized by a wave height and not together with an associated period. This way all waves exceeding this height are not allowed, regardless of their period. Since the vessel cannot carry all monopiles of a wind farm, multiple trips are needed. The input file can be created for one trip and then simulated for any number of trips.

Due to the sequential approach, a task can only be carried out when the previous task is completed. This leads to accurate estimations of the total duration and weather downtime. The software uses a hindcast database that dates back to January 1979 to produce statistical results of the total duration and weather downtime. Since WDTX uses historical data and not weather forecasts, the input limits can be given as the operational limits with α =1. The results are related to the starting date and to the probability of non-exceedance. The starting date has an influence in the sense that marine operations normally have much less weather downtime in summer than in winter. The probability of non-exceedance describes the probability that the specified duration of the weather downtime is not exceeded. In RWE, the modelling of marine operations is usually based on a probability of non-exceedance of 50% (P50). To have consistent and comparable results, P50 is also used as the main probability for the evaluation in this thesis.

3.6. Simulations overview

The simulations carried out with the above models can be divided into three parts: the validation of the model, the parameter study and the application to specific case studies.

3.6.1. Validation

In order to evaluate the model with regard to the results produced, the Amrumbank met mast, which has already been decommissioned, is considered once again. It is known from the project that the monopile broke off at the end at a cutting progress of around 98% to 98.6%. Furthermore, the structural parameters and the sea state that led to failure are known. In Table 3.4, these are summarized again.

Table 3.4: Parameter set of the Amrumbank met mast monopile.

Variable	Value	Variable	Value
Water depth d	23 m	Pile diameter D	3.5 m
Sea water density ρ_{sw}	1025 kg/m^3	Wall thickness t_w	78 mm
Significant wave height H_s	1.5 m	Steel density ρ_s	7850 kg/m^3
Wave period T_p	10 s	Cutting depth d_c	2.8 m
Current velocity u_c	1 m/s	Pile top below MSL $z_{c,1}$	0 m
Gravity g	9.81 m/s^2	Marine growth thickness t_{mg}	80 mm

With the above parameters, the Amrumbank case can be calculated with the created model. This involves checking whether the model predicts the same cutting progress before the monopile breaks. In addition to comparing the model with reality, a modal analysis will also be carried out. This gives an indication of whether the assumption of the static analysis for the maximum forces is sufficient or whether the potential dynamic movement of the pile should also be considered.

3.6.2. Parameter study

Once the cutting model has been successfully validated, it will be analysed further by conducting a parameter study. Different parameters are varied and the influence of these variations on the results is presented. This will give an impression of which are the most important or critical parameters when cutting and extracting monopiles. A base case is defined beforehand, from which the parameter variations start. The parameters of the base case can be found in Table 3.5. It will be seen later that these parameters are already orientated towards the case studies carried out afterwards.

Table 3.5: Parameter set of the base case.

Variable	Value	Variable	Value
Water depth d	25 m	Cutting depth d_c	3 m
Sea water density ρ_{sw}	1025 kg/m^3	Pile top below MSL $z_{c,1}$	5 m
Significant wave height H_s	1 m	Marine growth thickness t_{mg}	80 mm
Wave period T_p	8 s	Marine growth density ρ_{mg}	1400 kg/m^3
Current velocity u_c	0 m/s	Sand friction coefficient β	0.46
Gravity g	9.81 m/s^2	Sand buoyant weight γ_s'	10 kN/m^3
Pile diameter D	5 m	Clay undrained shear strength s_u	50 kPa
D/t ratio	80	Clay buoyant weight γ_c'	12 kN/m^3
Steel density ρ_s	7850 kg/m^3		

The parameters that are varied are shown in Table 3.6. The variation range is also displayed. The ranges were chosen to be as wide as possible in order to cover many of the currently operating wind farms. However, it must be noted that only one parameter is changed at a time when analysing the parameter influence. It is therefore possible that some parameter variations do not provide a realistic set.

Table 3.6: Variables varied during parameter study.

Variable	Range	Variable	Range
Cutting depth d_c	3 m ... 6 m	D/t ratio	60 ... 100
Current velocity u_c	0 m/s ... 2 m/s	Water depth d	15 m ... 50 m
Pile top below MSL $z_{c,1}$	0 m ... 6 m	Significant wave height H_s	0.5 m ... 2 m
Pile diameter D	4 m ... 8 m	Peak period T_p	4 s ... 12 s

3.6.3. Case studies

After the detailed analysis with the help of the parameter study, the case studies are used to perform the computations for realistic parameter sets. In this way, the cutting and extraction of monopiles can be calculated for two real wind farms. The two wind farms are Robin Rigg and Galloper, both in waters of the United Kingdom. These case studies are described in more detail in chapter 5. For the two wind farms, following the above calculation, where any operability limits for cutting and extraction have been determined, the schedules of the decommissioning plans are also calculated. This makes it possible to estimate how long the operation will take in total and how much of this time is caused by waiting on weather.

4

Model validation and parameter study

In this chapter, the developed model is first validated with the help of a decommissioning project that has already been carried out. Furthermore, the modal analysis is performed to analyse the potential increasing dynamic behavior of the model with cutting progression. Subsequently, the model is examined in depth by conducting a parameter study. This helps to determine the parameters to which the model reacts most sensitively. The chapter ends with a discussion of the results.

4.1. Validation of the cutting model

As described above, the decommissioning project of the Amrumbank metmast is used to validate the model. The calculations were carried out using the Amrumbank parameters and the weather data at the time of the operation. The results can be seen in Figure 4.1.

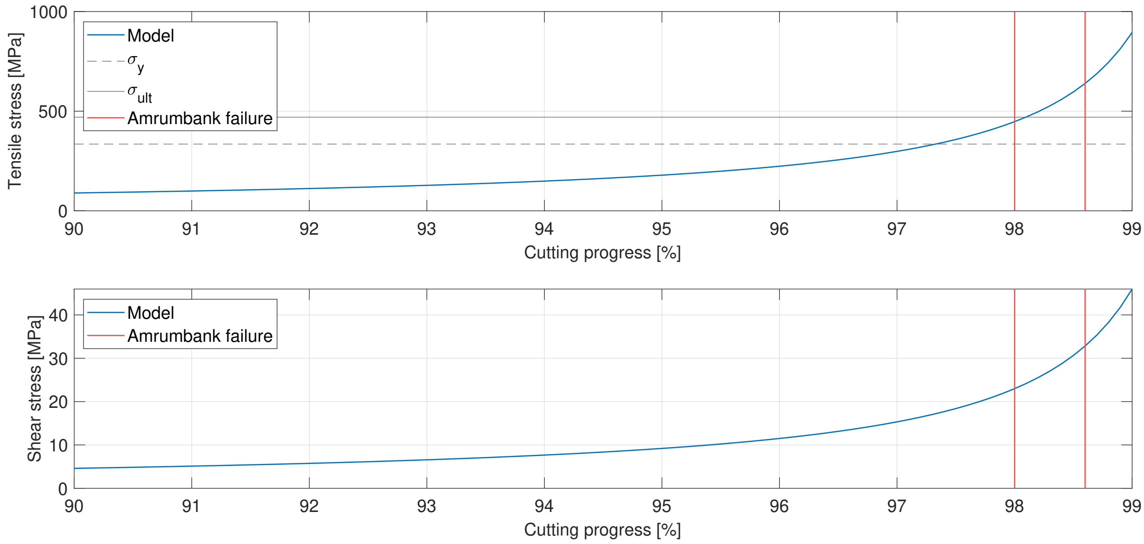

Figure 4.1: Stress calculation results for the Amrumbank met mast monopile.

The upper plot shows the tensile stress development in the uncut section under tension as the cut progresses, calculated as described in subsection 3.2.2. The cutting process is shown from the 90% to 99%. The yield strength σ_y and the ultimate tensile strength σ_{ult} of the material are also shown. The lower plot shows the shear stress development in the three uncut sections. The two vertical red lines show the estimated cutting progress when the monopile of the Amrumbank met mast broke free. Two main observations can now be made.

Firstly, the tensile stresses are generally many times greater than the shear stresses, by a factor of around 20. Tension is therefore the main type of stress that leads to failure of the uncut sections. Secondly, in the case of the Amrumbank met mast, this failure occurred at a cutting progress between 98% and 98.6% (see red lines). It can be observed that also with the analytical model a cutting progress in this range leads to reaching the ultimate tensile strength, which indicates a failure of the component. The exact calculated cutting progress that leads to reaching the ultimate tensile strength is 98.1%. Therefore, the model predicts behaviour similar to that observed in reality.

Above, only the largest loading of the calculated time series of loads was used to determine the stresses. However, this assumes that this value occurs just when the critical cutting progress of 98% to 98.6% is reached. To show how often a value that increases the ultimate tensile strength for the critical cutting progress is reached within the time series, it is depicted in Figure 4.2.

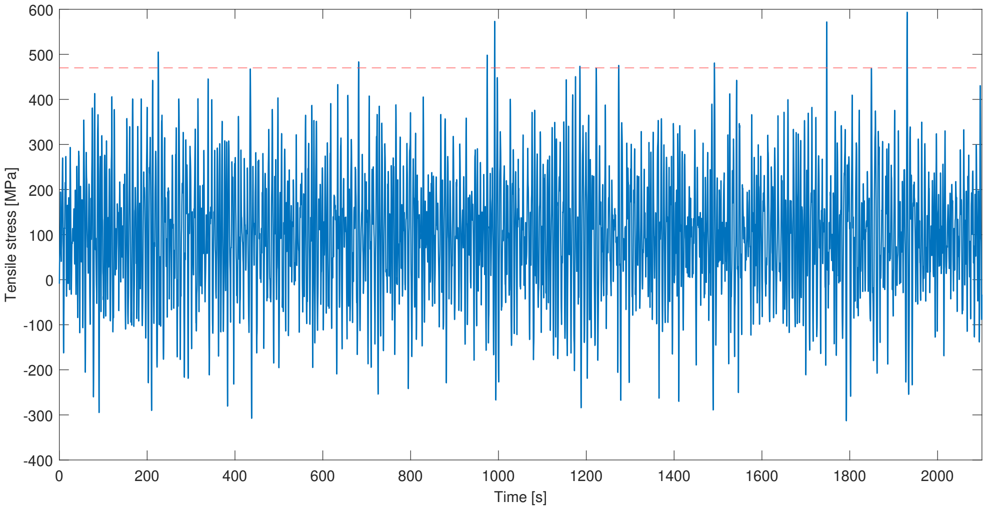

Figure 4.2: Time series of the tensile stress for the critical cutting progress.

The time series has the length that it takes to cut 10% of the monopile because it was decided that only the last 10% are of interest for the pile's stability (see subsection 3.2.1). It can be observed that the ultimate tensile strength during this time series is not reached only once by the largest loading but in total is reached 12 times. This shows that it is likely that such a load also occurred between 98% and 98.6% cutting progress which resulted in the failure of the monopile. These observations are further discussed in section 4.3. Nevertheless, in the further course of the work, only the highest load during the time series is used for the calculation in order to maintain the conservative approach and to determine the earliest possible time of failure.

The calculations of the stresses above were made neglecting the pressure from the self-weight of the monopile. This was done because during cutting, the crane is connected to the pile with 80% of the pile's weight in the hook. The calculation of the pressure in the uncut sections increases with progression of the cut and works in the opposite direction of the tensile stress. However, calculating the pressure for the determined failure point of 98.1% results in a value of 8.74 MPa. Compared to the ultimate yield strength of 470 MPa and the rate of change at around 98.1% cutting progress, the pressure is very small.

Regarding the modal analysis, the first two different mode shapes are considered, i.e. the two with the lowest eigenfrequencies. Figure 4.3 presents these shapes. The analysis is limited to two modes because already the third mode has a significantly larger corresponding eigenfrequencies than the first and second mode. As stated before, usually the modes with the lowest frequencies are governing for the real oscillation shape.

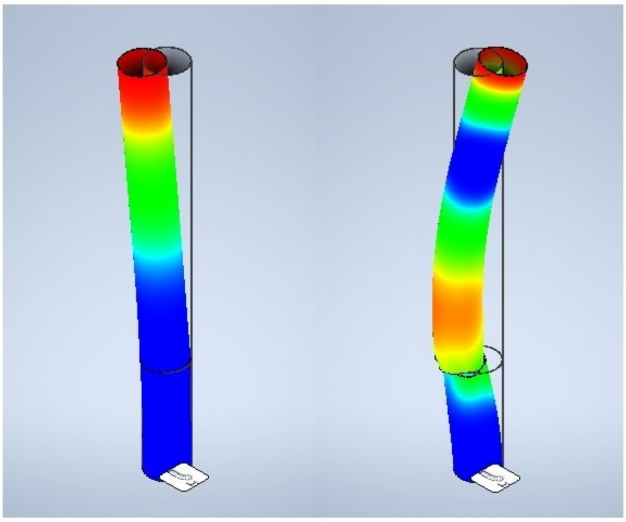

Figure 4.3: Mode shapes of the Amrumbank met mast monopile.

The first mode is a simple fore-aft motion of the monopile. In theory, there are three of these modes due to the symmetry with three uncut sections. The second mode is a more complex bending motion. Throughout the cutting progress, a significant change in the shape of the modes does not appear. Figure 4.3 shows the mode shapes for a cutting progress of 98%. In section C.1 in the appendix, the mode shapes of the uncut pile can be seen for a comparison. The eigenfrequencies corresponding to the two depicted modes and their development with the progression of the cut is presented in Figure 4.4.

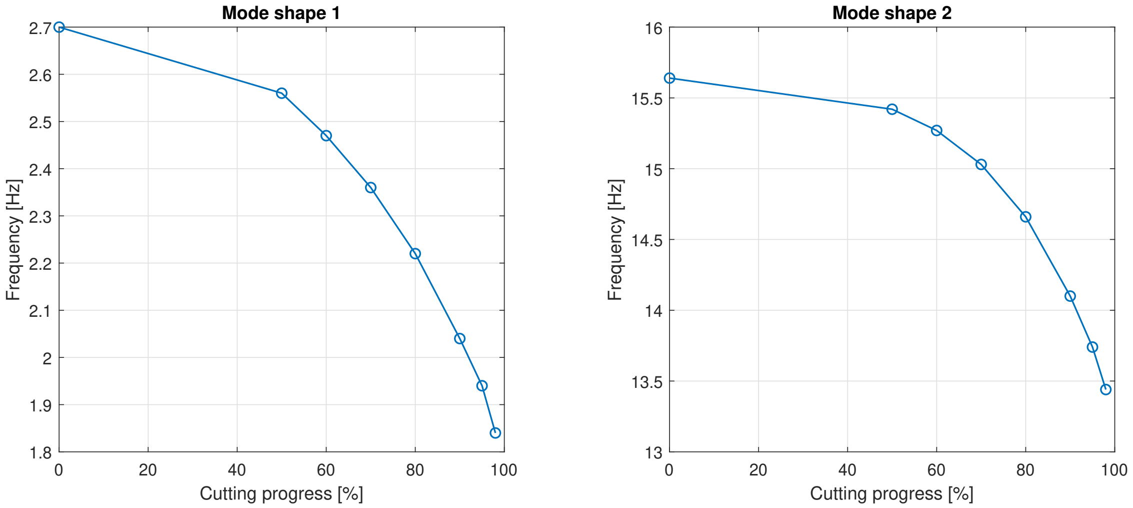

Figure 4.4: Modal frequencies of the Amrumbank metmast monopile.

It can be observed that the modal frequencies generally decline with a similar trend when the cutting progresses. This means that the monopile is becoming less stiff when it is cut. The frequency of the first mode shape is 2.7 Hz when the pile is uncut and reduces to 1.84 Hz when the pile is cut to 98%. The gradient of the curve increases considerably with increasing cutting progress. For the second mode shape, the associated frequency is 15.64 Hz for an uncut monopile and decreases to 13.45 Hz at 98% cutting progress. The considered waves in this thesis have periods between 4 s and 12 s, which corresponds to frequencies between 0.083 Hz and 0.25 Hz. Even with a cutting progress of 98%, these frequencies are still more than 7 times lower than the lowest natural frequency of the monopile. Hence, the stiffness of the monopile is still considerably large when compared to the wave excitation frequencies.

The influence of the mesh density on the results of the modal analysis is now analysed. Figure 4.5 presents the eigenfrequencies for the two considered mode shapes, calculated with five different mesh densities. The base value is a mesh with an average element size of S_e equal to 0.08 of the frame length. Then, meshes with elements with average sizes twice ($S_e/2$), four times ($S_e/4$), eight times ($S_e/8$) and 16 times ($S_e/16$) smaller are used. The minimum element size around the cut always is a fifth of the average element size.

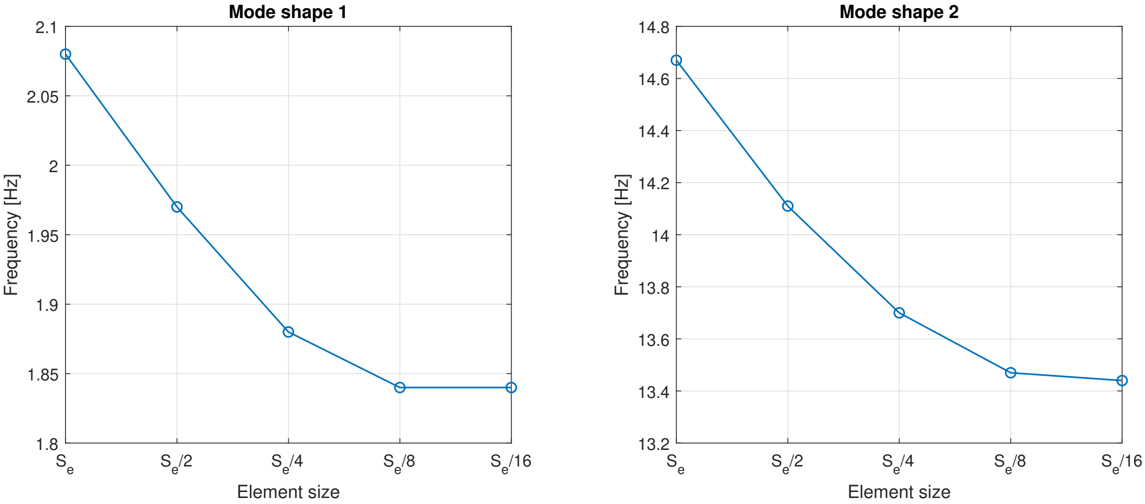

Figure 4.5: Convergence study for the Amrumbank met mast monopile.

Above, the results of the mesh study are presented for a cutting progress of 98% since this is deemed the critical value. If the results converge for 98%, they will do for the lower cutting progresses as well, as the same meshing is used. Convergence can be observed, since for the results obtained using elements with average sizes of $S_e/8$ and $S_e/16$, little to no difference can be observed. For the first mode shape the frequencies are the same and for the second mode shape the difference in the frequencies is 0.2%.

4.2. Parameter study

The parameter study is now performed. Only the calculation of the maximum stresses and the extraction loads on the hook are calculated. Due to the complex adaptation of the FEM model to each new parameter, the long calculation time and the results for Amrumbank, the modal analysis is not performed in the parameter variation. However, it is carried out again for the case studies in chapter 5. Due to the simplicity of the analytical model and its good adaptability, many simulations with a single parameter change can be carried out effectively. First, the base case is analysed with the parameters listed in Table 3.5. Then, the parameter variations are carried out as described in Table 3.6.

4.2.1. Base case

The base case serves as the starting and comparison point for the parameter variations. Compared to the Amrumbank met mast, the base case differs primarily in its larger diameter of 5 m and its smaller wall thickness. It is also important that the Amrumbank met mast monopile protruded from the water, as no transition piece was installed. In the base case, it is assumed that the pile ends 5 m below the water surface due to the previous cutting down of the transition piece. The sea state is also selected to be lower with a significant wave height of 1 m and a period of 8 s. A current is not yet taken into account in the base case. However, the water and cutting depths are initially selected similarly. Figure 4.6 shows the results for the tensile and shear stresses as the cutting progresses.

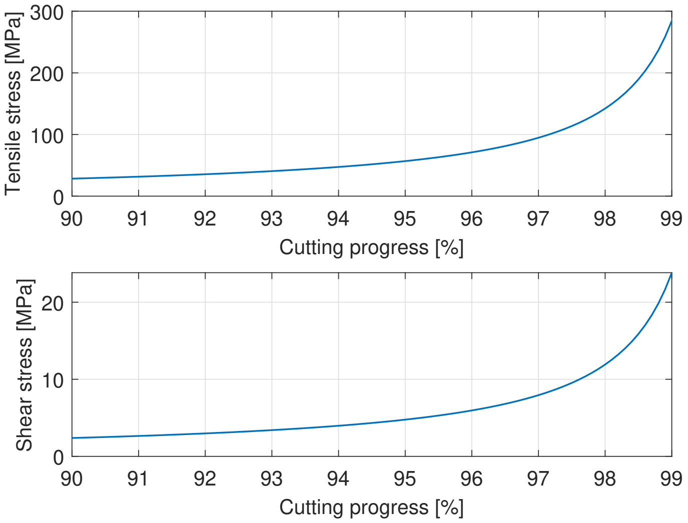

Figure 4.6: Stress calculation results for the base case of the parameter variation.

It can be observed that the stresses in this case are lower than for the Amrumbank met mast. At the minimum value of 98% to be reached before the pile is allowed to break, the tensile stress is around 150 MPa, which is well below the material limit of 470 MPa. The pile can therefore be considered stable at this point. As before, the shear stress is significantly lower, even if the factor is only 10 (previously 20). From now on, the extraction loads for the hook are also considered, as these also depend on the varied parameters. These are always shown as bar or area diagrams, once for sand and once for clay. The results for the base case can be seen in Figure 4.7.

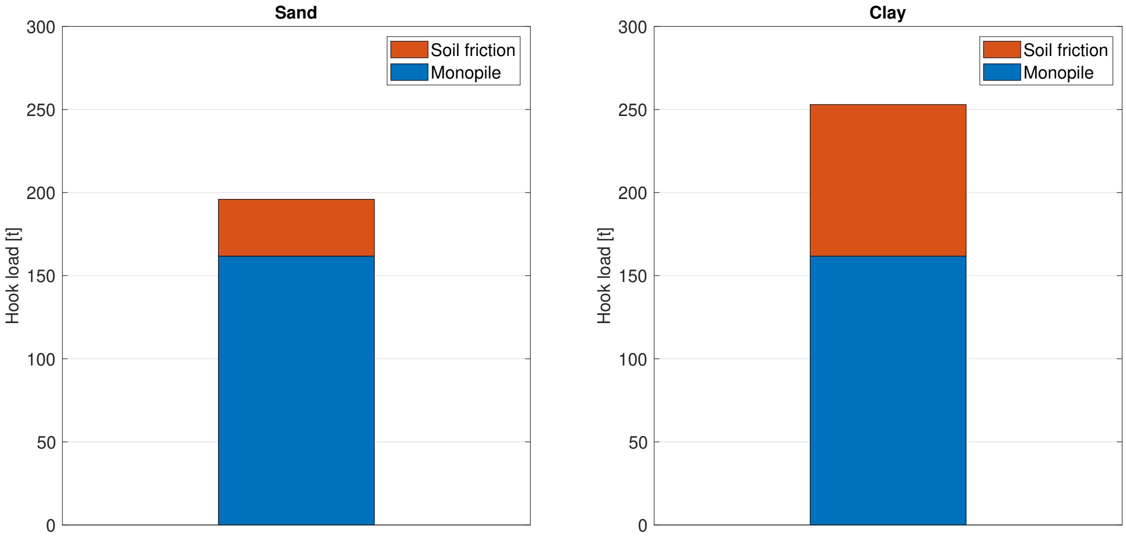

Figure 4.7: Hook load calculation results for the base case of the parameter variation.

It can be seen that, regardless of the soil type, the main hook load is caused by the weight of the monopile. In the base case, this is approximately 160 t. The friction that clay exerts on the pile is almost three times greater than that of sand, at around 95 t, resulting in a total hook load of around 250 t. The total hook load in sand is around 200 t.

4.2.2. Cutting depth

The first parameter variation covers the cutting depth below the seabed. Figure 4.8 shows the tensile stress curve with varying cutting depth at the critical cutting progress of 98% on the left and the curves for three different cutting depths starting from 90% on the right. The shear stress is not shown as it does not change.

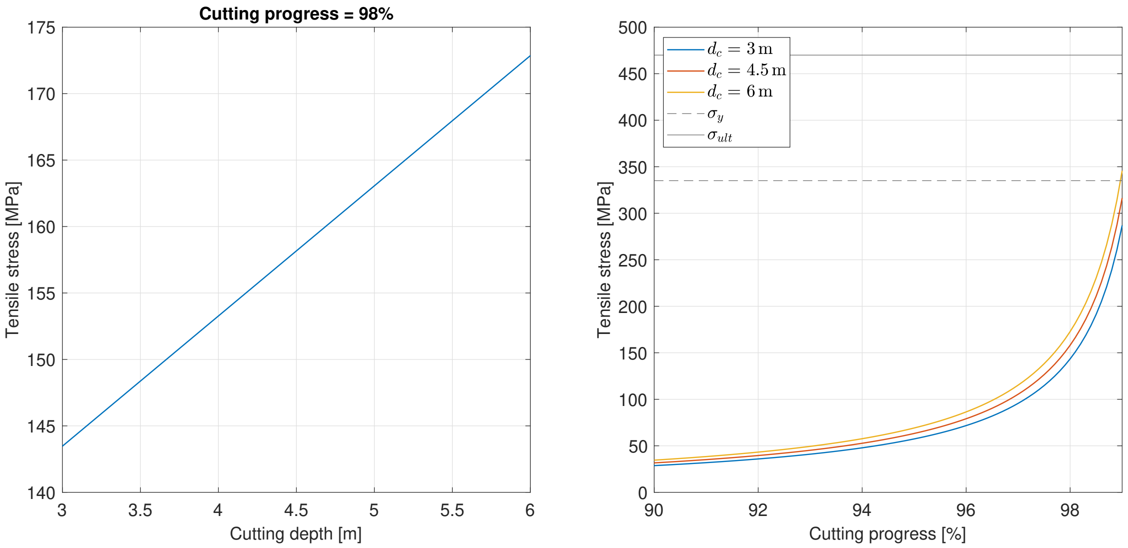

Figure 4.8: Stress calculation results for varying cutting depth.

In the left plot it can be observed that the tensile stress increases linearly with the cutting depth, from just under 145 MPa at 3 m below the seabed to just over 170 MPa at 6 m. This results from the linear moment line in the model (see Figure 3.6). In the plot on the right, it is easy to see that the effects of the different cutting depths only make small differences in the tensile stresses. Therefore at 98% cutting, the critical material limits are not reached. In comparison with the influence of the cutting depth on the stresses in the cut, the influence on the hook load is much larger, which is presented in Figure 4.9.

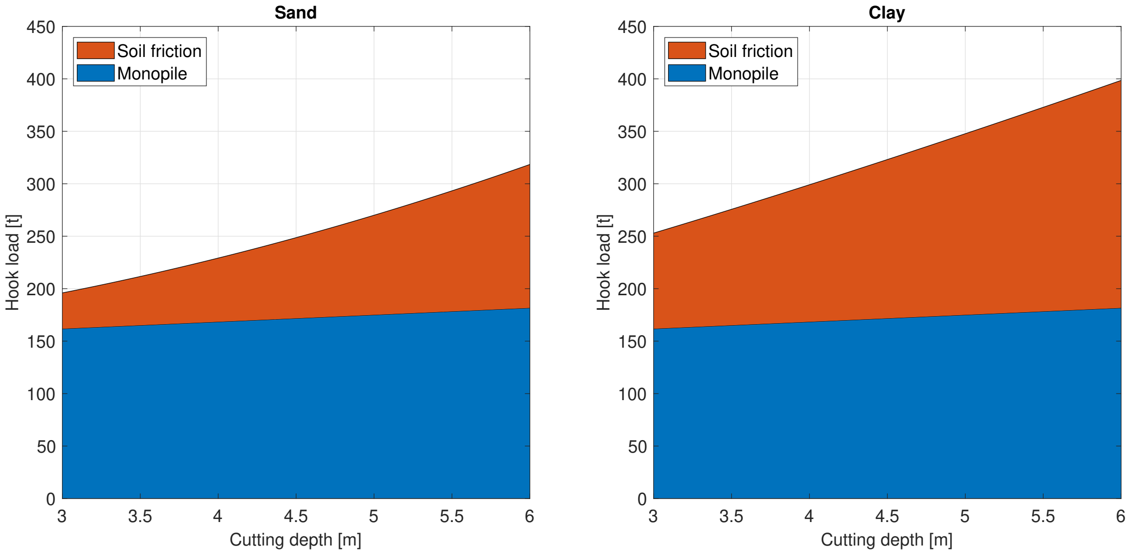

Figure 4.9: Hook load calculation results for varying cutting depth.

In sand, the load increases significantly due to soil friction, from 35 t at a cutting depth of 3 m to 140 t at a cutting depth of 6 m. An even greater increase can be observed in clay, from 95 t to approx. 220 t.

In both soil types, a slight increase in the load caused by the monopile weight can also be observed. This is due to the removed pile becoming longer with the cutting depth.

4.2.3. Current velocity

The second parameter variation deals with the influence of a constant current speed. Figure 4.10 shows the tensile and shear stresses, for the constant cutting progress of 98% and for three different current velocities with varying cutting progress starting from 90%.

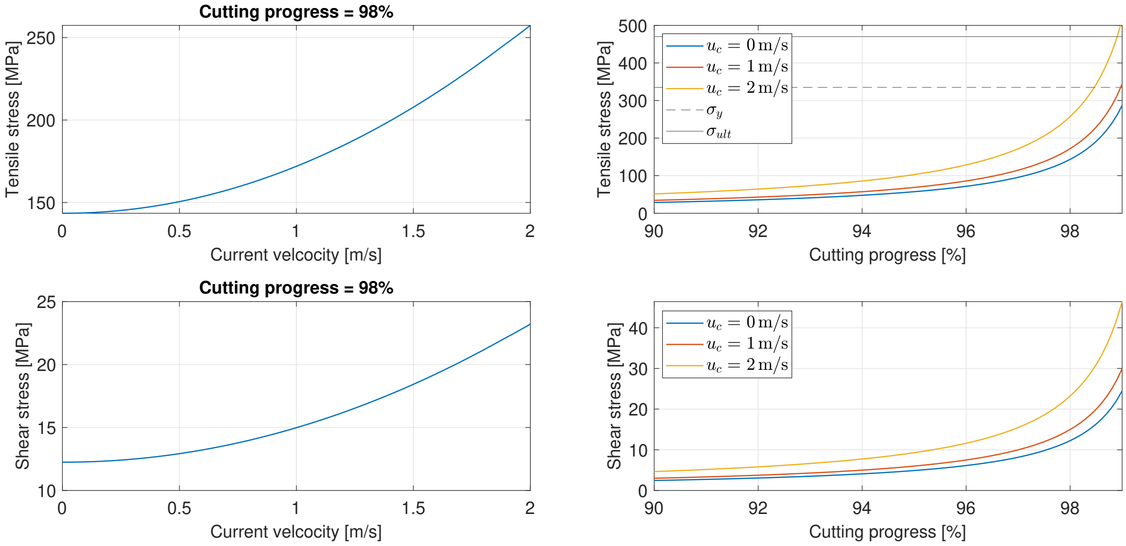

Figure 4.10: Stress calculation results for varying current velocity.

The plots on the left show that the current velocity has a quadratic influence on both types of stress. This can be explained using the Morison equation (see Equation 3.2), where the drag term is proportional to the square of the fluid's velocity. The Keulegan-Carpenter number (see. Equation 3.4) is 3.25 at a current velocity of 2 m/s. This indicates that the influence of the drag term is rather small. Nevertheless, the critical tensile stress increases from below 150 MPa without a current to over 250 MPa at 2 m/s. Within the same range, the shear stress increases from 12 to 24 MPa. The two plots on the right show the quadratic influence once again. From 0 to 1 m/s the curves are still quite close. For a flow velocity of 2 m/s, however, significantly higher stresses can be recognised. Overall, the material limits are not reached at 98% cutting progress.

4.2.4. Part of monopile below MSL

Now the influence of the highest point of the monopile being below the water surface will be analysed. As explained before, this is the case when the transition piece of a monopile has to be cut off first. Figure 4.11 shows the results for the tensile and shear stress calculations. On the left are the stress curves for a monopile whose top is between 6 and 0 m below the sea surface at a cutting progress of 98%. On the right are the stress curves from a progress of 90% onwards for three different distances.

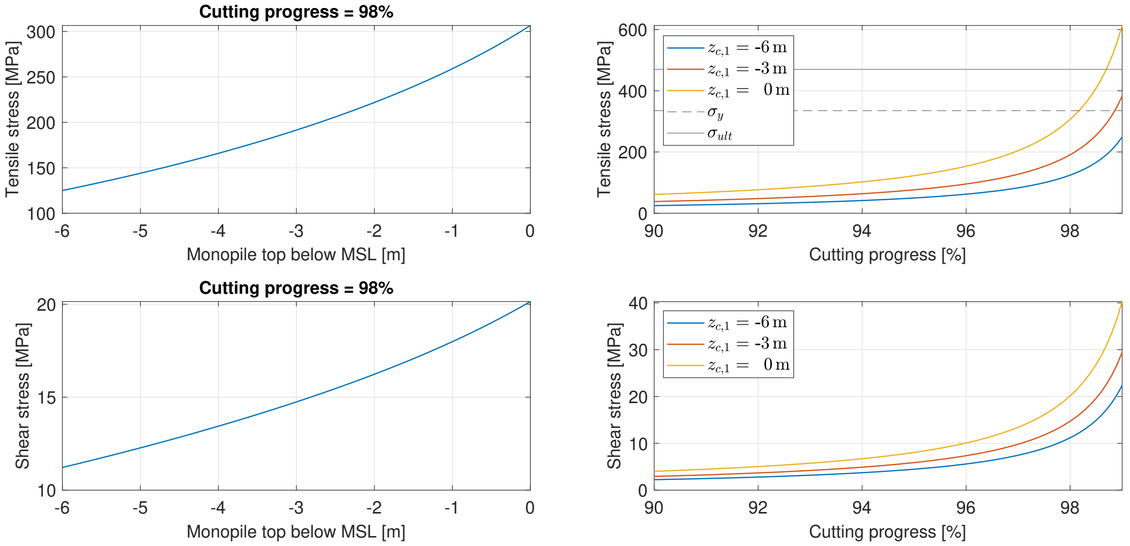

Figure 4.11: Stress calculation results for varying depths of the monopile top.

It can be observed that the stresses increase significantly when the tip of the monopile is close to the water surface. The tensile stress at 98% increases from 130 MPa to 310 MPa and the shear stress from 12 MPa to about 20 MPa. This can also be seen in the plots on the right, as the stress curves for 6, 3 and 0 m differ significantly. This can be attributed to the fact that the wave forces are greatest just below the water surface. In Figure 3.6 the distribution of the hydrodynamic load with the water depth was already shown. It is clear to see that most of the force is applied just below the surface of the water. If the upper part of the pile is cut off, these forces are not taken up by it.

Since the pile becomes longer if it extends to just below the water surface, this increases the amount of the monopile weight in the hook load. This can be seen in Figure 4.12. The increase of the monopile weight is around 40 t from the top being 6 m below the MSL to the top protruding the MSL. The frictional force generated by the soil remains unchanged by this parameter variation.

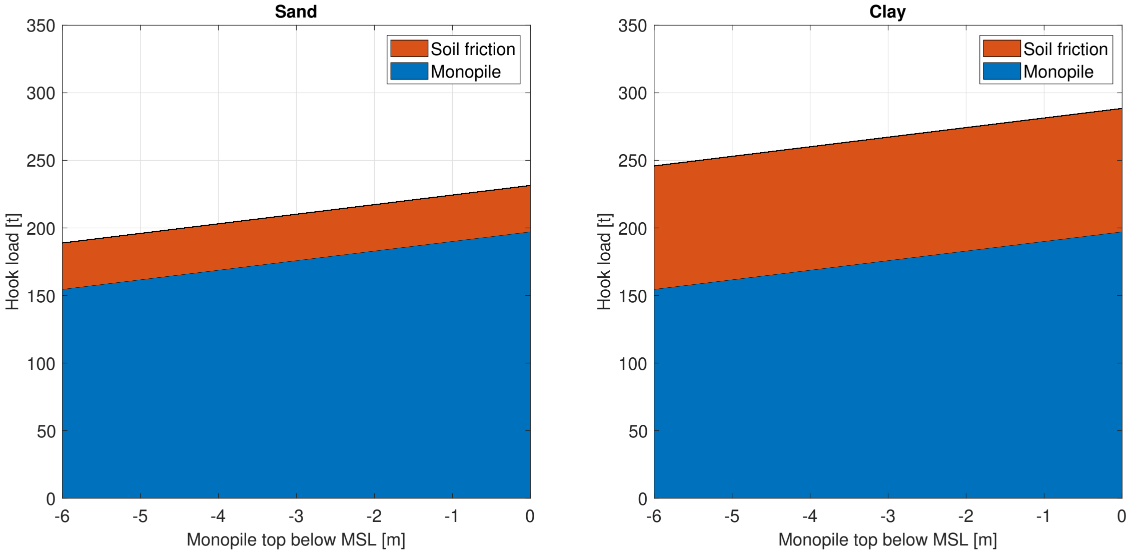

Figure 4.12: Hook load calculation results for varying depths of the monopile top.

4.2.5. Monopile diameter

The next parameter to be varied is the monopile diameter. Figure 4.13 again shows the two stress curves with varying diameter at constant cutting progress of 98% on the left side. The plots on the right show the curves for three different diameters starting from a progress of 90%.

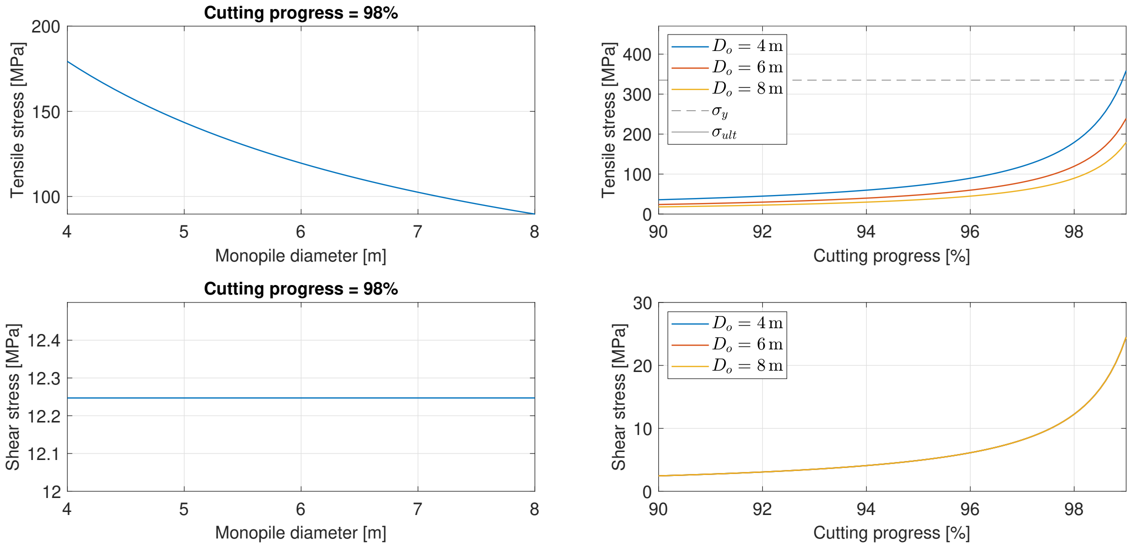

Figure 4.13: Stress calculation results for varying outer diameters.

It can be observed that the tensile stress decreases with increasing pile diameter, namely from 180 MPa at 4 m to around 90 MPa at 8 m for a cutting progress of 98%. The shear stresses, on the other hand, do not change with increasing diameter. To investigate these phenomena in more detail, Figure 4.14 shows the axial and horizontal forces causing the tensile and shear stresses, as well as the areas taking up these forces, with varying diameters at a cutting progress of 98%.

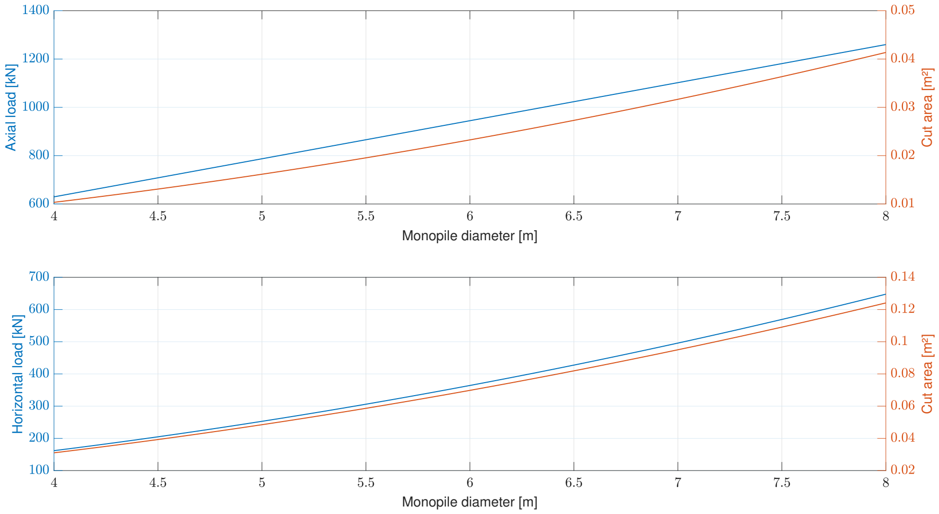

Figure 4.14: Trends of loads and cut areas with varying outer diameter.

It can be observed that the axial load that causes the tensile stress grows quite linearly with an increasing monopile diameter, whereas the area of the cut that has to take up the axial load grows quadratically with the monopile diameter. This explains the decrease in the maximum tensile stress when increasing the monopile diameter. However, the horizontal load is also growing quadratically with the area of the cut surface. This leads to the constant shear stress observed in Figure 4.13. Here, the cutting progress was kept constant at 98%. To additionally show how this behaviour changes with the cutting progress, Figure C.2 in section C.2 in the appendix is provided.

The change in diameter leads to a significant change in the extraction forces. The monopile weight and the soil friction both increase with increasing diameter (see Figure 4.15). This is particularly noticeable with the weight of the monopile. As the D/t ratio is kept constant at 80, the wall thickness increases along with the diameter. This results in an increase in monopile weight from 100 t crane load at 4 m diameter to 400 t at 8 m. The increase in soil friction is small in comparison. For sand, it grows from around 30 t at an outer diameter of 4 m to around 60 t at a diameter of 8 m. For clay it increases from around 80 t to 150 t.

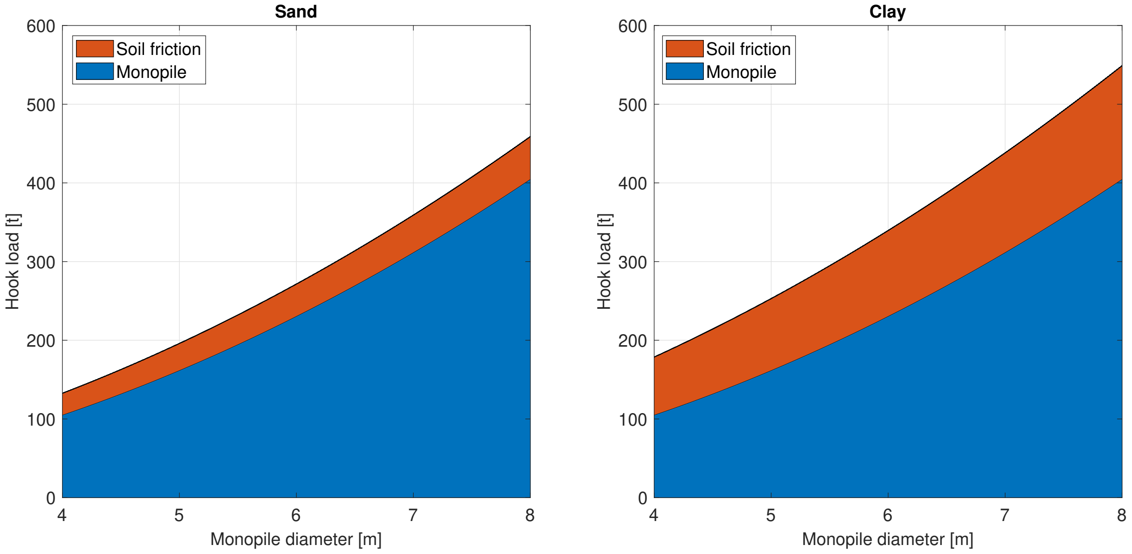

Figure 4.15: Hook load calculation results for varying outer diameters.

4.2.6. Diameter/thickness ratio

Now, the diameter is kept constant at 5 m, but the D/t ratio is changed. Smaller D/t ratios mean greater wall thicknesses and larger D/t ratios lead to smaller wall thicknesses. Figure 4.16 shows this influence on the stress curves. Left for varying D/t ratios with a constant cutting progress of 98% and right for varying cutting progress with three constant D/t ratios.

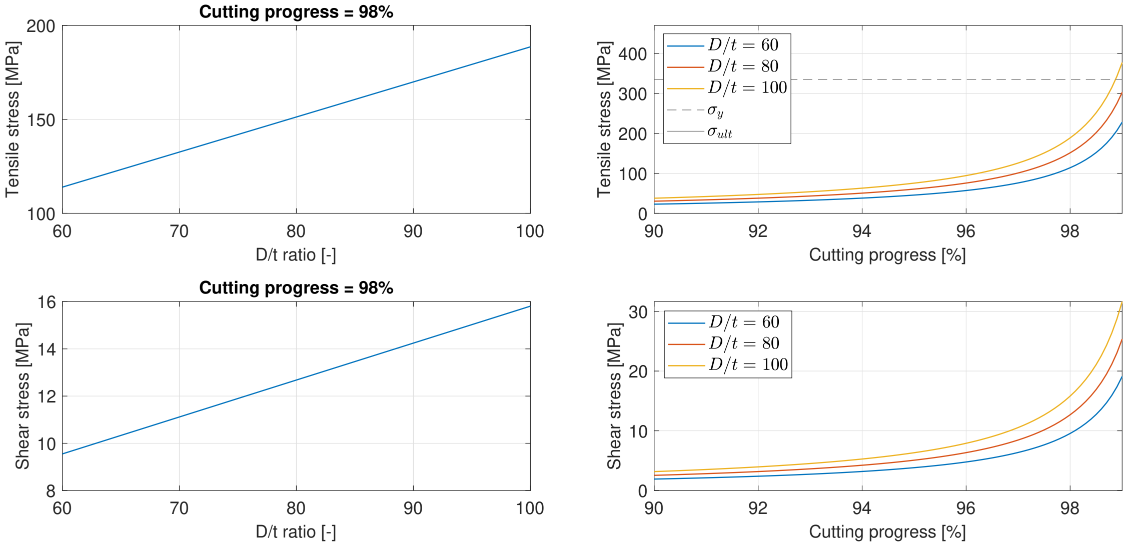

Figure 4.16: Stress calculation results for varying D/t ratios.

As the cutting area decreases with increasing D/t ratio, it can be seen that the stresses increase. At a constant cutting progress of 98%, the tensile stresses increase from 110 MPa at a D/t ratio of 60 to up to 180 MPa at a D/t ratio of 100. In the same range, the shear stresses increase from 9 MPa to 16 MPa.

With increasing D/t ratio and thus decreasing wall thickness, the weight of the monopile decreases. This is reflected in Figure 4.17, which shows that the weight of the monopile is reduced from 210 t to 130 t when the ratio is increased from 60 to 100. The soil friction is not affected by this because the outer diameter is not changed.

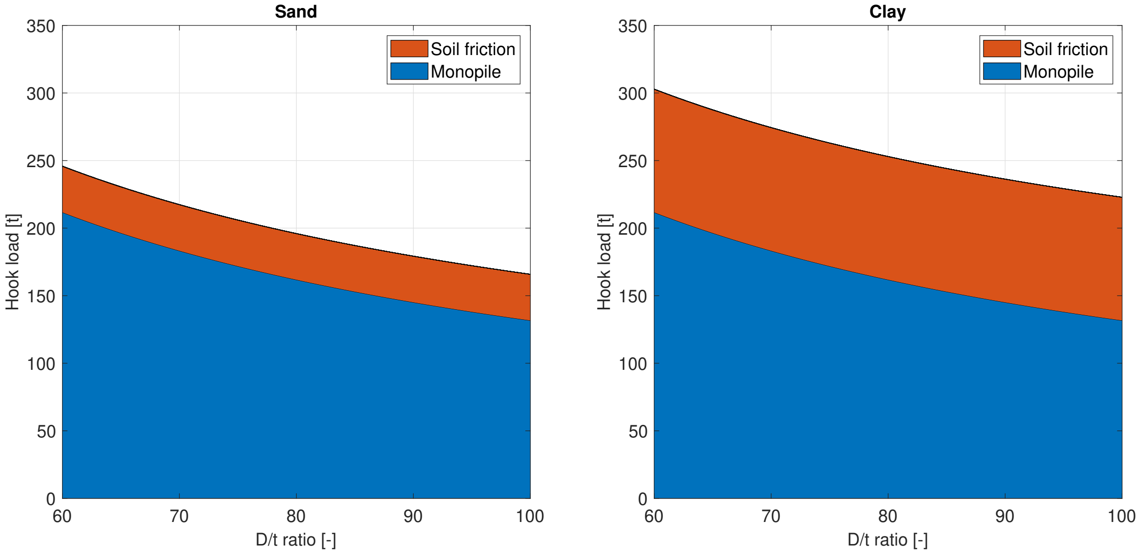

Figure 4.17: Hook load calculation results for varying D/t ratios.

4.2.7. Water depth

The influence of the water depth on the model is now analysed. Figure 4.18 shows the influence on the stresses. On the left for varying water depths with a constant cutting progress of 98% and on the right for varying cutting progress with three constant water depths.

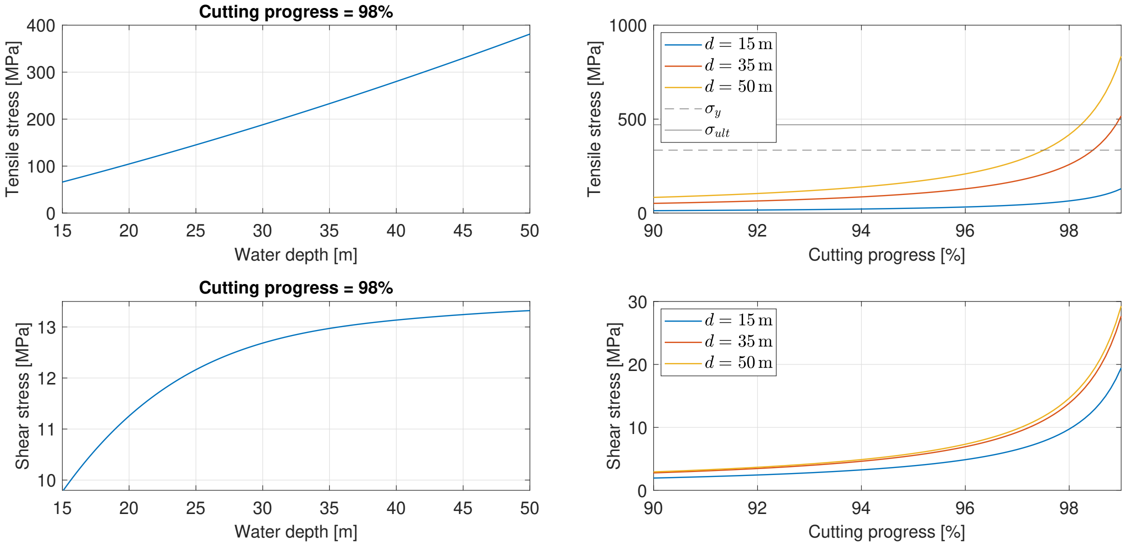

Figure 4.18: Stress calculation results for varying water depths.

It can be seen that the tensile stress increases quite linearly with the water depth, from approximately 75 MPa at 15 m depth to 380 MPa at 50 m depth. The shear stress does not increase linearly. At first it increases more strongly with the water depth, later this gradient decreases. At a depth of 15 m the shear stress is about 9 MPa, at a depth of 50 m slightly larger than 13 MPa. On the right side, it can be seen that the tensile stress reaches the yield point at just under 98% cutting progress and the ultimate tensile strength at just over 98%. In order to visualise the effects of varying water depth, especially with regard to the differences in tensile and shear stress development, the force distribution for three different water depths is shown in Figure 4.19.

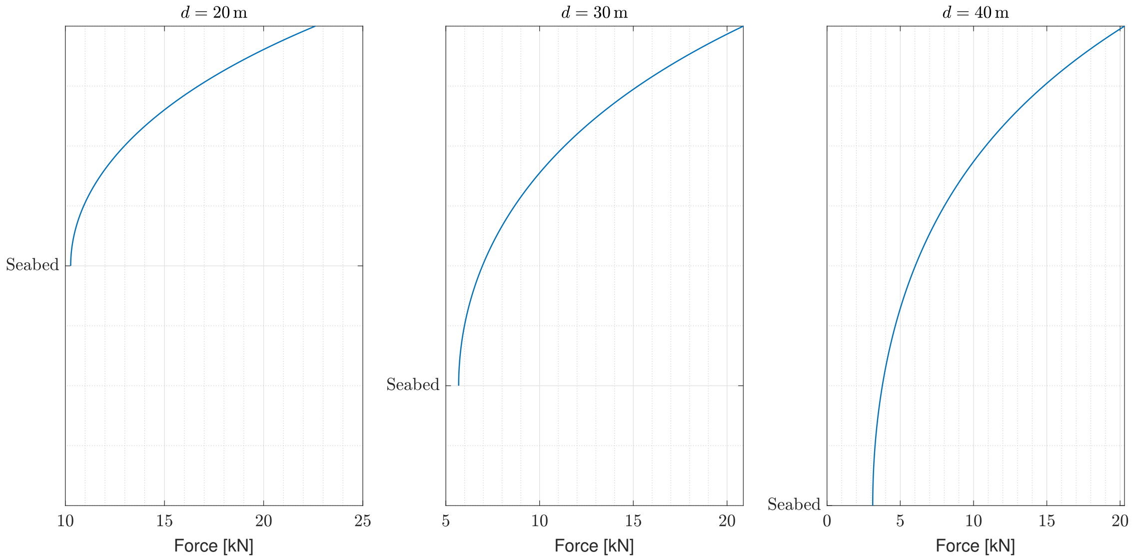

Figure 4.19: Hydrodynamic force distribution for three different water depths.

For the depth of 20 m the integrated force is 282 kN, for the depth of 30 m the integrated force is 305 kN and for the depth of 40 m the integrated force is 313 kN. The hydrodynamic force increases with the water depth but this growth becomes smaller when the depth increases. This is due to the fact that most addition only comes from the part that is close to the seabed where the forces are small anyway. At smaller water depth, the share of this force is larger compared to deeper waters, which is why the integrated force grows faster first, with a decreasing gradient. Regarding the different shape of the tensile stress in Figure 4.18, this can be explained by a mix of the larger loads and the longer lever arm of the resulting force which increases with deeper waters.

The variation in water depth also has a significant influence on the hook load. Figure 4.20 shows that although the soil friction remains the same, the monopile weight increases. As the water depth increases, the pile becomes longer and therefore heavier. This leads to an increase from 90 t at 15 m to 330 t at 50 m.

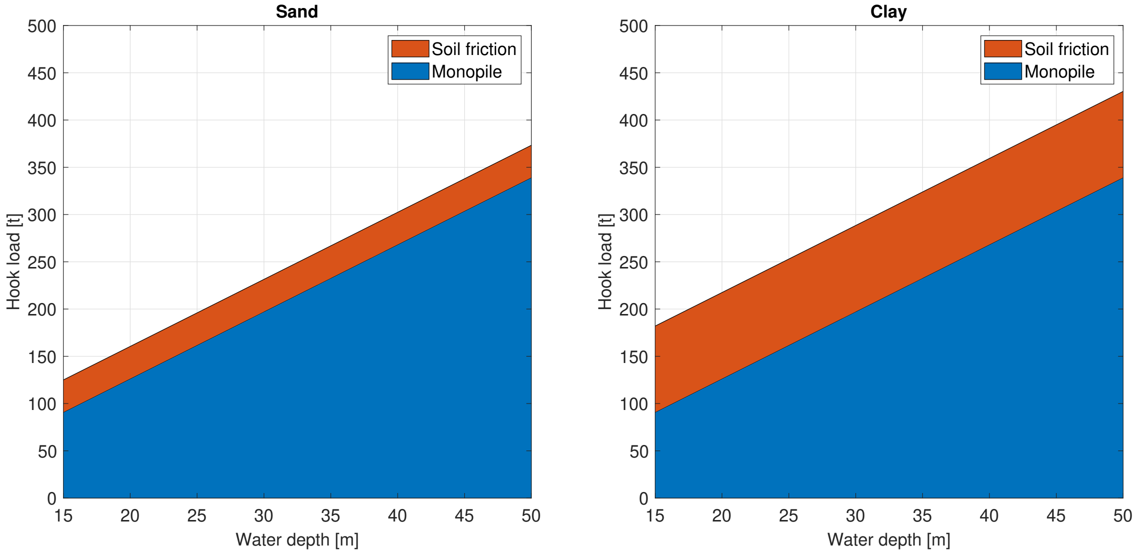

Figure 4.20: Hook load calculation results for varying water depths.

4.2.8. Sea states

The last parameters to be analysed are the significant wave heights and peak periods, which together describe the sea states. Figure 4.21 shows two maps on the left side, which describe the tensile stress and the shear stress at a constant cutting progress of 98%. Maps are used because two parameters were varied simultaneously, the significant wave height from 0.5 m to 2 m and the peak period from 4 s to 12 s. On the right, the stress curves for a cutting progress from 90% are depicted, specifically for three different sea states (H_s & T_p combinations).

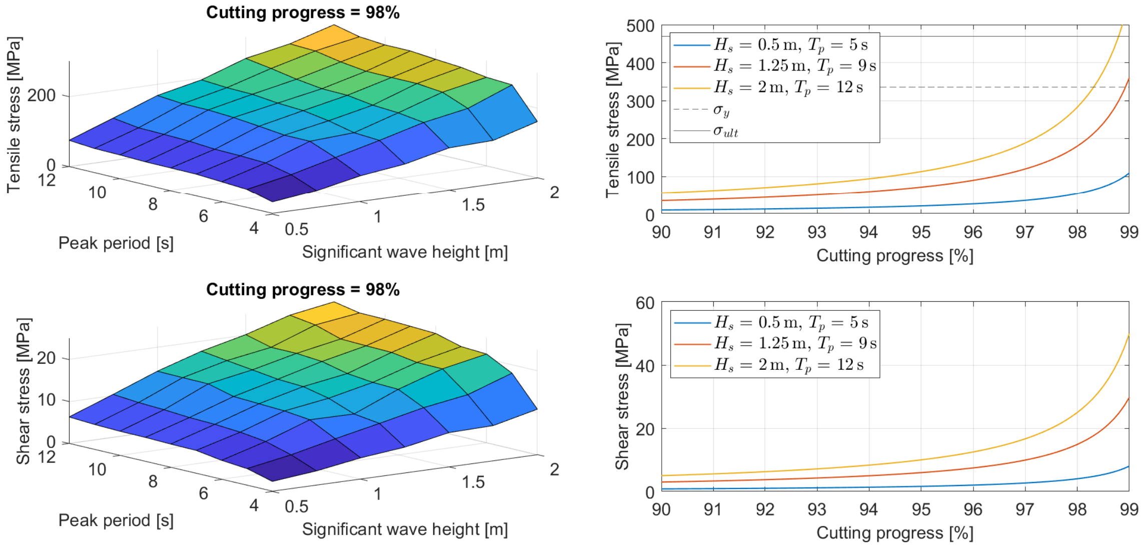

Figure 4.21: Stress calculation results for varying sea states.

It can be seen that increases in wave height and increases in peak period both lead to larger stresses. The tensile stress increases from approximately 50 MPa at a wave height of 0.5 m and a period of 4 s to 280 MPa at a wave height of 2 m in combination with a period of 12 s. The shear stress increases from around 3 MPa at a wave height of 0.5 m and a period of 4 s to approximately 25 MPa at a wave height of 2 m in combination with a period of 12 s. However, the material-critical values in the base case are not reached before 98%, even in the worst weather conditions (yellow line). It must be noted that only the sea states were varied. In combination with other parameter changes that also showed to increase the stresses, it might be that the ultimate tensile strength is reached before. As stated before, realistic parameter sets are analysed in chapter 5.

4.3. Discussion

This section contains an initial discussion of the modelling and results. There are two discussion sections in total, the first here and the second at the end of chapter 5. This approach was chosen because some topics should already be discussed after this chapter. The next chapter has its own topics, which can only be discussed then. The topics in this first discussion include the assumptions used in the stress calculation, the validation of the stress calculation, the modal analysis, the calculation of the extraction forces and the parameter variations. Each of these topics will have its own paragraphs in the following text.

Assumptions used in the stress calculation
In order to calculate the stresses in the uncut sections, the hydrodynamic maximum forces were first determined. For this purpose, irregular waves and their forces were calculated using standard methods (see section 3.1). The Morison equation was used and for short waves also the MacCamy-Fuchs correction was applied. However, the maximum forces were found to occur in long waves and were therefore calculated with the Morison equation only. As these equations are very well established, the force calculations themselves are considered reliable and will not be discussed further here. However, the duration of the time series and the resulting maximum forces must be considered in more detail. The stress calculation was performed by taking the maximum force from ten time series. The duration of the time series has an influence on this maximum force. The longer the time series are selected, the greater is the probability that an even larger maximum force will be present. However, in operations such as the cutting operation, where only a short situation, in this case shortly before the end of cutting, is of the greatest interest, it is too conservative to take the entire length of the operation as a time series. Therefore, the time it takes to cut the last 10% of the pile was taken as the time series. The results have shown that even the duration of the last 10% is still a conservative estimate, as no critical stresses occur at a cutting progress of 90%. Due to this, a shorter time series may also be sufficient for the calculation of the max loads.

The determination of the stresses in the cut was carried out using a simplified analytical calculation. The reasons for this are manifold. Firstly, this topic is very new, so there were no references on how to calculate the stresses in the best possible way. Therefore, the easiest method to implement was used initially. In addition, the analytical calculation can be adapted very easily, which is important for the parameter variations. The simplifications made will now be evaluated. Firstly, the effective fixity model was used. As this is widely used in industry, can be applied at the depth at which the cut is present and is considered reliable in terms of load and stress calculation in the foundation, its use makes sense. The moment in the cutting plane was divided equally between the two sides of the pile which are either loaded under pressure or tension. This means that the tensile forces have the same magnitude as the compressive forces. However, the loading direction is assumed in a way that the compressive forces are taken by two uncut sections and the tensile forces only by one. This way the worst case is depicted, as the stresses in the tensile loaded uncut section are as large as possible. So, a conservative approach was taken again. During a progress meeting for this thesis a mistake in the calculation of the tensile and compressive forces was found. The correct calculation is applied in this work. However, in section A.5 in the appendix the wrong calculation and the impact are presented. The greatest simplification was made by constantly distributing the stresses in the uncut sections across the cross-section. At the beginning of the cut, this assumption is not optimal, as the uncut sections are still quite large and therefore some areas are significantly closer to the centre than others. However, as the cut progresses, the sections become smaller. At the critical cutting progress of around 98%, the maximum and minimum distances to the centre within an uncut section are so small that this simplification is a good approximation (see Table 3.1). However, if the stresses need to be calculated at much smaller cutting progresses, other calculation methods should be used, e.g. an FEM analysis to determine the variations in stresses across the cross-section. This could be the case if very severe sea states with larger hydrodynamic loads leading to earlier failure are to be considered. The sea states considered in this work with maximum significant wave heights of 2 m result in loads that only lead to failure very late in the cutting process, which can be calculated well with the assumptions made.

As the failure criterion, the reaching of the ultimate strengths of the material was assumed. With the analytical calculation approach, the complex material behaviors that are shown in section A.3 in the appendix cannot be considered. For this initial conservative calculation, these limits are deemed sufficient. Further investigations could be carried out to investigate the material behavior in more detail. For example, the cut could be assumed to be a crack and calculated using fracture mechanics methods.

In the tensile stress calculation, the dead weight of the monopile and the resulting tension-reducing pressure on the cut surface was neglected. The calculation with the 80% hook load, which was used at Amrumbank, showed that the residual pressure stress is so low compared to the tensile stress caused by the wave forces that it makes sense to neglect it.

Validation of the stress calculation

In order to further validate the results and the assumptions made, the stress calculation was applied to the known case of the Amrumbank met mast. It was known that it broke between a cutting progress of about 98% to 98.6% due to hydrodynamic loading. The analytical calculation results in a critical cutting progress of 98.1% for the same input values, at which the tensile strength of the material is reached. The calculation can thus be validated in principle, but a few limitations must be considered. Firstly, the stresses calculated for the Amrumbank monopile in this range of 0.6% cutting progress fluctuate between 450 and 650 MPa, which represents a wide range. This means that the calculation at this point reacts very sensitively to the cutting progress. Secondly, it is not possible to find out exactly which load caused the met mast to fall. As described above, a maximum force was calculated for the sea state (for the Amrumbank met mast H_s was 1.5 m). It is not possible to judge whether it was really this force or another one that caused the mast to fail. However, it was seen by the time series that the model would also predict the failure in the range of 98% to 98.6% for lower forces that occurred (see Figure 4.2). This again is due to the high sensitivity to the cutting progress at this stage. Furthermore, any fatigue of the monopile was not taken into account. The Amrumbank met mast was exposed to the ocean for about 11 years, which could lead to a weakening of the material. For these reasons, it would be useful in future work to further validate the analytical stress calculation with other methods or real examples. Experiments with monopiles in water tanks could also be done to further investigate the behaviour during cutting. Even if not all factors could be taken into account, the calculated and real results still match fairly well for the simplified approach. An initial estimate of when a monopile will lose its stability and break due to cutting can therefore still be made.

Modal analysis

The modal analysis was additionally carried out to investigate the vibration behaviour of the pile as the cut progresses. Previously, the stability of the monopile was assessed solely on the basis of a static calculation of the maximum stress. If the pile starts to move strongly, this could also lead to failure. However, the results of the modal analysis show that the pile remains relatively stiff even with large cutting progressions. In comparison with the wave frequencies, the natural frequencies of the monopile are many times higher. The assumption that the monopile fails due to maximum force and not due to excessive motion can therefore be verified. In addition, the mode shape with the lowest frequency and therefore the one that is most likely to be excited shows that the shape hardly changes during cutting. The effective fixity model was also used for the modal analysis. In comparison with other, more complex soil models, this simplified model nevertheless shows good results. The real stiffness is likely to be even greater, as the effective fixity model slightly underestimates it [55]. The convergence study of the modal analysis showed good convergence against threshold values for the modal frequencies. It can therefore be assumed that the mesh is sufficiently fine and correctly generated.

Calculation of the extraction forces

The calculation of the extraction forces and the hook loads when pulling out the monopiles was also carried out. The calculation of the weights can be regarded as trivial. The shaft friction was calculated using standard API methods for sand and clay. These methods for calculating axial soil capacity are widely used in the industry and will therefore not be discussed in detail. It was assumed that the soil was not affected by previous cutting or any horizontal movement after the pile comes free. This made it possible to determine the maximum loads that the crane must be able to withstand. However, this should only serve as an estimate for the required maximum crane capacity.

Parameter variations

The influence of various parameters on the cutting and extraction calculations was studied. The largest influences on the cutting were found to be produced by the depth that the monopile top is below the water surface, the pile diameter, the water depth and the sea states. As expected, deeper water and larger sea states led to higher loads and therefore larger stresses in the cut line. However, the significant difference when varying the depth of the pile top is less intuitive. It was found that this is due to the fact that the hydrodynamic loads are largest directly below the water surface. This must be kept in mind when deciding if and where the transition piece on top is cut off. In chapter 5, this phenomenon will be investigated further because one of the wind farms in the case study has a bolted transition piece. If this is bolted and not cut off the monopile, the pile protrudes through the waterline and the loads in the top of the water column are applied. Another counter-intuitive observation is the reduction of the tensile stresses in the pile when the diameter increases. It is not intuitive because the forces increase with larger pile diameters. However, the cut surface that takes the loads also becomes larger and this increase is faster than the force increase. It is important to note that only one parameter at a time has been varied. In chapter 5, realistic parameter sets will be investigated.

Considering the influence of the varied parameters on the extraction, the largest influences were observed when analysing the soil type, the cutting depth, the monopile diameter and the water depth. Apart from changing the cutting depth, the monopile weight is the main contributor to the hook load. The weight is especially sensitive to the diameter and water depth as these change the pile dimensions the most. Modelling the friction forces exerted by the soil with the used API approach, clay is found to generally produce larger friction. As stated before, it is assumed that the water flow from the cutting process does not interfere with the soil above the cut line. Furthermore, other degradation of the soil is not considered to have a conservative estimate for the needed crane capacity. In reality, the pile might move after being fully cut which could lead to the soil losing some of its integrity and the soil friction being lower.

5

Analysis of case studies

In this chapter, the calculations already performed in chapter 4 are carried out for two case studies. In addition, the monopile decommissioning schedules for the case studies are established and analysed. The two real wind farms analysed are Robin Rigg and Galloper. Both are located in UK waters and differ significantly. In the following, both wind farms are first introduced, before the results of the described calculations are presented.

5.1. Description of Robin Rigg

The Robin Rigg Offshore Wind Farm (Robin Rigg) has a capacity of 174 MW and has been fully operational since April 2010 after the construction began in December 2007. The following subsections on site location, layout, bathymetry and soil, metocean conditions and installed foundations are based on RWE's documents [56].

5.1.1. Site location and layout

The wind farm is located on the Robin Rigg sandbank in the Solway Firth in Scottish waters. The site is approximately 13.5 km off the coast of Cumbria (England) and 9 km off the coast of Dumfries and Galloway (Scotland) [57].

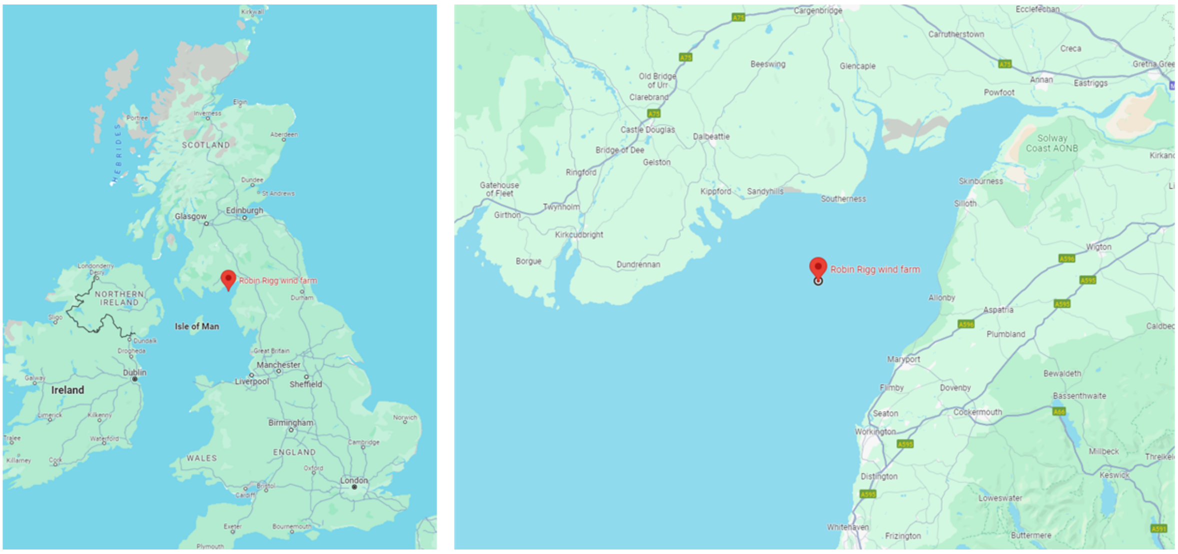

Figure 5.1: Location of the Robin Rigg Offshore Wind Farm.

Source: [57]

The OWF consists of 60 Vestas V90-3MW turbines spaced over a total area of 10 km^2. The distance in between the turbines is approximately 450 m. The site is split into Robin Rigg East (RRE) and Robin Rigg West (RRW), which each consist of 30 WTGs. RRE and RRW both have two array cable loops and an offshore substation which can be seen in Figure 5.2.

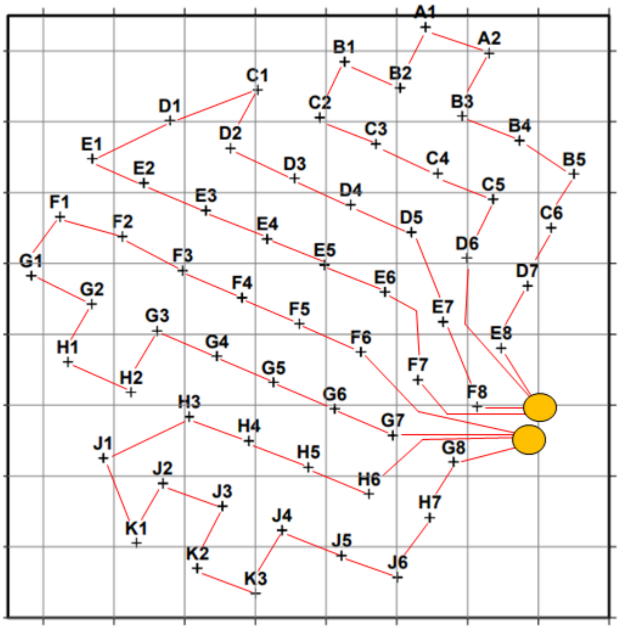

Figure 5.2: Turbine names with locations (black crosses), array cables (red lines) and substations (orange circles) of the Robin Rigg Offshore Wind Farm.

Source: [58]

The two array cable loops connected to the upper substation form RRE, the other two form RRW. The export cables are connected to the national electricity grid at Workington in England (see Figure 5.1). Together with both substations they are not owned and therefore likely to not be decommissioned by RWE. [56]

5.1.2. Bathymetry and soil conditions

Due to the proximity of Robin Rigg to the coast, the tidal effects can be felt relatively strongly. A reference value must therefore be defined that can be applied when specifying water depths, the so-called chart datum (CD). In the case of Robin Rigg, the chart datum is equal to the lowest astronomical tide (LAT), i.e. the lowest possible water level due to tides.

The dynamics of the Robin Rigg sandbank lead to changes in the morphology of the seabed and the water depths at this location. The last bathymetric survey was carried out in spring 2023 (see Figure 5.3). The area is divided into parts, with the deeper waters separated by a narrow bank with very shallow water depth. The upper channel covers almost the entire RRE and has an average depth of about 8 m LAT. The water depth increases from south-west to north-east. The upper channel also contains the largest natural water depth of the site, which is about 15 m LAT in the far north-east of RRE. The lower channel largely comprises the bottom loop of the two array cables of RRW, also with an average depth of approximately 8 m LAT. The shallow water bank runs from west to north-east through the centre of the wind farm and therefore also affects some of the turbines. The approximate average depth above the shallow water sand bank is 1.5 m LAT. The shallowest natural water depths are located directly south-east of WTG number E6 with values around 0 m LAT and even above, exposing the seabed during low tides. Locally at the turbines, the natural depths are exceeded due to scouring effects around the foundations. Only 21 of the monopiles are protected against scouring and most of the protection was installed later during operation in 2016 and 2018. Due to this, the original mudlines from 2008/09 at most turbines have dropped over the years of operation [56].

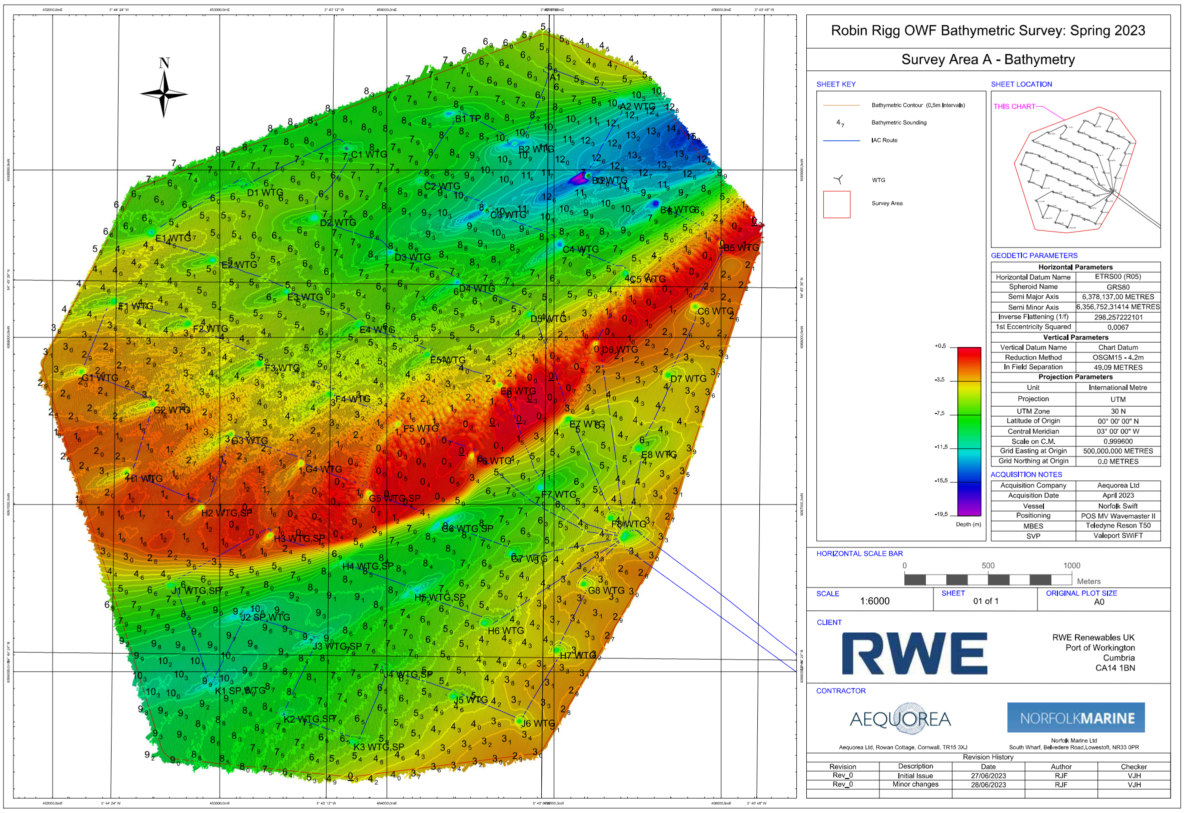

Figure 5.3: 2023 bathymetry of Robin Rigg Offshore Wind Farm.

Additionally to Figure 5.3, an overview of the water depths at all 60 turbine locations is provided in Table 5.1. The seabed depths including consideration of scour effects at the turbines are given. It is further indicated if scour protection (SP) has been installed.

Table 5.1: Water depths at turbine locations of Robin Rigg Offshore Wind Farm.

Location	Water depth	Location	Water depth	Location	Water depth	Location	Water depth
A1	6.3 m	D3	16 m	F3	10.8 m	H2 (SP)	8.4 m
A2 (SP)	14.4 m	D4	15 m	F4	12.4 m	H3 (SP)	10 m
B1 (SP)	14.4 m	D5	12.7 m	F5	8.1 m	H4 (SP)	12 m
B2 (SP)	11.4 m	D6	6.8 m	F6	7.8 m	H5 (SP)	10.8 m
B3 (SP)	8.9 m	D7	10.4 m	F7	13.8 m	H6	12.3 m
B4	19.5 m	E1	14.4 m	F8	11.3 m	H7	11.2 m
B5	6 m	E2	13.7 m	G1	10.5 m	J1 (SP)	11.1 m
C1 (SP)	12.1 m	E3	12.5 m	G2	10 m	J2 (SP)	11.3 m
C2 (SP)	12 m	E4	14 m	G3	9.9 m	J3 (SP)	11.3 m
C3 (SP)	9.8 m	E5	12.4 m	G4	10 m	J4 (SP)	9.8 m
C4	17.8 m	E6	7.7 m	G5 (SP)	6.9 m	J5	12.1 m
C5	11.4 m	E7	11.4 m	G6 (SP)	10.3 m	J6	10.4 m
C6	8.8 m	E8	11.3 m	G7	13.7 m	K1 (SP)	11.7 m
D1 (SP)	9.7 m	F1	13.3 m	G8	10.3 m	K2 (SP)	11.2 m
D2	15.3 m	F2	12.1 m	H1	11.2 m	K3 (SP)	11.4 m

Today, the average seabed depth with consideration of scour holes across all locations is 11.48 m LAT with the most extreme location being WTG B4 where the water depth is 19.5 m LAT.

The seabed of the OWF consists of sand, silt, clay and till deposits. However, since the wind farm is constructed on a sandbank the upper soil layers widely consist of sand which can be described as medium dense to very dense. These sand deposits are 17 - 21 m deep with few silt and clay deposits inter-bedded. Underneath these layers is glacial till [59]. Due to the sand layer reaching far beyond the potential cutting depths, only the sand needs to be considered as the soil. The buoyant weight of the sand γ_s' is estimated to be $10\,\mathrm{kN/m^3}$ and the sand friction coefficient β is 0.46 [51, 60].

5.1.3. Metocean conditions

The metoceanic conditions can be divided into wind, tides and waves and are considered separately below. The nominal wind climate is measured at 10 m above sea level with a spatial resolution of 0.2°. Long-term probabilistic data on the wind speed at Robin Rigg can be seen in the wind rose in Figure 5.4. This data covers the period from January 1979 to the present.

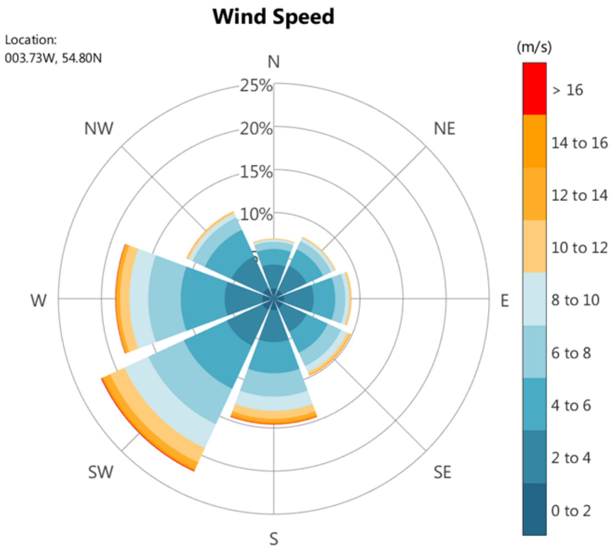

Figure 5.4: Long term probabilistic wind rose of Robin Rigg Offshore Wind Farm.

Source: [61]

The prevailing wind directions are west, south-west and south, with the wind from these directions accounting for around 55% of all winds. Furthermore, wind speeds of max 10 m/s account for 89% of all wind speeds.

Before describing the tidal effects at Robin Rigg, the most important tidal levels and their names are explained. In contrast to the previously used LAT, which corresponds to the absolute lowest possible tide, the highest astronomical tide (HAT) is the highest possible tide level. Two other important values are the tidal spring and neap ranges. Springs are the tides with the largest difference between high and low water and neaps are the tides with the smallest difference between high and low water. Taking the yearly averages of spring tides results in mean high water springs (MHWS) and mean low water springs (MLWS), taking the yearly averages of neap tides results in mean high water neaps (MHWN) and mean low water neaps (MLWN). From highest possible to lowest possible tides the order would therefore be HAT, MHWS, MHWN, MLWN, MLWS and LAT [62]. The values for the tidal levels at Workington Port, which is closest to the Robin Rigg, can be found in Table 5.2.

Table 5.2: Tidal levels at the port of Workington.

Tidal Levels	
HAT	9.27 m
MHWS	8.35 m
MHWN	6.52 m
MLWN	2.65 m
MLWS	0.93 m
LAT	0.04 m

Source: [63]

The resulting max possible tidal range between HAT and LAT is 9.23 m, the spring range is 7.42 m and the neap range is 3.87 m. For 2024 the highest tide will be 9.18 and the lowest will be 0.06 m [63]. Due to the tides, the OWF is exposed to significant currents everyday. However, the maximum tidal current velocities do not vary much, as the current velocity for a one-year return period is 1.29 m/s and that for a 50-year return period is only slightly larger at 1.32 m/s [56].

Similar to the wind speeds, there are also hindcast databases of wave parameters that date back to January of 1979. In Figure 5.5, long-term hourly averages of the significant wave height at Robin Rigg are given.

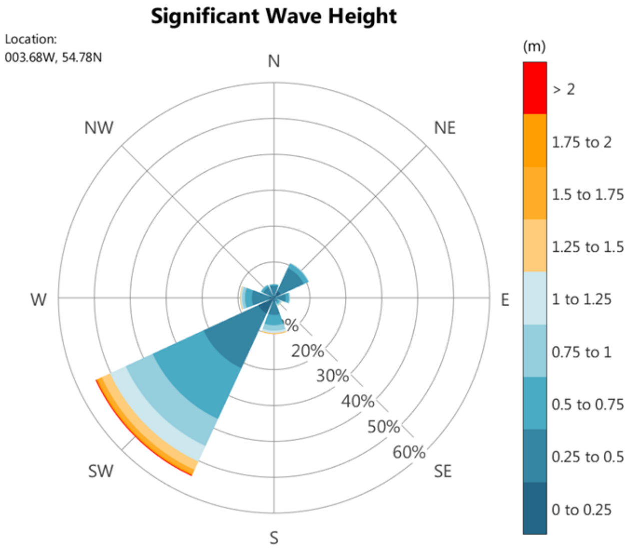

Figure 5.5: Long-term probabilistic wave rose of Robin Rigg Offshore Wind Farm.

Source: [61]

The largest amount of the waves comes from the south-west direction with a percentage of 65%. These are the waves entering the Solway Firth from the open sea. Due to the proximity to the coast, only around 15% of the waves exceed a significant wave height of 1 m, making the metocean conditions at Robin Rigg very mild compared to other locations.

5.1.4. Installed foundations

The Vestas V90-3 MW turbines are supported by monopiles with transition pieces used in between the turbine tower and the foundation. The transition pieces are the same at all WTG locations and serve as the connection between the turbine tower and the monopile foundation. The turbine tower is connected to the transition piece with 120 bolts. The monopile and the transition piece are grouted together. The grout annulus in the 6.45 m overlap zone between transition piece and monopile is 70 mm thick, resulting in a total weight 15 t of grout used per foundation [56]. Due to the grouted connection, the transition piece needs to be cut off the monopile. This cut is assumed to be around 1 m below the bottom of the transition piece, thus 7.45 m below the monopile top. This is the reason why the monopile top lies below the waterline.

The monopiles were installed between 2007 and 2009 using the heavy lift jack-up vessel MPI Resolution. They are each uniquely adapted to their location. Due to different soil profiles, the length of the piles varies from 35.45 m to 42.45 m. The outer diameter is kept constant everywhere at 4.3 m. However, the wall thickness varies between 45 mm and 75 mm which also changes the inner diameter along the foundation. The total weight of the monopiles is 228 t on average [58]. For the calculations, only one monopile is considered. Location B4 is chosen, since the water depth is the largest. The wall thickness at the potential cut line 3 m below seabed (with scour hole) is 55 mm. This and the largest water depth makes location B4 the most critical among all monopile foundations at Robin Rigg.

Over the years of operation, exposure to the sea will lead to an accumulation of marine growth on the monopiles and transition pieces. These biological organisms further increase the weight as they grow on the piles. For the parameter variations, a constant value for the marine growth thickness of 80 mm was assumed. For this case study more detailed assumptions are available. The thicknesses on the outside of the foundations can be seen in Table 5.3. The density is assumed to be 1400 kg/m^3.

Table 5.3: Marine growth.

Depth (reference: LAT)	**Marine Growth Thickness**
8.75 m to -1.25 m	50 mm
-1,25 m to -11.25 m	45 mm
-11,25 m to -16.25 m	65 mm
-16.25 m to -26.25 m	90 mm
<-26.25 m	80 mm

Source: [56]

To find the range of added weight due to marine growth, it is exemplary calculated for the locations B4 and B5 which are the deepest and the shallowest. The calculated weights are 7 t for B5 and 16.1 t for B4.

In section B.1 in the appendix, a tabular overview of all parameters used in the Robin Rigg case study is provided.

5.2. Description of Galloper

This section presents RWE's Galloper Offshore Wind Farm (Galloper) which is used as the second case study in this thesis. Galloper has a capacity of 353 MW and became fully operational in April 2018 after construction began in 2015 [64]. The following subsections explain the location and layout of the site, the bathymetry and soil conditions and the installed foundations. The available information on Galloper are not as detailed as they are for Robin Rigg. Therefore, some things are taken over from Robin Rigg. However, this will be explicitly mentioned.

5.2.1. Site location and layout

Galloper is located in the outer Thames estuary in UK waters. The distance to the Suffolk coast in the East of England is approximately 27 km and the closest port is Harwich [65]. Compared to Robin Rigg, Galloper is located more in the open sea and is therefore less protected. Figure 5.6 shows the wind farm's location on Google Maps.

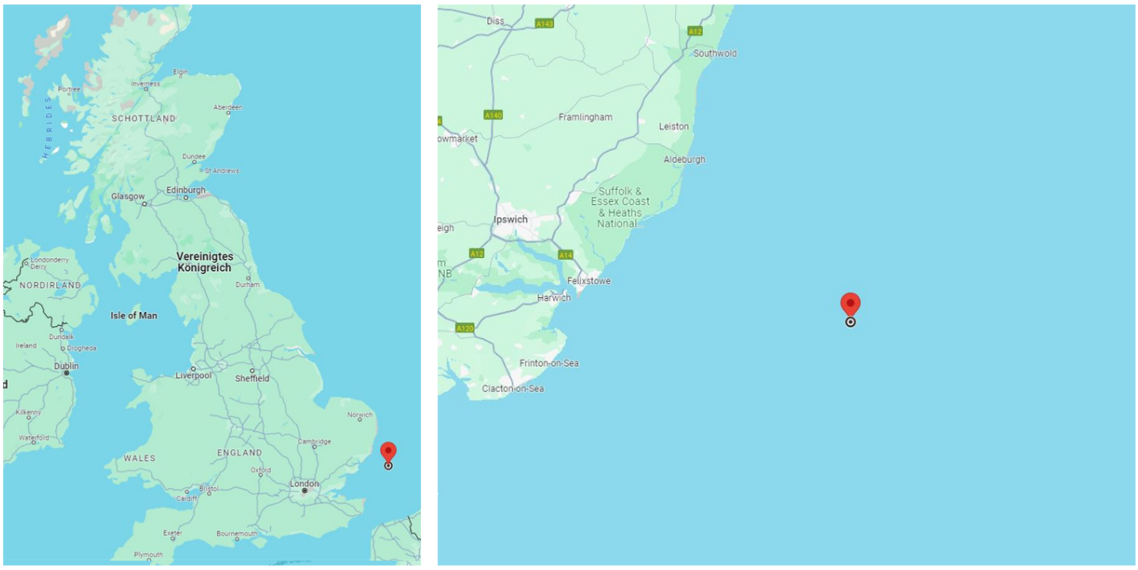

Figure 5.6: Location of the Galloper Offshore Wind Farm.

Source: [65]

The site consists of 56 Siemens D6-6.3MW turbines spaced over a total area of 114km^2. Similar to Robin Rigg, Galloper is also split into two sites, the Galloper North and the Galloper South Area. In the Northern area, 38 of the turbines and in the Southern area the remaining 18 are located. The turbine layout and the array cables connecting all turbines to one offshore substation can be seen in Figure 5.7.

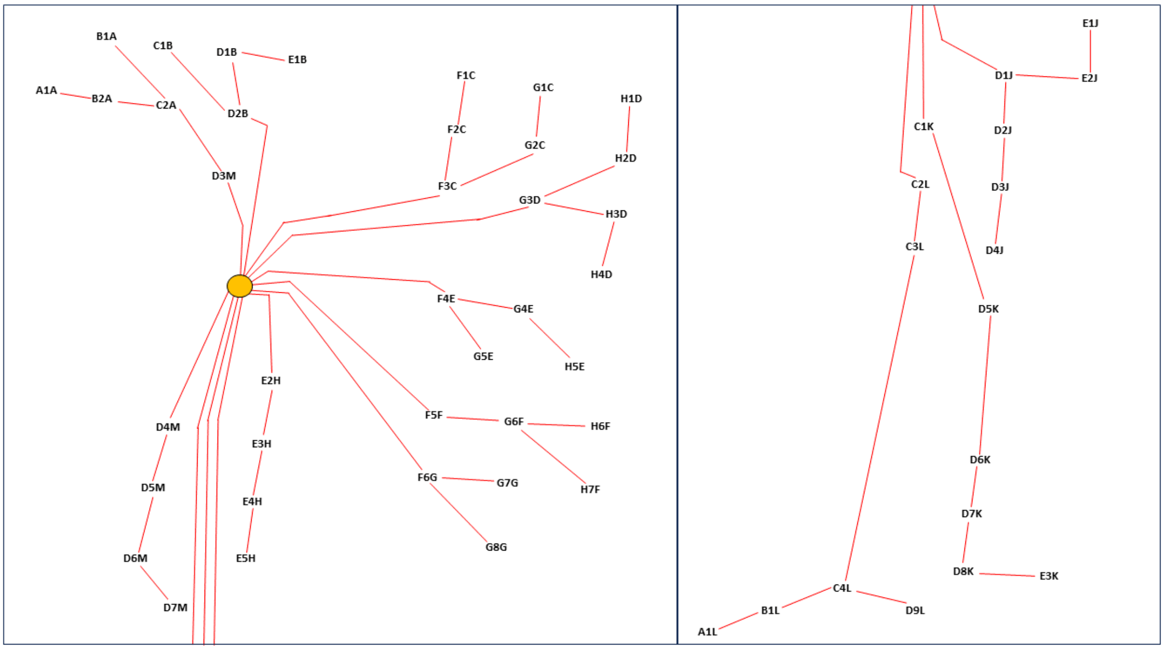

Figure 5.7: Turbine names with locations, array cables (red lines) and substations (orange circles) of Galloper North (left) and South (right).

Each array cable connects a maximum of six turbines. Nine of these cable strings link the turbines of the Galloper North area to the substation. The turbines of Galloper South are linked by three cable strings. The offshore substation is connected to the national electricity grid in Suffolk and is not to be decommissioned by RWE. [64]

5.2.2. Bathymetry and soil conditions

In contrast to Robin Rigg, no recent bathymetric survey was conducted. However, Spinergie also provides the water depths and since the monopile foundations are protected against scouring, these water depths are assumed to be reasonably accurate. The water depth for every turbine can be seen in Table 5.4. The average water depth is 31.2 m LAT and the turbine with the largest water depth of 35 m LAT is WTG B1L.

Table 5.4: Water depths at turbine locations of Galloper Offshore Wind Farm.

Location	Water depth	Location	Water depth	Location	Water depth	Location	Water depth
A1A	31 m	D2J	33 m	E1J	34 m	G2C	30 m
A1L	33 m	D3J	33 m	E2H	28 m	G3D	32 m
B1A	32 m	D3M	32 m	E2J	35 m	G4E	35 m
B1L	35 m	D4J	34 m	E3H	33 m	G5E	32 m
B2A	31 m	D4M	32 m	E3K	32 m	G6F	31 m
C1B	30 m	D5K	35 m	E4H	31 m	G7G	31 m
C1K	28 m	D5M	31 m	E5H	31 m	G8G	33 m
C2A	29 m	D6K	35 m	F1C	30 m	H1D	32 m
C2L	29 m	D6M	30 m	F2C	28 m	H2D	31 m
C3L	30 m	D7K	33 m	F3C	32 m	H3D	32 m
C4L	35 m	D7M	31 m	F4E	34 m	H4D	35 m
D1B	28 m	D8K	33 m	F5F	28 m	H5E	33 m
D1J	34 m	D9L	33 m	F6G	28 m	H6F	33 m
D2B	30 m	E1B	29 m	G1C	31 m	H7F	34 m

Source: [66]

The seabed at Galloper comprises predominantly London clay with few very thin sand deposits in some areas. For this type of stiff clay, a buoyant unit weight gamma γ_c' of 12 kN/m^3 and an undrained shear strength s_u of 50 kPa are assumed [60, 67].

5.2.3. Metocean conditions

Now, the metoceanic climate at Galloper, which is split into wind, tidal and wave conditions again, is analysed. The wind speed is measured at 10 m above sea level with a spatial resolution of 0.2°. Long-term probabilistic data on the wind speed at Galloper recorded from January 1979 until today can be seen in the wind rose in Figure 5.8.

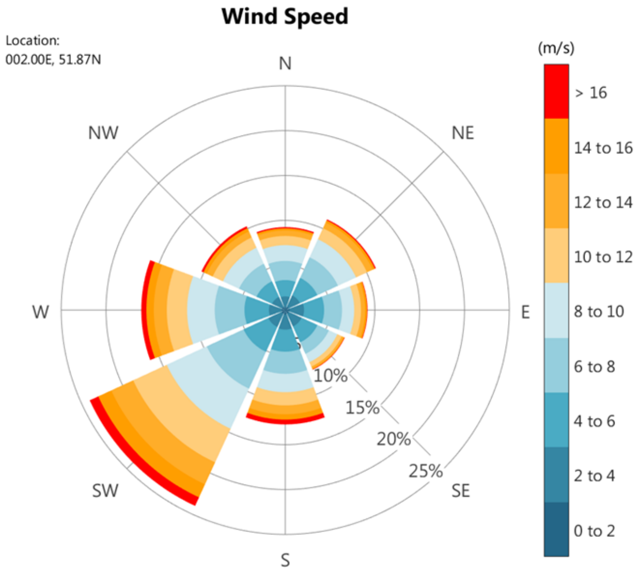

Figure 5.8: Long term probabilistic wind rose of Galloper Offshore Wind Farm.

Source: [61]

The prevailing wind directions are west, south-west and south with the wind from these directions making up for more than 52% of all winds. The wind speeds increase 10 m/s around 70% of the time which makes the location significantly more windy compared to Robin Rigg. However, wind speeds faster than 16 m/s only occur 3% of the time.

Galloper is further out in the open sea than Robin Rigg. Therefore, taking the tidal levels from the operation port Harwich is not as accurate than it was with Robin Rigg and Workington Port. Nevertheless, the tidal levels are presented in Table 5.5 below.

Table 5.5: Tidal levels at the port of Harwich.

Tidal Levels	
HAT	4.60 m
MHWS	4.15 m
MHWN	3.34 m
MLWN	1.12 m
MLWS	0.45 m
LAT	-0.11 m

Source: [68]

The tidal range at Harwich and thus at Galloper is significantly smaller in comparison with Robin Rigg. The resulting max possible tidal range between HAT and LAT is 4.49 m, the spring range is 3.7 m and the neap range is 2.22 m. For 2024, the highest tide will be 4.51 m and the lowest will be -0.1 m [68]. The maximum depth-averaged current speeds at Galloper are around 1.5 m/s [64].

The wave climate, similarly to the wind climate, is much more severe at Galloper than it is at Robin Rigg. At Robin Rigg, only 15% of the waves had a significant wave height larger than 1 m. For Galloper, this share is at around 50%. Also, wave heights larger than 2 m are relatively frequent with a share of around 11%.

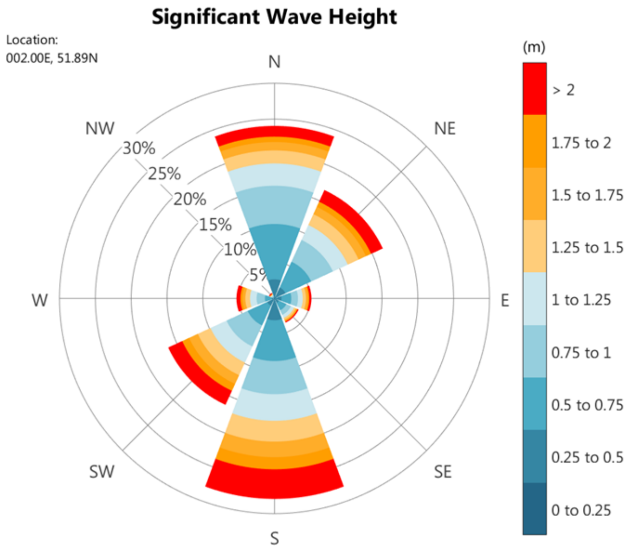

Figure 5.9: Long-term probabilistic wave rose of Galloper Offshore Wind Farm.

Source: [61]

5.2.4. Installed foundations

The Siemens D6-6.3 MW turbines are supported by monopiles with transition pieces used in between the tower and the foundation. In contrast to Robin Rigg, not only the tower-transition piece connection but also the monopile-transition piece connection is bolted. Due to this, the transition piece does not need to be cut off the foundation and can be unbolted. The bolted connection between the monopile and transition piece is at 6 m LAT which is above MSL and even above HAT. The monopiles were installed between December 2016 and April 2017 using the heavy lift jack-up vessel Innovation. They are each uniquely adapted to their location. Due to different soil profiles, the length of the piles varies from 85 m to 95 m. The outer diameter is 7.5 m and the wall thickness around the potential cutting line below seabed is 115 mm. The total weight of the monopiles is 1200 t on average which also is considerably heavier than the ones from Robin Rigg. Again, only the most critical monopile shall be considered. The foundation in location B1L is chosen as the water depth is the largest.

Since no information on the marine growth assumptions are available, the same values as for Robin Rigg are applied (see Table 5.3). To find the range of added weight due to marine growth at Galloper, it is calculated for the locations B1L and C1K which are the deepest and the shallowest. The calculated weights are around 36 t for C1K and 45 t for B1L.

As for Robin Rigg, in section B.1 in the appendix a tabular overview of all parameters used in the Galloper case study is provided.

5.3. Application of the cutting and extraction calculations

In this section, the results of the cutting and extraction model are presented for the two wind farms Robin Rigg and Galloper. This way, realistic parameter sets are analysed, in contrast to the previous parameter variations, where only one parameter at a time was varied. To avoid having to apply the model to all 60 piles from Robin Rigg and 56 piles from Galloper, only the monopile that is considered to be the most critical is calculated in each case. This can be determined with the help of the parameter variations carried out. Most of the parameters, such as the current velocity or diameter, are constant across the wind farm. However, as the water depth varies from location to location, the most critical pile is taken to be the one placed at the greatest water depth. It is also important how far the pile head is below the water level. Robin Rigg therefore considers both LAT and HAT. With Galloper, the monopile top is always above the water surface anyway, as the transition piece can be unbolted and does not have to be cut off. Therefore, only the case with the greatest water depth, i.e. HAT, is considered for Galloper.

5.3.1. Robin Rigg

For Robin Rigg, the tensile and shear stresses in the uncut sections were calculated for different sea states and different cutting progresses. This way the operational weather limits of the pile failing at a progress of 98% or before can be determined. In Figure 5.10 on the left, the variation of both stress types for different sea states and on the right, the variation with cutting progress can be seen. As before, the sea states are characterized by the significant wave height and the corresponding peak period. On top, a constant current velocity of 1.3 m/s is applied. As stated before, for Robin Rigg LAT and HAT conditions are considered. In Figure 5.10, first the LAT is analysed as the water level.

The most important observation is that none of the considered sea states leads to the ultimate tensile strength of the material being reached before 98%. With increasing wave height and period an increase in stresses can be seen but even for the most severe sea state considered, the tensile stress at 98% cutting progress is around 370 MPa. However, the ultimate tensile stress is reached only shortly after that at 98.4%. This again shows the large variation of the stresses in the final part of the cutting process. The shear stresses are considerably lower than the tensile stresses with around 33 MPa at 98% cutting progress. Due to these observations and the previously determined cutting limit of 98% that should be reached prior to failure, all considered sea states can be allowed at LAT.

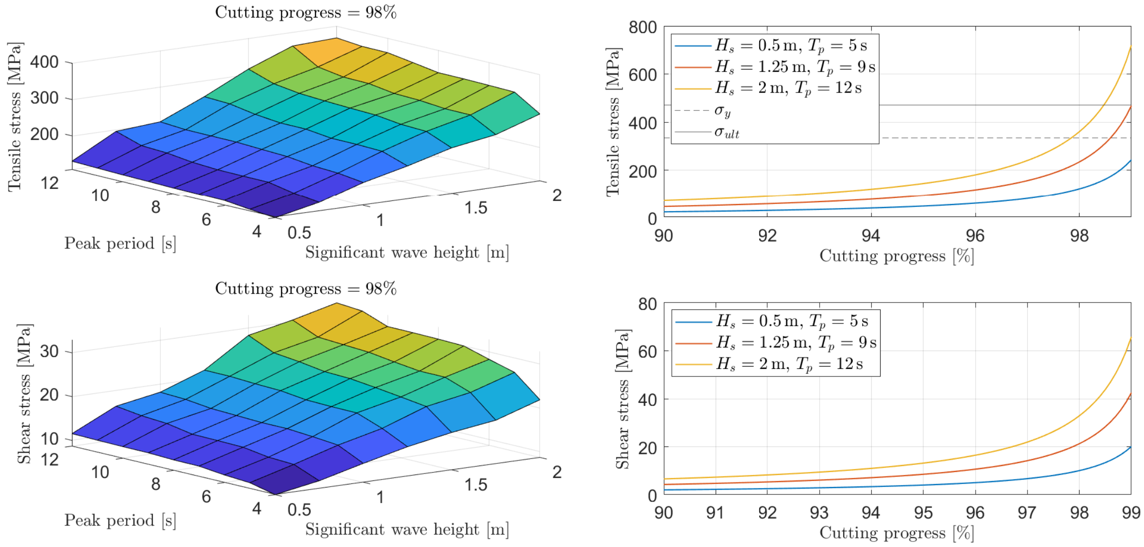

Figure 5.10: Stress calculation results for different sea states at LAT conditions for Robin Rigg.

Figure 5.11 shows the same results as before, now under HAT. It can be seen that the stresses in this case are even lower. At 98% cutting progress, the max tensile stress is 220 MPa and the max shear stress is 22 MPa. This can be explained with the depth the monopile top is below the water surface. As seen in section 4.2, when the top is further below the waterline the hydrodynamic loads are significantly reduced because the largest loading is exerted by the top wart of the water column. At LAT, the monopile top lies 3.14 m below the water line, at HAT this value increases to 12.37 m, resulting in significantly lower forces. Therefore, regardless of the tidal conditions the cutting can be carried out during all considered sea states.

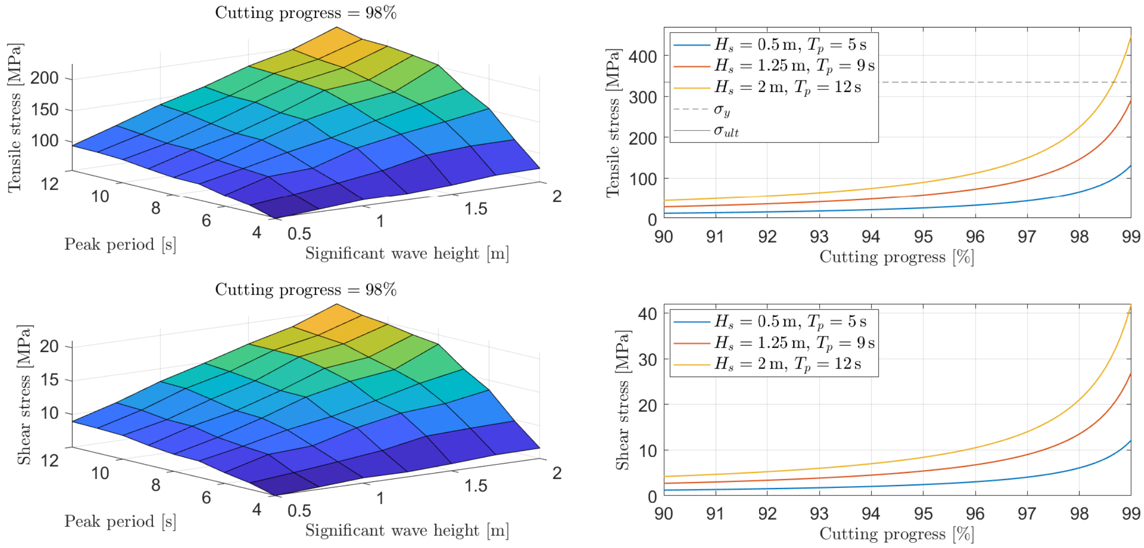

Figure 5.11: Stress calculation results for different sea states at HAT conditions for Robin Rigg.

For the Robin Rigg monopile, the modal analysis is also carried out. In Figure 5.12 the trends of the modal frequencies for the first two mode shapes (see Figure 4.3) are presented.

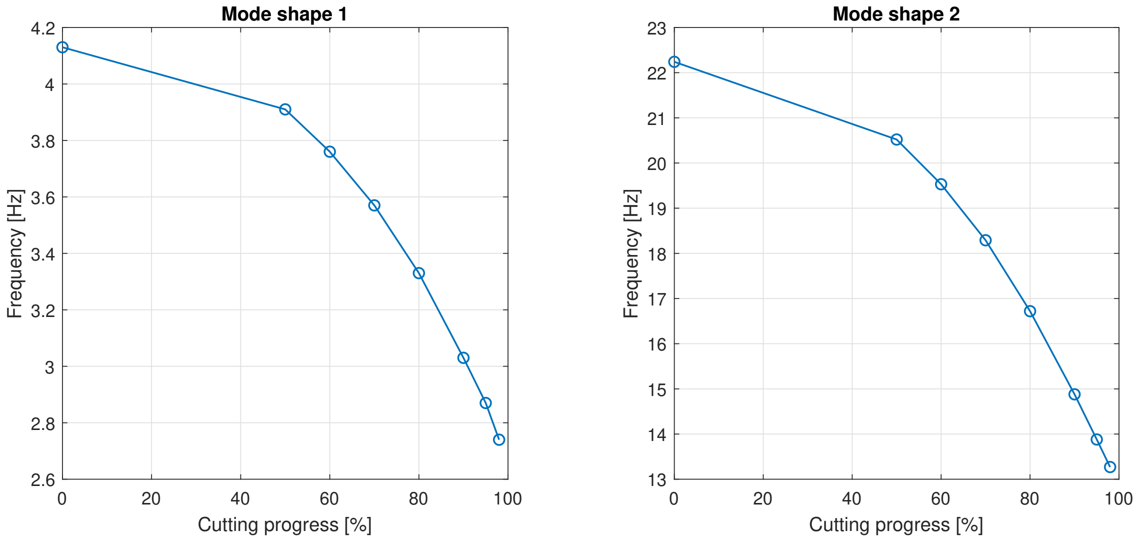

Figure 5.12: Modal frequencies of the Robin Rigg monopile.

Similarly to the Amrumbank met mast monopile, the frequencies decline when the pile is cut. The frequency of the first mode shape is 4.13 Hz when the pile is uncut and reduces to around 2.74 Hz when the pile is cut to 98%. For the second mode shape, the associated frequency is 22.24 Hz for an uncut monopile and decreases to 13.27 Hz at 98% cutting progress. The decrease indicates that the stiffness of the monopile is being reduced during cutting. However, the modal frequencies are larger than they were for the Amrumbank pile. This can be explained by the shorter but wider monopile used at Robin Rigg, which makes the structure stiffer. Due to the even larger frequencies, the monopile is even further away from the wave frequencies, with the frequencies being at least 10 times larger. In section C.3 in the appendix, a mesh convergence study, which shows the convergence of the results, can be found again.

As described in section 5.1, Robin Rigg is located on a sandbank with medium to very dense sand. As seen before, sand provides less friction than clay and since also the monopiles are relatively small, the total hook load is small. In Figure 5.13, the hook load and the contributions of the monopile weight and the soil friction are presented.

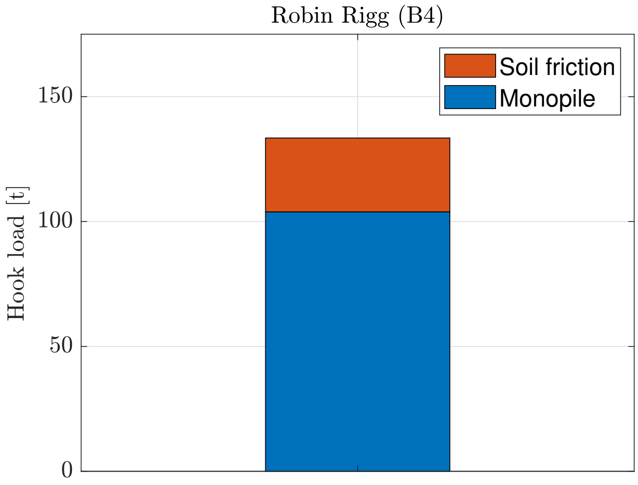

Figure 5.13: Hook load calculation results for Robin Rigg.

The hook load due to the pile weight is around 100 t and the soil friction makes up around 30 t. The maximum hook load therefore is 130 t which is around 100 t less than the total average weight of the monopiles used at Robin Rigg. The calculated loads during extraction can be taken by most heavy-lift jack up vessels. For example, even the first purpose-built wind turbine installation vessel (WTIV), the MPI Resolution that was also used for the Amrumbank met mast decommissioning, already has a crane capacity of 600 t.

5.3.2. Galloper

The same calculations are now carried out for Galloper, which has some differences compared to Robin Rigg (for details, see section 5.2). Most importantly, the monopiles are significantly larger and the piles protrude through the water line because the transition piece does not need to be cut off. Furthermore, the soil is different, as at Galloper predominantly stiff London clay can be found. Figure 5.14 again presents the variation of tensile and shear stresses with the sea states and cutting progress, respectively.

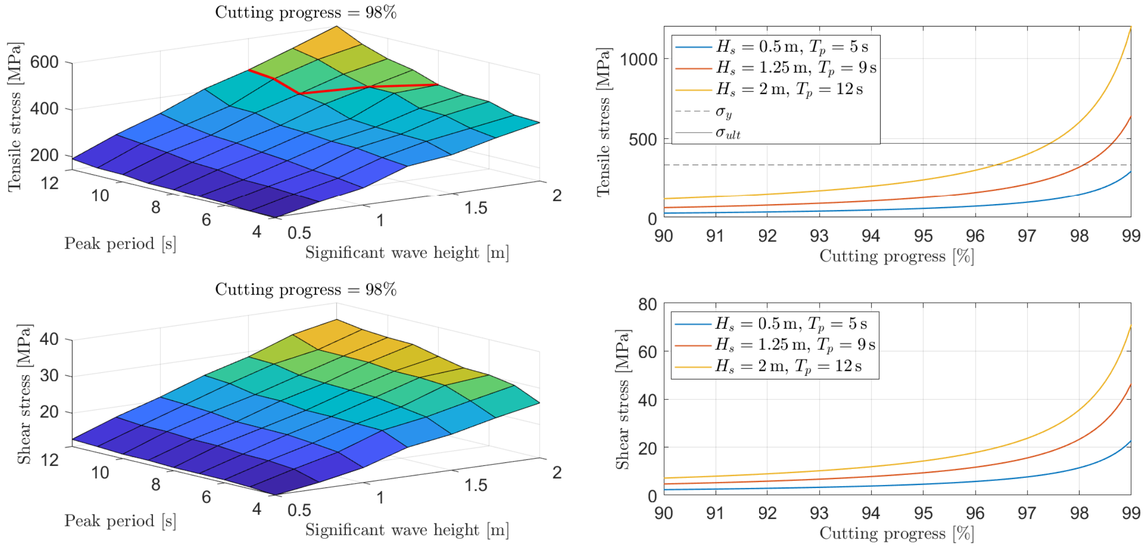

Figure 5.14: Stress calculation results for different sea states for Galloper.

It can be observed that for Galloper the sea state with $H_s = 2$ m and $T_p = 12$ s gives a stress of more than 600 MPa at 98% cutting progress. This significantly exceeds the ultimate tensile strength of the material. Based on the established limit that the tensile stresses in the cut should not reach this limit before 98% progress, this sea state cannot be allowed. The same observation can be made for some less severe sea states. The red line in the upper left graph shows the limit from which the sea states above it are not permitted due to the 98% limit. All sea states with a wave height of 1.5 m do not reach the ultimate tensile strength and therefore this can be used as a new wave limit for Galloper. The shear stresses still only play a subordinate role.

Again, the modal analysis is carried out for the monopile of Galloper, to see how the eigenfrequencies change with the progression of the cut. Figure 5.15 shows the curves of the two lowest eigenfrequencies.

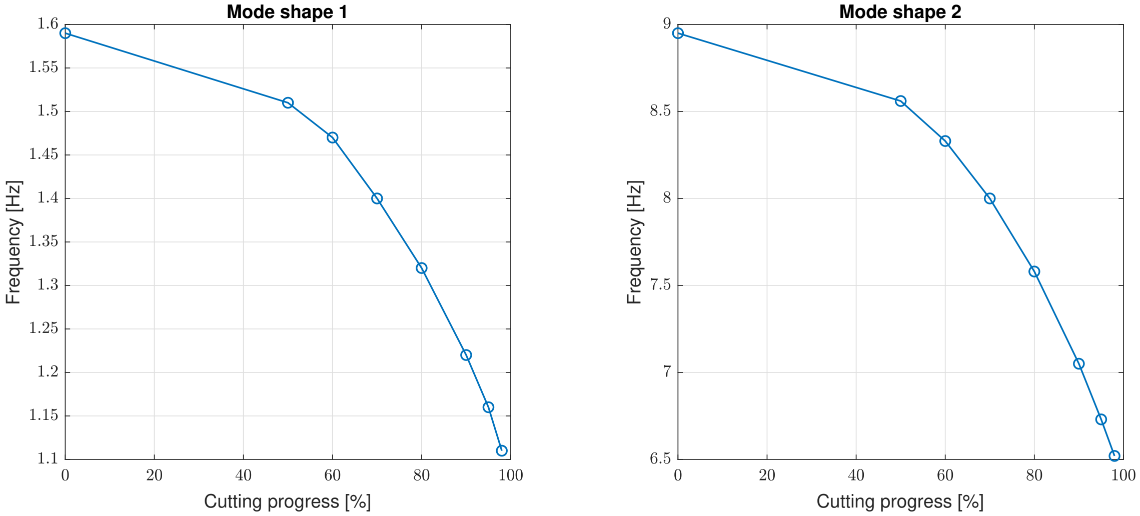

Figure 5.15: Modal frequencies of the Galloper monopile.

The eigenfrequencies again decline with progressing cut. For the first mode shape, the frequency of the uncut pile is 1.59 Hz and drops to 1.11 Hz at 98% cutting progress. In the same range, the frequency of the second mode shape declines from 8.95 Hz to 6.52 Hz. In general, the frequencies are at a lower level than in the two previously considered modal analyses. This is due to the significantly longer monopile at Galloper, which is less stiff overall. Nevertheless, the natural frequencies are still more than four times greater than the wave frequencies, even at a cutting progress of 98%. A mesh convergence study was carried out again. Convergence can also be observed in this last case; the exact results can be found in section C.3 in the appendix.

Like the stresses during cutting, at Galloper also significantly larger monopile extraction hook loads can be observed. These are due to the larger monopile weight and the stronger soil friction of the clay. Figure 5.16 presents the total hook load and the contributions of the pile weight and the soil friction.

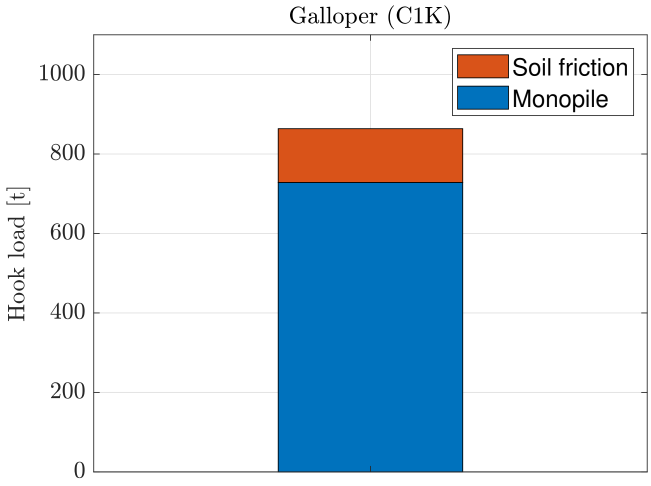

Figure 5.16: Hook load calculation results for Galloper.

The monopile weight yields a hook load of around 725 t and the soil friction adds another 135 t. This adds up to a total maximum hook load of 860 t which is more than 6 times larger than the required capacity for Robin Rigg.

5.4. Monopile decommissioning schedules

This section will be the last part of the thesis where new results are presented. The results are the decommissioning schedules for both case studies. These consist of the total duration of the operations, the shares of weather downtime on the total duration and an overview of the tasks that contribute the most to the weather downtime. Before the results for the schedules are given, first all the tasks that are carried out during the monopile decommissioning must be described:

The operation begins in the working port of the wind farm. For Robin Rigg this is Belfast and for Galloper it is Harwich. The vessel then starts with jacking-down, leaving the harbour and travelling to the respective location. The distance between the port of Belfast and Robin Rigg is approximately 84 nm and between the port of Harwich and Galloper it is 35 nm. After arrival, DP tests must be carried out on site. The vessel can then be jacked-up at the first turbine. After jacking-up, the equipment is prepared and the marker buoy is recovered. After these initial preparations, the main work can begin. Firstly, the dredging tool is inserted into the monopile and it is dredged to a certain depth. Once the dredging tool has been recovered, the water cutter can be inserted into the pile. Before starting the circumferential cut, the tool is positioned and three small vertical cuts are made to ensure that the connection between the three cutting lines is established. Then the main cutting process begins. Once the cutting process is complete, the monopile and the tool are recovered to the vessel together. On board, the monopile is down-ended, the tool is retrieved and the pile is fastened at sea. Once this work has been completed, the vessel can jack-down and travel to the next location, where it will start with jacking-up again. It is assumed that four monopiles can be transported at the same time. Once the fourth monopile has been fastened at sea, the vessel returns to the working port, jacks-up and unloads the recovered monopiles. The cycle described above then begins again.

In the previous description of the monopile decommissioning, a jack-up vessel was always assumed. This is due to the fact that a jack-up vessel was also used during the Amrumbank met mast removal campaign. Such a vessel will also have to be used at Robin Rigg, as some of the turbine locations are in such shallow waters that floating vessels would run aground at low tide. For the comparison of the two wind farms, it is therefore assumed that a jack-up vessel will also be used at Galloper. Furthermore, it is always taken for granted that only the monopiles need to be removed. Turbines and transition pieces as well as any other structures are not considered. This is discussed in section 5.5. In principle, the decommissioning campaigns for Robin Rigg and Galloper are very similar. The biggest differences can be found in the aforementioned port distance, the tool deployments, the cutting itself and the number of trips. The limits for deploying the tools are much lower for Robin Rigg, as they have to be guided into the pile underwater with an ROV. At Galloper, this can be done above the water surface leading to higher limits. Cutting takes longer at Galloper due to the larger diameter; instead of 7.3 h as with Robin Rigg, it takes 12.7 h. Robin Rigg requires 15 trips to decommission all the piles, whereas Galloper only requires 14.

In section B.2 in the appendix, overview tables with the individual tasks, their duration and the weather limits are provided. The duration and limits were only calculated for cutting. The effort required to carry out these calculations for all other tasks would be massive. Furthermore, as the other tasks are not new, compared to monopile cutting, and are frequently performed (e.g. jacking operations), the limits and duration of these tasks are only estimated. Therefore, other schedules of marine operations calculated with WDTX are used as references. As already described in section 3.5, WDTX usually only sets a limit for the wave height, but not for the wave period. This way all waves of the specified height are forbidden, independent of the period. Furthermore, the application of alpha factors to the operational limits is not necessary because no uncertainties in the weather forecast are included. WDTX uses hindcast data and can therefore predict how the operation will perform statistically. Nevertheless, the tables with calculated alpha factors can also be found in section B.2 in the appendix. These are important if the operation is carried out in reality and the weather forecast has to be used on the vessel. In addition to the limits and duration, the tables in the appendix also contain values for the average period of the wind and the reference height at which the wind limit should apply. The default value of 600 s is retained for the period. The reference height for the wind is important as the wind speed increases with increasing height. A reference height of 50 m is therefore specified for crane operations. In all other cases without a crane operation, this is set to 10 m.

5.4.1. Robin Rigg

First, the total duration of the monopile decommissioning of Robin Rigg and the associated weather downtime is analysed. Figure 5.17 presents graphs for the total duration and the weather downtime, both in days, depending on the probability of non-exceedance and the starting date throughout the year. Three probabilities are given: P50, P75 and P90.

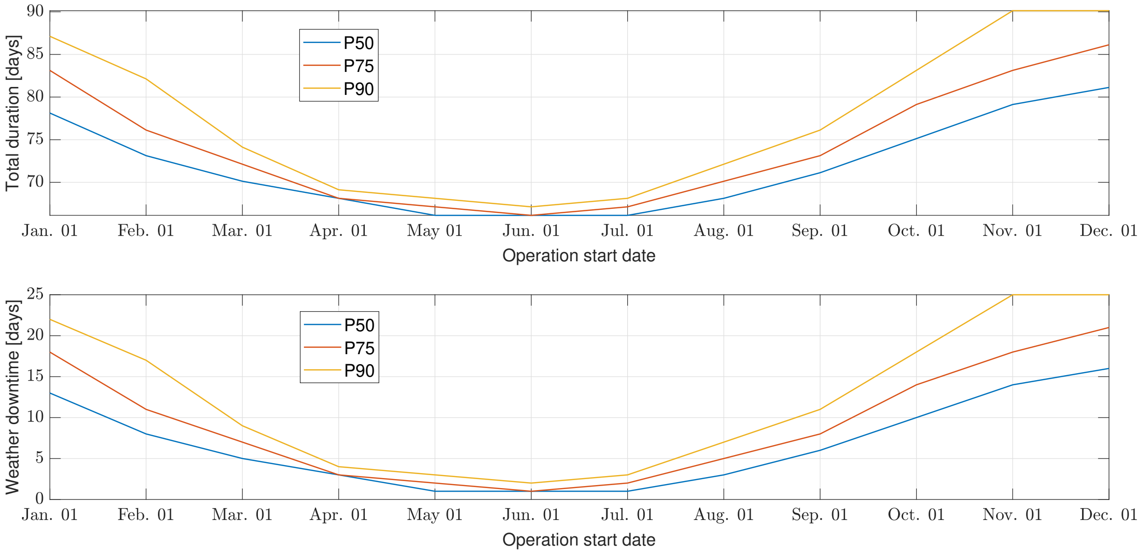

Figure 5.17: Total duration and weather downtime for the monopile decommissioning at Robin Rigg.

The general trend can easily be observed: If the starting date for the operation is during summer, the weather downtime and thus the total duration of the operation is reduced significantly. For the P50 case, the weather downtime drops from 16 days in December to only 1 day when starting in May, June or July. This has to be added to the net duration of around 65 days to find the total duration. The net duration is the working time without any limitation due to weather. Increasing the probability of non-exceedance also increases the weather downtime. For P75, the maximum weather downtime is 21 days and the minimum stays 1 day. For P90, the maximum weather downtime is 25 days and the minimum goes up to 2 days. December and November as starting months for the operation give most downtime and June the least amount. In Figure 5.18, this is further analysed and pie charts are presented for the yearly average, the best month and the worst month, considering operability. This is based on the P50 probability of non-exceedance. The yearly average weather downtime is 9% which can be further reduced to only 2% in May. Starting the operations in December would yield a weather downtime of 18%.

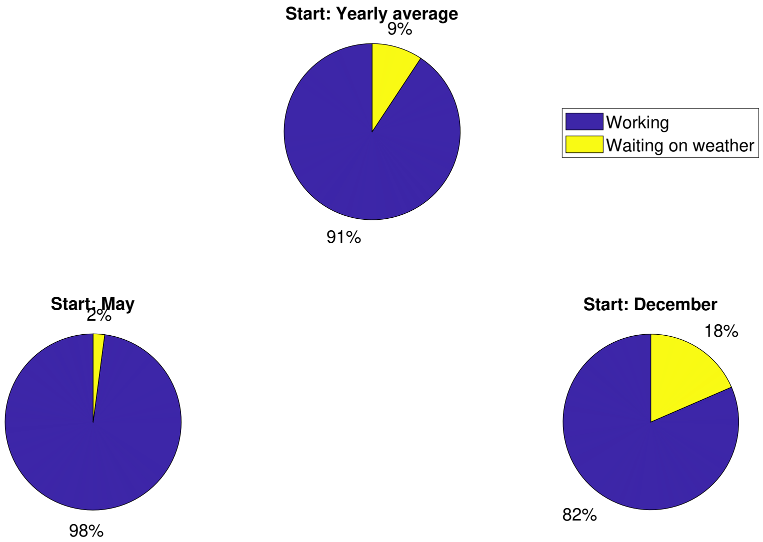

Figure 5.18: Share of weather downtime at Robin Rigg.

In addition, the contributions to the weather downtime are analysed in Figure 5.18. The pie chart presents the shares of the tasks contributing to most weather downtime.

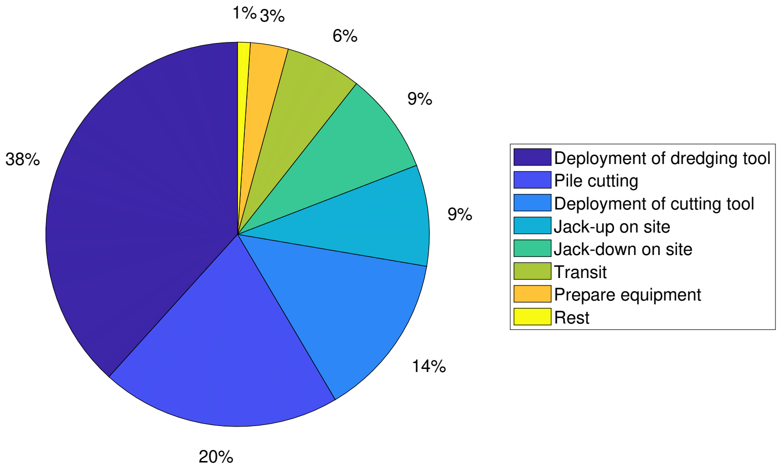

Figure 5.19: Top tasks contributing to weather downtime at Robin Rigg.

It can be seen that the deployment of the dredging and cutting tools makes up for 52% of all weather downtime. In Table B.3 it was shown that these tasks have the lowest wave and current limits because ROVs must be used to correctly guide the tools through the water column. Even though both tasks have exactly the same limits, the deployment of the dredging tool makes up for 24% more weather downtime. This can be explained by the sequential modelling approach. When the deployment of the dredging tool has to be undertaken the limits drop significantly the first time and some waiting on weather can be expected. The deployment of the cutting tool then happens shortly after. Here, only weather downtime will occur if the weather in between the deployment of the dredging and the cutting tool got worse again. Other tasks contributing considerably to weather downtime are the pile cutting with 20% respectively and the jacking operations on site with a total of 18%. Generally, these results show very good operability which is mainly due to the mild sea climate at Robin Rigg. Figure 5.5

showed how rarely the wave heights of 1 m are exceeded. Further discussions regarding these results can be found in section 5.5.

5.4.2. Galloper

In this subsection, the total duration of the monopile decommissioning at Galloper and the associated weather downtime is analysed. Again, Figure 5.20 presents graphs for the total duration and the weather downtime, depending on the probability of non-exceedance and the starting date throughout the year.

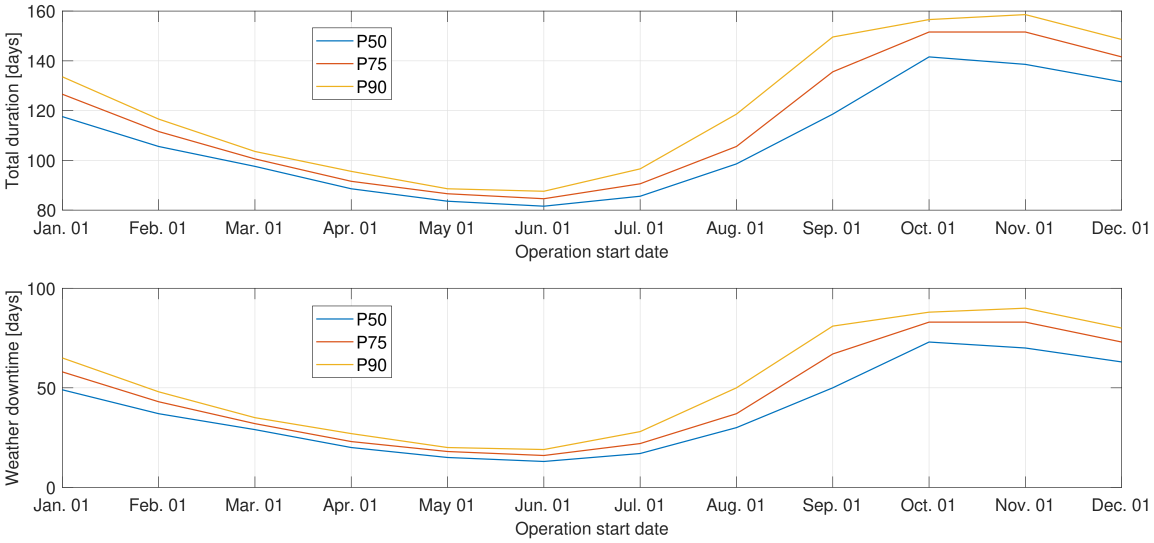

Figure 5.20: Total duration and weather downtime for the monopile decommissioning at Galloper.

The overall trend that weather downtime is largest during the winter months and smallest during summer also holds at Galloper. The net duration of the operation is 69 days, thus four days more than it is for Robin Rigg even though four piles less have to be removed. This can be explained with the longer cutting duration for each pile at Galloper. Regarding the weather downtime for the P50 case, this drops from 73 days for operations starting in October to 13 days when starting in May. An increase in probability of non-exceedance again increases the weather downtime. For P75, the weather downtime in October increases to 83 days. The downtime for operations starting in June increases to 16 days. For the P90 case, these values increase to 88 days in October and 19 days in June. Adding the weather downtime to the net duration leads to the total duration of the operation. When comparing this with the found total duration of Robin Rigg, it can be seen that the decommissioning operation takes longer at Galloper. This effect is especially significant in the winter months. For the P50 case, the maximum total duration of the operation is more than 50 days longer for Galloper. Since the net duration of both decommissioning schedules are very similar this has to be due to the more severe weather conditions occurring on the Galloper site (see Figure 5.5 and Figure 5.9). The pie charts in Figure 5.21 present the percentage of weather downtime on the total duration.

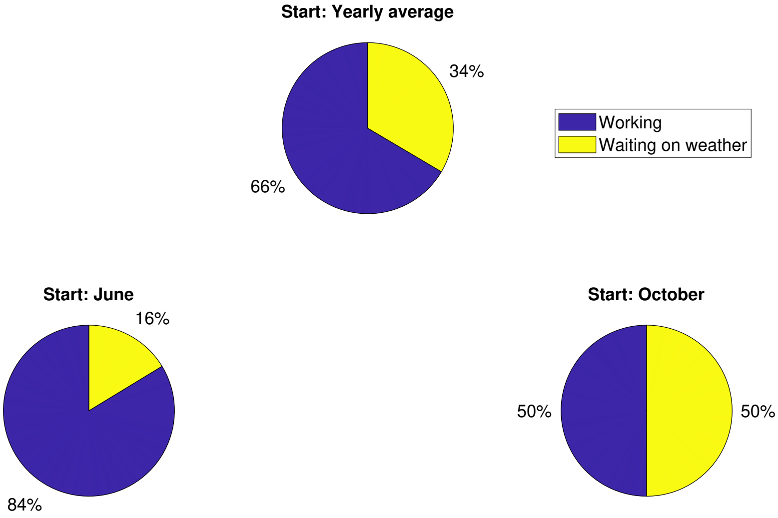

Figure 5.21: Share of weather downtime at Galloper.

The yearly average, the best and the worst months are depicted. The average weather downtime for operation around the year is 34%. The starting month resulting in the least amount of weather downtime is June with only 16% and the starting month with the largest share of downtime is October with 50%. These values are the ones for the P50 case. Again, the top tasks contributing to weather downtime are presented in Figure 5.22.

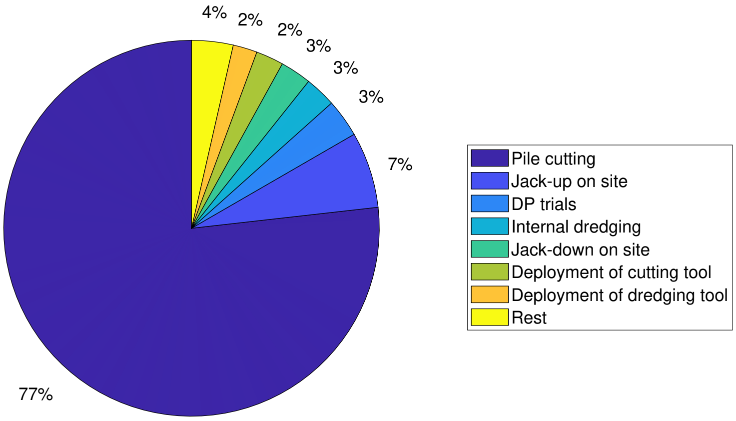

Figure 5.22: Top tasks contributing to weather downtime at Galloper.

With a share of 77% the pile cutting operation is the main contributor to the weather downtime. This is followed by the jacking operations with 10%, the DP trials with 3% and the dredging with 3%. The tool deployment into the monopile only makes up for 4% of the weather downtime. At Robin Rigg, the most downtime was due to the insertion of the tools, namely 52%. At Galloper, the downtime due to these tasks is significantly lower, as the tools can be inserted into the pile above the waterline. At Robin Rigg, the tools have to be guided through the water column with an ROV, which is associated with lower wave and current limits.

5.5. Discussion

This section contains the second part of the discussion, after the first part has already been carried out in section 4.3. This part deals with the calculation results of the case studies, the assumed cutting limit of 98% that should be reached before the monopile fails and the assumptions and results of the decommissioning plans.

Calculations of the case studies
The two case studies were used in order to carry out the previously performed calculations of the stresses in the cut and the crane loads during extraction for realistic parameter sets. The results for the stresses show that the operation is not very weather-sensitive, only for larger piles the weather sensitivity increases slightly. The chosen cutting limit of 98%, which will be discussed in more detail shortly, can be achieved for Robin Rigg even if the significant wave height of 2 m from the safe working limit is applied. It is therefore not necessary to introduce a lower limit here. With Galloper, the wave limit of 2 m cannot be imposed, but a smaller limit of 1.5 m is sufficient to be able to cut the pile up to 98% progress. In general, the cutting operation was found to be much less critical and dependent on the weather limits than was assumed at the beginning. This applies not only to smaller piles such as the Amrumbank weather mast or Robin Rigg, but also to much larger monopiles, e.g. with a diameter of 7.5 m at Galloper. Although the forces increase due to the larger diameters and the usually deeper waters, the wall thicknesses and thus the areas that take up the forces increase so that they partially compensate for this. The modal analyses for both case studies also show the same uncritical behaviour that was already observed for the Amrumbank met mast. In the case of Robin Rigg, the natural frequencies are even higher due to the shortness of the monopiles. Although they are lower for Galloper, they are still well away from the wave frequencies, which indicates that the piles are sufficiently stiff during cutting. Finally, the necessary extraction crane loads were also calculated for the two case studies. In the worst case, i.e. with the soil undisturbed, the total hook load is still significantly lower than the loads due to the original weights of the entire piles.

Assumed cutting limit
Setting a suitable cutting limit that should be reached before the monopile breaks off proved to be a major challenge. This is mainly due to the fact that, based on experience, it is difficult to classify when it is okay for a monopile to break before it is completely cut. Not many monopile decommissioning operations were carried out, and if so are not well documented. No specific wave limit was set for the Amrumbank decommissioning and therefore a standard limit for safe working on deck was used. This included a significant wave height of 2 m. During the Amrumbank decommissioning, the pile failed at a cutting progress of around 98%. As the decommissioning was successful and there were no problems during extraction or with the tool despite this rupture, a limit of 98% was also set for this work. This must be achieved before the monopile fails. The sea states that ensure that failure is reached beforehand are then no longer permissible. However, this limit represents a very conservative limit, as it is quite possible that even a fracture before a cutting progress of 98% will not lead to problems during the operation. However, the calculations of the stresses in the cut for the case studies show that even such a conservative limit hardly restricts the operation further due to the weather. Only in the case of Galloper, there was a reduction in the wave limit from 2 m to 1.5 m. However, if it would be decided to reduce the limit to be reached by only 1% to 97%, this would already mean that the operation at Galloper would also not be weather-restricted. If it can be proven that a 97% limit or lower would be okay, the operability would therefore increase. This could be carried out in future work. However, to show this probably experiments have to be carried out as modelling the damage to the cutting nozzles is difficult. This analysis furthermore strongly depends on the design of the cutting tool itself, which was not considered in this thesis. Here, the operation was designed to match to the decommissioning of the Amrumbank met mast monopile.

The reason for the limit in the first place was the mentioned possible damage to the tool's cutting nozzles. This was justified by the fact that these are directly at the breaking line and can then be damaged by a possible relative movement of the two pile sections. This assumption makes sense especially when a large number of piles must be cut in succession. Repairs to the tool that cause unnecessary waiting time on-site must be avoided at all costs. This is an argument in favour of a rather too conservative limit as assumed here.

Decommissioning schedules

For the decommissioning schedules, only the limits for the cutting itself were determined. The other routine tasks were taken from operations already carried out by RWE. This approach is useful, as determining all limits would largely extend the scope of this work. There are significant differences in the results of the decommissioning plans of the two case studies. In the case of Robin Rigg, it is important to note that no tidal limitation was taken into account. In reality, it is possible that the few turbines located in the very shallow area of the wind farm can only be reached by a vessel when the tide is high. This could result in waiting times. However, as most of the turbines are located in water depths that can also be approached at low tide, this was neglected. At Robin Rigg, the weather downtime is very low overall, even though the most weather-sensitive tasks are carried out here, in which the tools are inserted into the monopile under water with an ROV. However, as the weather conditions at Robin Rigg are so mild, even these tasks are of little consequence. In hindsight, it might have been better if a wind farm had been considered where the weather is harsher and the tools have to be guided into the pile underwater. With Galloper, the ocean climate is much harsher, but the tools can be inserted into the monopiles above the water surface. This means that with Galloper, it is not the insertion of the tools, as with Robin Rigg, but the cutting itself that provides the greatest downtime.

If the operation is to be optimised, this could best be achieved by reducing the cutting time, as this already accounts for 43% of the net time at Galloper. As the development of cutting tools progresses, it is likely that this time can be reduced in the future. Furthermore, in order to additionally optimise the operation, it could be examined whether barge transport of the monopiles would be a more effective option. This would avoid the constant transit, but an additional ship would have to be chartered. This could be investigated in further work.

It is also important to note that only the decommissioning of the monopiles was considered. Turbines and transition pieces were assumed to be already removed. As wind farms are often installed sequentially, with all monopiles being placed first, then all transition pieces and then all turbines being installed, this backwards procedure was chosen for the decommissioning as well. Further work could investigate whether it might be worthwhile to completely remove one wind turbine together with the foundation and then move on to the next. This way every location is only approached once but for a longer time. Also, all tools would be needed for a longer hire duration.

6

Conclusion and recommendations

This final chapter concludes the master's thesis. The investigations carried out are summarised once again and the main findings are presented. To this end, the research questions formulated at the beginning in subsection 1.3.2 are explicitly answered. The chapter, and therefore also the thesis, ends with a section that provides recommendations for further work on the topic.

6.1. Summary

This work dealt with the topic of monopile decommissioning for entire wind farms. The main focus was on the determination of weather limits during the cutting operation. In an initial literature review, projects that can be learnt from were presented, the basic operation for removing monopiles was described, the ASWJ cutting technique was presented and the regulatory aspects of removing the piles from the seabed were considered. Calculations were then carried out to predict the failure of the monopiles depending on external conditions. In addition, the maximum crane loads that must be applied when extracting the monopiles from the seabed were calculated. The calculations were applied to an existing decommissioning project in order to validate them. Following the validation, a parameter study was carried out. This allowed further insights into the model to be gained and the most important parameters during cutting and subsequent extraction from the seabed to be visualised. Following this in-depth model investigation, the calculations were also carried out for the monopiles of two real wind farms, allowing the behaviour of realistic parameter sets to be investigated. In addition, calculations for the decommissioning campaigns of the monopiles were carried out for the two wind farms. This enabled weather downtimes to be quantified and the tasks that contribute most to these downtimes to be identified. The results and the assumptions made in the calculation models were evaluated in two discussion sections focussing on different topics.

6.2. Main findings

The main findings of this work are presented as explicit answers to the research questions initially formulated in subsection 1.3.2 in the introduction chapter.

What is the current state of monopile decommissioning and how is it regulated in Germany and the UK?

> The decommissioning of monopiles is an issue that has not received much attention to date. However, it will become increasingly relevant in the future as more and more wind farms reach the end of their lifetime in the coming years. Wind farm operators such as RWE will then be required to decommission their assets and restore the environment as close as possible to its original state. Most initial decommissioning plans are based on the internal ASWJ cutting method as the base case for the removal technique for the monopiles. However, an examination of the guidelines issued by the authorities in Germany and the UK shows that they propose the complete removal of the foundations as the base case. This cannot be achieved by cutting, as part of the foundations always remain in the seabed. However, under special conditions, the authorities

may also permit partial removal by cutting. This depends on the technical feasibility and costs of complete removal as well as the impact on the environment. Although complete removal restores the seabed to its original state, it is unclear whether it makes sense to remove the monopiles completely for environmental reasons. The same applies to cables and scour protection, which were not considered in this study. It is therefore up to the authorities to decide which method will be favoured in the future.

How do the cutting tools work and what is important when decommissioning multiple monopiles?

An ASWJ tool cuts the monopile foundations using water pressure combined with an abrasive. Scaling the cutting technique to larger diameters and wall thicknesses is not a problem, but the operation takes longer. The cutting speed is only a few millimetres per minute, which has a significant impact on larger diameters. In order to reduce cutting times, several cutting nozzles can therefore be used evenly distributed around the circumference to shorten the cutting time. In this work, three cutting nozzles were assumed, which leads to a reduction of the cutting time to a third compared to one nozzle. This is particularly relevant if several monopiles have to be removed. In addition, the tool must be adaptable to different internal diameters, as not all monopiles in a wind farm have the same internal diameter. In the best case, the cutting tool also comes with a device for lifting the monopile to minimise the number of different types of equipment.

When in the cutting process do WTG monopiles lose their stability and fail?

The Amrumbank met mast monopile lost its stability late in the cutting process at around 98% of the circumference being cut. This dealt as a reference for the calculations in this thesis. The foundations at Robin Rigg and Galloper were used as case studies for monopiles with the sizes of those being used in actual wind farms. It was found that also these monopiles lose the largest amount of their stability and stiffness similarly late in the cutting progress. Of course, this depends on the loads acting on the monopile but at least for Robin Rigg even the largest considered loads did not cause a failure of the monopile before a cutting progress of 98%. Therefore, no special limits were applied to the Robin Rigg monopile cutting operations. The Galloper monopile was estimated to lose its stability slightly before the cutting progress of 98% when the largest loading was considered. Since this cutting process should be achieved as the selected limit, there is only a restriction in the operability limits for Galloper. In general, the monopiles lose their stability much later than was expected at the beginning of this thesis. It is only from about 95% cutting progress that the cutting surface becomes small enough that large changes in the stresses become noticeable.

What crane capacities are required for successful monopile removal from the seabed after cutting?

During the removal of a cut monopile from the seabed, the maximum crane loads are made up of the pile's own weight and the soil friction on the outer wall of the pile. Normally, the majority of the crane load comes from the weight of the pile and the shaft friction only plays a subordinate role. This only changes if the cutting depth is changed and the cut is made further below the seabed. From a certain depth, shaft friction then plays the main role. However, the extraction forces are generally lower than the forces that had to be applied when the piles had to be lifted during installation. This is due to the fact that usually around half of the pile remains in the seabed. Even the additional soil friction does not change this. For these reasons, vessels with the same or lower crane capacity than the installation vessel can be used for decommissioning.

What parameters have the most influence on the monopile's stability during cutting and on the extraction hook loads?

Considering the stresses in the cut, as expected, it is mainly greater water depths and stronger sea states that lead to an increase in stresses. What is not necessarily trivial is that larger diameters do not lead to greater but, on the contrary, to smaller tensile stresses in the cut. This is due to the fact that the cut area increases more with increasing diameter than the loads on these areas do. Another important parameter that has a major influence on the stresses in the cut is whether and how far the monopile top is below the water surface. If the transition piece has to be cut from the pile beforehand, the monopile top is below the water surface. If the transition piece is bolted, it can be unscrewed and the monopile head is above the water surface. As the hydrodynamic forces are greatest in the upper part of the water column, it makes a considerable difference whether the pile reaches there or not. Regarding the hook loads, the water depth, the pile diameter, the soil type and the cutting depth have the greatest influence. Greater water depths lead to longer and therefore heavier piles, as is the case with larger pile diameters. It also became clear that clay leads to higher shaft friction than sand. Regardless of the soil type, cutting further below the seabed also results in a significant increase in hook load. However, at the assumed cutting depth of 3 m below seabed, the pile's self weight is still governing for the hook loads.

What schedules can be expected for the decommissioning of monopiles and what role does the cutting operation play in this?

The net time for the two monopile decommissioning schedules for Robin Rigg and Galloper is approximately one day per monopile. To be precise, it is 1.08 days for Robin Rigg and 1.21 days for Galloper. This is due to the fact that cutting alone takes 7.3 h for Robin Rigg and 12.7 h for Galloper, as the piles are larger. In addition to the net time, there is the weather downtime, which is significantly longer at Galloper as the weather is much harsher. On an annual average, Galloper has a weather downtime of 34%. At Robin Rigg, this is only 9%, which is very low. As already indicated above, cutting takes up most of the time. Of the net time, this is 28% for Robin Rigg and around 43% for Galloper. However, the weather downtime at both wind farms results from different reasons. At Robin Rigg, 52% results from the tool deployments and only 20% from the cutting itself. At Galloper, the tool deployments only account for 4% of the downtime and 77% comes from the cutting itself. This is because at Robin Rigg the tools have to be guided into the pile with an ROV below the water surface and the limits for ROVs are significantly lower. At Galloper, insertion can take place above the surface of the water and ROVs are not required. So, cutting only accounts for most of the weather downtime if the monopile is sticking out of the water. If not, inserting the tools is the operation that causes the most downtime.

In general, the operability of WTG monopile decommissioning using internal cutting is good and comparable with that of installation campaigns. Therefore, this method offers a valid approach to be used in the future during decommissioning campaigns of entire wind farms. Both, small and larger monopiles from modern wind farms can be decommissioned in the same way. With further optimisations in tool development, especially with regard to cutting speed, the performance of the method can be further improved.

6.3. Possibilities for future work

This thesis has provided some insights into the still new field of applying water cutting as decommissioning method to WTG monopiles. Nevertheless, there are aspects of the thesis where further work is needed.

Firstly, more validation work should be carried out on the created model to predict pile failure. Whilst this has been successfully compared to the Amrumbank met mast decommissioning, further validation with real examples would increase confidence in the calculations. The validation using the Amrumbank met mast still leaves some uncertainty as it cannot be investigated what the exact force was that led to the failure of the pile.

In addition, other more complex methods for the stress calculation in the cut should be carried to compare the results with those from this work. As the analysis of a cut monopile was completely new, the simplest possible calculation using analytical formulae was chosen here. This provided a good result in comparison with the real example of Amrumbank, but should nevertheless be compared with other calculation methods. These methods could for example be the FEM or calculations using the theories of fracture mechanics.

In this work, it was assumed that the monopiles are not allowed to fail before a cutting progress of 98% of the circumference has been reached. This was based on the Amrumbank met mast, which is one of very few reference projects. Here, the pile broke at around 98%, the decommissioning operation was a success and the tool was not damaged. So, this was set as the minimum cutting progress to be achieved. However, it is possible that a pile that breaks beforehand, for example at 95%, will also not cause any damage to the tool. Further investigations should therefore be carried out to determine when a pile may really break so that the operation is successful. However, as this is very difficult to determine without real experience, actual projects or experiments in water tanks will probably have to be carried out. Also, the design of the tool itself and especially the nozzles plays a key role in this. Maybe a design can be developed where the nozzles are better protected against damage. Furthermore, even for the conservative limit of 98% of the cut to be achieved, most sea states could be permitted. If it was found that less than 98% cutting progress could be allowed before failure, this would therefore only change the operability of the cutting to a certain extent.

The other tasks during monopile decommissioning should be considered separately in more detail, as they have only been transferred in simplified form from other projects. Especially, the weather-sensitive insertion of the tools could be optimised with regard to the limitations. This would be particularly relevant if the tools have to be inserted underwater at a location with a similarly rough metocean climate as Galloper. One option to get around the use of ROVs would be something like a funnel attachment that could be placed on the monopile to insert the tools.

Finally, further work should be put into planning the decommissioning campaigns. In this thesis, only one concept was considered, in which all the different parts of a wind turbine are decommissioned one after the other, so that in the end all the monopiles can be decommissioned in succession. However, it could possibly make more sense to first completely decommission one wind turbine with its foundation and then move on to the next. One argument in favour of the approach used in the work is that the different components require different tools in order to be decommissioned. Also, other ships may also be advantageous for the different operations. In favour of the second option would be that each turbine only needs to be approached once.

References

[1] United Nations. *Paris Agreement*. UNTC XXVII 7.d. Dec. 12, 2015.

[2] M. Dolores Esteban et al. “Why offshore wind energy?” In: *Renewable energy* 36.2 (2011), pp. 444–450.

[3] Giuseppe Costanzo and Guy Brindley. “Wind energy in Europe. Statistics and the outlook for 2024-2030”. In: *WindEurope* (Feb. 2024).

[4] Giles Hundleby and Freeman Kate. *Unleashing Europe’s offshore wind potential. A new resource assessment*. WindEurope. June 2017. URL: `https://windeurope.org/intelligence-platform/product/unleashing-europe-s-offshore-wind-potential` (visited on 02/14/2024).

[5] Mehmet Bilgili, Abdulkadir Yasar, and Erdogan Simsek. “Offshore wind power development in Europe and its comparison with onshore counterpart”. en. In: *Renewable and Sustainable Energy Reviews* 15.2 (Feb. 2011), pp. 905–915. ISSN: 13640321. DOI: `10.1016/j.rser.2010.11.006`.

[6] Zhiyu Jiang. “Installation of offshore wind turbines: A technical review”. In: *Renewable and Sustainable Energy Reviews* 139 (2021), p. 110576.

[7] J.H. Den Boon et al. “Scour behaviour and scour protection for monopile foundations of offshore wind turbines”. In: *Proceedings of the European Wind Energy Conference*. Vol. 14. EWEC London UK. 2004, p. 26.

[8] Lizet Ramírez. “Offshore wind energy 2023 statistics”. In: *WindEurope* (Apr. 2024).

[9] Dan Kallehave et al. “Optimization of monopiles for offshore wind turbines”. In: *Philosophical Transactions of the Royal Society A: Mathematical, Physical and Engineering Sciences* 373 (2015). DOI: `10.1098/rsta.2014.0100`.

[10] K.W. Hermans and J.M. Peering. *Future XL monopile foundation design for a 10 MW wind turbine in deep water*. Design Study. Energy Research Centre of the Netherlands (ECN), Dec. 2016.

[11] Luis M. Abadie and Nestor Goicoechea. “Old wind farm life extension vs. full repowering: a review of economic issues and a stochastic application for Spain”. In: *Energies* 14.12 (2021), p. 3678.

[12] A.M. Jadali et al. “Decommissioning vs. repowering of offshore wind farms—a techno-economic assessment”. In: *The International Journal of Advanced Manufacturing Technology* 112 (2021), pp. 2519–2532.

[13] Peng Hou et al. “Offshore wind farm repowering optimization”. In: *Applied energy* 208 (2017), pp. 834–844.

[14] Department of Energy and Climate Change London. *Decommissioning of offshore renewable energy installations under the Energy Act 2004*. Mar. 2019.

[15] Eva Topham et al. “Challenges of decommissioning offshore wind farms: Overview of the European experience”. In: *Journal of Physics: Conference Series*. Vol. 1222. 1. IOP Publishing. 2019, p. 012035.

[16] 4C Offshore. *4C Offshore Database*. URL: `https://www.4coffshore.com` (visited on 02/19/2024).

[17] Gillian Smith and Graeme Lamont. “Decommissioning of Offshore Wind Installations. What we can learn”. In: *Offshore Wind Energy* (2017), pp. 6–8.

[18] e.on. *Amrumbank Met Mast Decommissioning - Project Summary*. Tech. rep. e.on, 2016.

[19] Spinergie. *Significant wave height. Amrumbank West*. URL: `https://market-intelligence.spinergie.com/dashboard/page/windfarm?windfarmId=94` (visited on 06/07/2024).

[20] Tim Müller and Ewoud Bloem. *Decom Offshore Wind Farms. Lessons Learned and Challenges*. URL: `https://www.seeoff.de/data/events-20210621-1-p89P4Dog.pdf` (visited on 02/22/2024).

[21] Patrick Rainey. *Blyth Offshore Wind Farm. Decommissioning the UKs First Offshore Wind Farm*. 2021. URL: `https://www.seeoff.de/data/events-20210621-1-Ifcd2Xli.pdf` (visited on 02/22/2024).

[22] Clemens van Gessel. *Dismantling of Irene Vorrink Wind Farm after 25 years of faithful service*. 2022. URL: `https://group.vattenfall.com/press-and-media/newsroom/2022/dismantling-of-irene-vorrink-wind-farm-after-25-years-of-faithful-service` (visited on 02/28/2024).

[23] International Martime Organization (IMO). “Guidelines and standards for the removal of offshore installations and structures on the continental shelf and in the exclusive economic zone”. In: *Pub. L. No. IMO Resolution A.* 672.16 (1989), pp. 1–9.

[24] Bundesamt für Seeschifffahrt und Hydrographie (BSH). *Standard Design. Minimum requirements concerning the constructive design of offshore structures within the Exclusive Economic Zone (EEZ)*. BSH-No.: 7005. 2021. URL: `https://www.bsh.de/DE/PUBLIKATIONEN/_Anlagen/Downloads/Offshore/Standards/Standard-Minimum-requirements-concerning-the-constructive-design-of-offshore-structures-within-the-Exclusive-Economic-Zone-EEZ-en.html` (visited on 02/23/2024).

[25] Silke Eckardt et al. *Handbook of offshore wind farm decommissioning. Framework, technologies, logistics, processes, scenarios and sustainability*. Hochschule Bremen, 2022.

[26] BEIS. *Decommissioning of offshore renewable energy installations under the Energy Act 2004. Guidance notes for industry (England and Wales)*. Mar. 2019. URL: `https://www.gov.uk/government/publications/decommissioning-offshore-renewable-energy-installations` (visited on 02/23/2024).

[27] Marine Scotland. *Decommissioning of Offshore Renewable Energy Installations in Scottish waters or in the Scottish part of the Renewable Energy Zone under The Energy Act 2004. Guidance notes for industry*. July 2022. URL: `https://www.gov.scot/publications/offshore-renewable-energy-decommissioning-guidance-scottish-waters/` (visited on 02/23/2024).

[28] Eva Topham and David McMillan. “Sustainable decommissioning of an offshore wind farm”. In: *Renewable energy* 102 (2017), pp. 470–480.

[29] Gillian Smith, Chris Garrett, and George Gibberd. “Logistics and cost reduction of decommissioning offshore wind farms”. In: *Presented EWEA Offshore* 2015 (2015), pp. 10–12.

[30] Forewind. *Dogger Bank Offshore Wind Farm Decommissioning Programme*. 2020. URL: `https://doggerbank.com/downloads/Dogger-Bank-A-and-B-Decommissioning-Programme.pdf` (visited on 02/27/2024).

[31] Katie Smyth et al. “Renewables-to-reefs? – Decommissioning options for the offshore wind power industry”. In: *Marine Pollution Bulletin* 90.1 (2015), pp. 247–258. ISSN: 0025-326X. DOI: `https://doi.org/10.1016/j.marpolbul.2014.10.045`.

[32] Scira Offshore Energy. *Statoil Decommissioning Programme Sheringham Shoal*. 2014. URL: `https://www.scira.co.uk/downloads/Decommissioning%20Programme%20SCIRA%20SC-00-NH-F15-00005_07.pdf` (visited on 02/27/2024).

[33] Nils Hinzmann et al. “Measurements of hydro sound emissions during internal jet cutting during monopile decommissioning”. In: *COME-Conference on Maritime Energy 2017-Decommissioning of Offshore Geotechnical Structures, 28.-29. März 2017 in Hamburg, S. 139*. Vol. 161. 2017.

[34] RGL Services. *Monopile Cut Internally by Abrasive Water Jet*. URL: `https://www.rglservices.co.uk/services/underwater-pile-cutting` (visited on 06/09/2024).

[35] Kenneth Bisgaard Christensen, Shahin Jalili, and Alireza Maheri. “A Comparative Assessment of Cutting Techniques for Offshore Energy Structures”. In: *2022 7th International Conference on Environment Friendly Energies and Applications (EFEA)*. Dec. 2022, pp. 1–6. DOI: `10.1109/EFEA56675.2022.10063821`.

[36] Wesam Salah Alaloul et al. “Multi-nozzle abrasive water jet for oil and gas platforms decommissioning: A review”. In: *Civil Engineering and Architecture* 9.6 (2021), pp. 2062–2076.

[37] RGL Services. *Abrasive Jet Cutting Speed*. URL: `https://www.rglservices.co.uk/Jet-cutting-Graph.jpg` (visited on 06/09/2024).

[38] Stuart Bradley. *End of Life Opportunities*. 2014. URL: `https://s3-eu-west-1.amazonaws.com/assets.eti.co.uk/legacyUploads/2014/06/End-of-life-for-offshore-wind-EI-June-2014UPDATED.pdf` (visited on 02/28/2024).

[39] Eva Topham et al. “Recycling offshore wind farms at decommissioning stage”. In: *Energy policy* 129 (2019), pp. 698–709.

[40] World Steel Association et al. “Steel solutions in the green economy: Wind turbines”. In: *World Steel Association* (2012).

[41] Marylise Schmid et al. *Accelerating Wind Turbine Blade Circularity*. 2020. URL: `https://windeurope.org/wp-content/uploads/files/about-wind/reports/WindEurope-Accelerating-wind-turbine-blade-circularity.pdf` (visited on 02/28/2024).

[42] Jonas Pagh Jensen and Kristen Skelton. “Wind turbine blade recycling: Experiences, challenges and possibilities in a circular economy”. In: *Renewable and Sustainable Energy Reviews* 97 (2018), pp. 165–176.

[43] Siemens Gamesa. 2021. URL: `https://www.siemensgamesa.com/en-int/-/media/siemensgamesa/downloads/en/sustainability/environment/siemens-gamesa-20210901-recyclableblade-infographic-finalen.pdf` (visited on 02/28/2024).

[44] DNV-RP-C205. *Environmental conditions and environmental loads*. Standard. Høvik, NO: DNV, Sept. 2021.

[45] Bernard LeMéhauté. *An introduction to hydrodynamics and water waves*. Vol. 52. Environmental Science Servies Administration, 1969.

[46] Klaus Hasselmann et al. “Measurements of wind-wave growth and swell decay during the Joint North Sea Wave Project (JONSWAP).” In: *Ergaenzungsheft zur Deutschen Hydrographischen Zeitschrift, Reihe A* (1973).

[47] RC MacCamy and RA Fuchs. *Wave forces on piles: a diffraction theory*. 69. US Beach Erosion Board, 1954.

[48] Mohibb Ghani Malik. *Hydrodynamic Modelling Effects on Fatigue Calculations for Monopile Offshore Wind Turbines*. en. 2016.

[49] Ivar Langen and Ragnar Sigbjörnsson”. *Dynamisk analyse av konstruksjoner (Dynamic analysis of structures)*. 1979.

[50] Guido Dhondt. *Ten-node tetrahedral element*. 2014. URL: `https://web.mit.edu/calculix_v2.7/CalculiX/ccx_2.7/doc/ccx/node33.html` (visited on 06/08/2024).

[51] Federico Pisano. “Piled Foundations - Axial Loading”. In: *Offshore Geotechnical Engineering, TU Delft* (2022).

[52] API RP 2A-WSD. *Planning, Designing, and Constructing Fixed Offshore Platforms*. Standard. API, Nov. 2014.

[53] DNV-ST-N001. *Marine operations and marine warranty*. Standard. Høvik, NO: DNV, Dec. 2023.

[54] ABPmer. *Weather Downtime Express (WDTX)*. URL: `https://www.seastates.net/weather-downtime-express/` (visited on 07/09/2024).

[55] Shanghui Yang, Xiaowei Deng, and Jun Yang. “Modeling of soil-pile-structure interaction for dynamic response of standalone wind turbines”. In: *Renewable Energy* 186 (2022), pp. 394–410.

[56] RWE. *Decommissioning Programme. Robin Rigg*. Report. RWE, 2023.

[57] Google Maps. *Robin Rigg Wind Farm*. 2024. URL: `https://www.google.com/maps` (visited on 03/04/2024).

[58] Spinergie. *Robin Rigg (Wind farm)*. 2024. URL: `https://market-intelligence.spinergie.com/dashboard/page/windfarm?windfarmId=44` (visited on 06/18/2024).

[59] John M. Harris, Richard J.S. Whitehouse, and James Sutherland. “Marine Scour and Offshore Wind: Lessons Learnt and Future Challenges”. In: *International Conference on Offshore Mechanics and Arctic Engineering*. Vol. 44373. 2011, pp. 849–858.

[60] Mathalino. *Unit Weights and Densities of Soil*. 2024. URL: `https://mathalino.com/reviewer/geotechnical-engineering/unit-weights-and-densities-soil` (visited on 06/18/2024).

[61] ABPmer. *SEASTATES. ABPmer Data Explorer*. Cell: 3.68 W, 54.78 N. 2024. URL: `https://www.seastates.net/explore-data/` (visited on 03/07/2024).

[62] National Tidal and Sea Level Facility. *Definitions of tidal levels and other parameters*. URL: `https://ntslf.org/tgi/definitions` (visited on 03/07/2024).

[63] National Tidal and Sea Level Facility. *Workington tide gauge site*. URL: `https://ntslf.org/tgi/portinfo?port=Workington` (visited on 03/07/2024).

[64] RWE. *Decommissioning Programme. Galloper*. Report. RWE, 2023.

[65] Google Maps. *Coordinates: 51.89224, 2.03471*. 2024. URL: `https://www.google.com/maps` (visited on 06/18/2024).

[66] Spinergie. *Galloper (Wind farm)*. 2024. URL: `https://market-intelligence.spinergie.com/dashboard/page/windfarm?windfarmId=1` (visited on 06/18/2024).

[67] A Gens. “On the hydromechanical behaviour of argillaceous hard soils-weak rocks”. In: *Proceedings of the 15th European Conference on soil mechanics and geotechnical engineering-geotechnics of hard soils-weak rocks*. Vol. 4. IOS Press. 2013, pp. 71–118.

[68] National Tidal and Sea Level Facility. *Harwich tide gauge site*. URL: `https://ntslf.org/tgi/portinfo?port=harwich` (visited on 06/18/2024).

[69] Nicoguaro. “Typical Stress vs. Strain Diagram for a Ductile Material (e.g. Steel)”. In: *Wikimedia Commons, the Free Media Repository* (May 2020).

[70] BS-EN-ISO 14688-2. *Geotechnical investigation and testing. Identification and classification of soil. Principles for a classification*. Standard. Jan. 2006.

A

Additional theory

This chapter of the appendix contains additional theory. This content is overly detailed or extensive, so its inclusion in the main body of the thesis is unnecessary for comprehension and potentially detrimental to readability. Nonetheless, it is considered relevant to the thesis and is therefore included here.

A.1. Wave dynamics

Equation A.1 shows the formula for calculating the free surface elevation of an irregular wave calculated with Stokes second-order wave theory.

$$\eta_s = \eta_l + \frac{\pi H^2}{8\lambda}\frac{\cosh(kd)}{\sinh(kd)^3}(2+\cosh(2kd))\cos(2(\omega t+\epsilon)) \tag{A.1}$$

Equation A.2 and Equation A.3 show the formulas for calculating the wave velocities and accelerations with linear wave theory.

$$u_{w,l} = \frac{\pi H}{T}\frac{\cosh(k(z+d))}{\sinh(kd)}\cos(\omega t+\epsilon) \tag{A.2}$$

$$\dot{u}_{w,l} = \frac{2\pi^2 H}{T^2}\frac{\cosh(k(z+d))}{\sinh(kd)}\sin(\omega t+\epsilon) \tag{A.3}$$

Equation A.4 and Equation A.5 show the formulas for calculating the wave velocities and accelerations with Stokes second-order wave theory.

$$u_{w,s} = u_{w,l} + \frac{3}{4}\frac{\pi H}{T}\frac{\pi H}{\lambda}\frac{\cosh(2k(z+d))}{\sinh^4(kd)}\cos(2(\omega t+\epsilon)) \tag{A.4}$$

$$\dot{u}_{w,s} = \dot{u}_{w,l} + \frac{3\pi^2 H}{T^2}\frac{\pi H}{\lambda}\frac{\cosh(2k(z+d))}{\sinh^4(kd)}\sin(2(\omega t+\epsilon)) \tag{A.5}$$

A.2. MacCamy-Fuchs correction

Figure A.1 presents the graphs for A and α which are used in the MacCamy-Fuchs correction. Both are complex functions that use the pile diameter D and the wave length λ (here L) as input values.

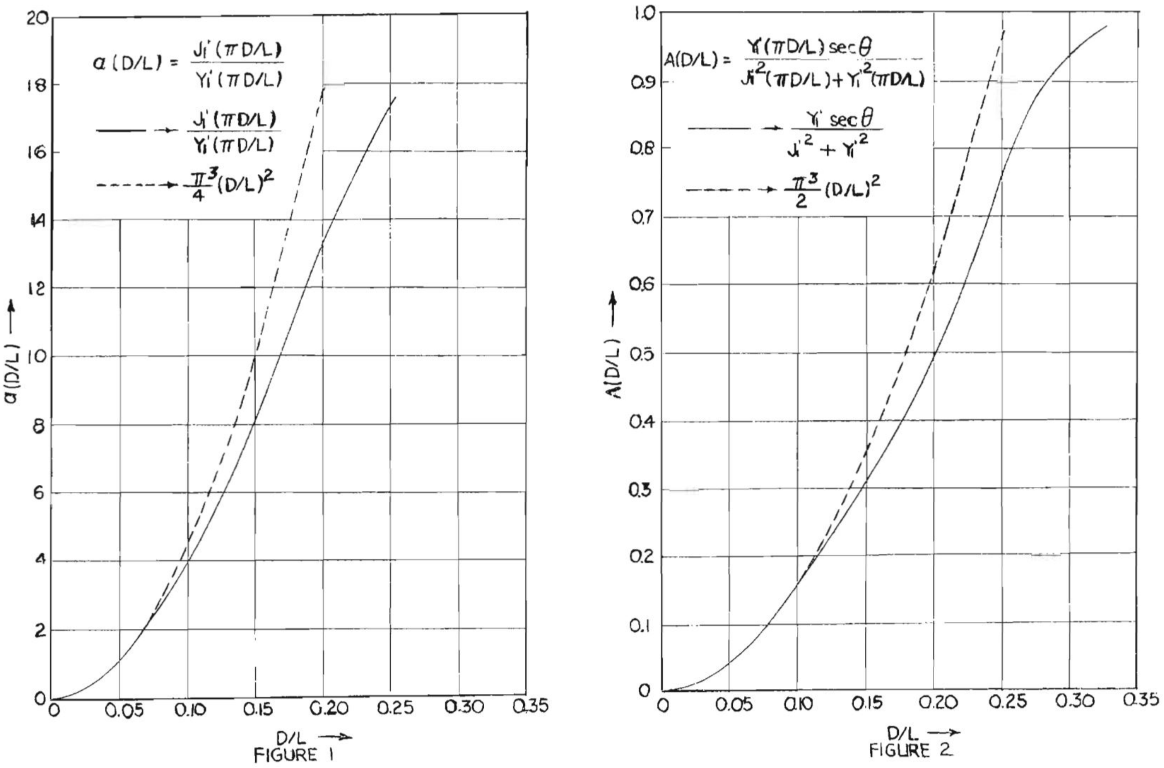

Figure A.1: Graphs for A and α values from MacCamy-Fuchs correction.

Source: [47]

A.3. Stress-strain-diagram

Figure A.2 presents a typical stress-strain curve of a ductile material like steel. The yield strength can be seen, together with the ultimate strength which was used as failure limit in this thesis. Furthermore, the elastic, the strain-hardening and necking regions are shown.

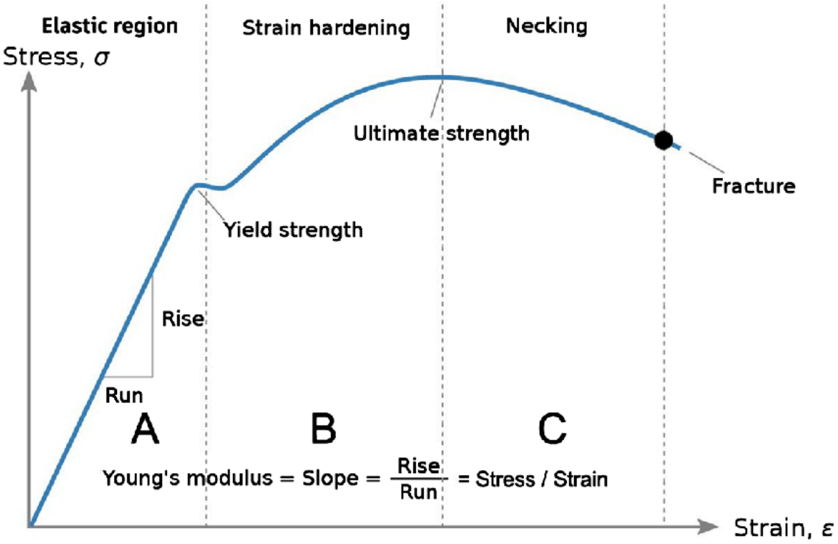

Figure A.2: Typical stress vs. strain diagram for a ductile material (e.g. steel).

Source: [69]

A.4. Soil parameters

Here, additional parameters for the calculations regarding the soil are provided. Figure A.3 presents typical values for the undrained shear strength of clay, Figure A.4 shows typical values for the saturated and buoyant unit weights of different soil types and Figure A.5 provides typical values for the shaft friction factor and limit for different types of sandy soils.

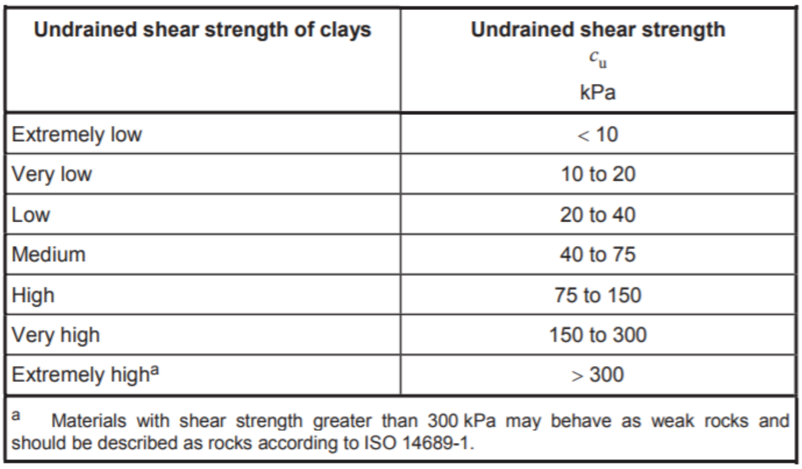

Undrained shear strength of clays	**Undrained shear strength** c_u kPa
Extremely low	< 10
Very low	10 to 20
Low	20 to 40
Medium	40 to 75
High	75 to 150
Very high	150 to 300
Extremely high[a]	> 300

[a] Materials with shear strength greater than 300 kPa may behave as weak rocks and should be described as rocks according to ISO 14689-1.

Figure A.3: Undrained shear strenghts of clay.

Source: [70]

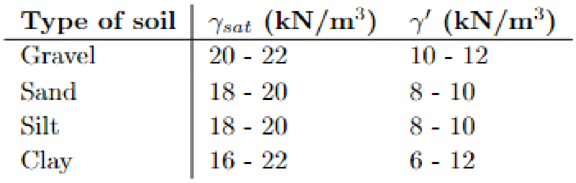

Type of soil	γ_{sat} **(kN/m^3)**	γ' **(kN/m^3)**
Gravel	20 - 22	10 - 12
Sand	18 - 20	8 - 10
Silt	18 - 20	8 - 10
Clay	16 - 22	6 - 12

Figure A.4: Unit weights for different soils.

Source: [60]

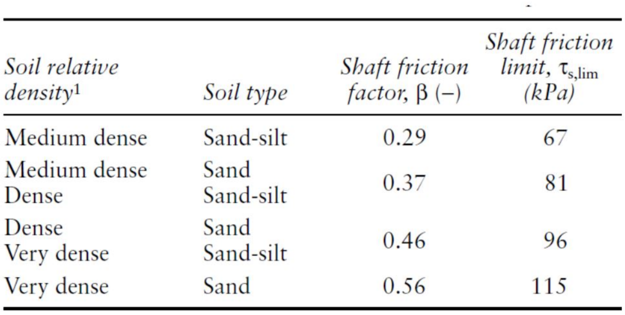

Soil relative density[1]	*Soil type*	*Shaft friction factor, β (–)*	*Shaft friction limit, $\tau_{s,lim}$ (kPa)*
Medium dense	Sand-silt	0.29	67
Medium dense Dense	Sand Sand-silt	0.37	81
Dense Very dense	Sand Sand-silt	0.46	96
Very dense	Sand	0.56	115

Figure A.5: Shaft friction factor and shaft friction limit for different sandy soils.

Source: [51]

A.5. Calculation update

During a progress meeting, a mistake in the calculation of the load in the uncut sections became clear. In the main thesis body the correct calculation is applied. However, the mistake and its influence shall be considered here in the appendix. In comparison to Figure 3.7, the line across which the moment is split into a tensile and compressive force was set in the middle of the pile, as can be seen in Figure A.6.

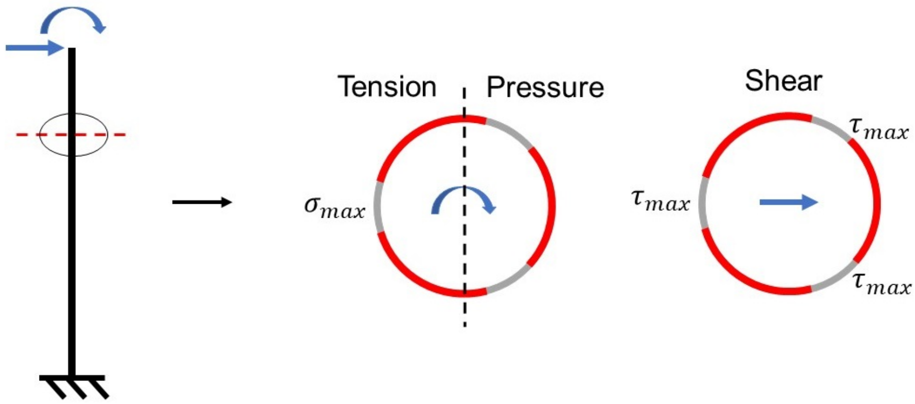

Figure A.6: Maximum tensile and shear stresses in the model (wrong calculation).

This way, the compressive and tensile forces are not in equilibrium as they should be. Furthermore the whole diameter was used for the splitting of the force, i.e. X was set to 1. In the correct calculation X is set to 0.75, to have equilibrium between tensile and compressive forces. The effect is quite significant, as the axial load in Equation 3.9 becomes 33% larger with the correct value of X. A comparison of the tensile stresses in the base case is provided in Figure A.7. The shear stresses are not affected by this.

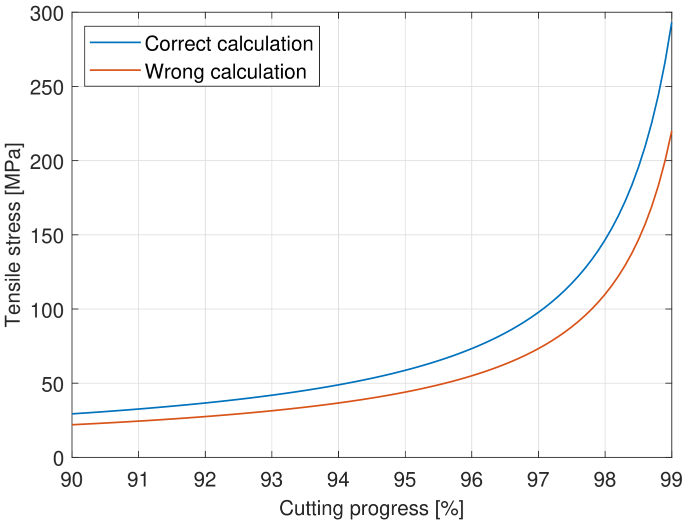

Figure A.7: Tensile stress calculation results for the base case of the parameter variation (wrong calculation).

B

Additional information on the case studies

This chapter of the appendix contains additional information regarding the case studies. As in the previous appendix with the additional theory, the inclusion of this content in the main body of the thesis is unnecessary but considered relevant to the thesis and is therefore included here.

B.1. Case study parameters

Table B.1 and Table B.2 present an overview of the parameters used in the calculations regarding the respective case study.

Table B.1: Parameter set of the Robin Rigg case study.

Variable	Value	Variable	Value
Water depth d	19.54 m (LAT) - 28.77 m (HAT)	Cutting depth d_c	3 m
Sea water density ρ_{sw}	1025 kg/m^3	Pile top below MSL $z_{c,1}$	3.14 m (LAT) - 12.37 m (HAT)
Significant wave height H_s	0.5 m - 2 m	Marine growth thickness t_{mg}	see Table 5.3
Wave period T_p	4 s - 12 s	Marine growth density ρ_{mg}	1400 kg/m^3
Current velocity u_c	1.3 m/s	Sand friction coefficient β	0.46
Gravity g	9.81 m/s^2	Sand buoyant weight γ_s'	10 kN/m^3
Pile diameter D_o	4.3 m		
Wall thickness t_w	55 mm		
Steel density ρ_s	7850 kg/m^3		

Table B.2: Parameter set of the Galloper case study.

Variable	Value	Variable	Value
Water depth d	35.94 m (LAT) - 40.2 m (HAT)	Cutting depth d_c	3 m
Sea water density ρ_{sw}	1025 kg/m^3	Pile top below MSL $z_{c,1}$	0 m
Significant wave height H_s	0.5 m - 2 m	Marine growth thickness t_{mg}	see Table 5.3
Wave period T_p	4 s - 12 s	Marine growth density ρ_{mg}	1400 kg/m^3
Current velocity u_c	1.5 m/s	Clay undrained shear strength s_u	50 kPa
Gravity g	9.81 m/s^2	Clay buoyant weight γ_c'	12 kN/m^3
Pile diameter D_o	7.5 m		
Wall thickness t_w	115 mm		
Steel density ρ_s	7850 kg/m^3		

B.2. Overview of decommissioning tasks

Table B.3, Table B.4, Table B.5 and Table B.6 present an overview of the tasks, their net duration and their limits that are carried out during the monopile decommissioning at Robin Rigg and Galloper. For every case study two tables are provided, one without and one with consideration of the alpha factors from Table 3.2 and Table 3.3.

Table B.3: Input list of tasks with operational limits for Robin Rigg.

Task	Net duration [h]	Wave limit H_s [m]	Wind limit V_w [m/s]	Wind ref. height [m]	Wind avg. period [s]	Current limit V_c [m/s]
Jack-down in port	1	1.5	15	10	600	1
Leave port	0.5	2.5	15	10	600	-
Transit (84 nm, 11 kn)	7.73	2.5	20	10	600	-
DP trials	2	1.5	15	10	600	1
Jack-up on site	2	1.5	15	10	600	1
Preparation of equipment	1	2	15	50	600	-
Retrieval of marker buoy	1	2	15	50	600	-
Deployment of dredging tool	1	1	15	50	600	1
Dredging operation	1	2	15	50	600	-
Recovery of dredging tool	0.5	2	15	50	600	-
Deployment of pile cutter	1	1	15	50	600	1
Cutting preparation	1	2	15	50	600	1.3
Pile cutting	7.3	2	15	50	600	1.3
Recovery of monopile	1	2	15	50	600	1.3
Down-ending of monopile	0.5	2	15	50	600	-
Seafastening	0.5	2	15	10	600	-
Jack-down on site	2	1.5	15	10	600	1
Sailing to next location	0.5	2.5	20	10	600	-
...	...	...	...	...	...	...
Jack-up in port	1	1.5	15	10	600	1
Load out	2	2	15	50	600	-

Table B.4: Input list of tasks with operational limits (including alpha factors) for Robin Rigg.

Task	Net duration [h]	Wave limit H_s [m]	Wind limit V_w [m/s]	Wind ref. height [m]	Wind avg. period [s]	Current limit V_c [m/s]
Jack-down in port	1	1.11	13.5	10	600	1
Leave port	0.5	2.03	13.5	10	600	-
Transit (84 nm, 11 kn)	7.73	2.03	16	10	600	-
DP trials	2	1.11	12	10	600	1
Jack-up on site	2	1.11	12	10	600	1
Preparation of equipment	1	1.6	13.5	50	600	-
Retrieval of marker buoy	1	1.6	13.5	50	600	-
Deployment of dredging tool	1	0.68	13.5	50	600	1
Dredging operation	1	1.6	13.5	50	600	-
Recovery of dredging tool	0.5	1.6	13.5	50	600	-
Deployment of pile cutter	1	0.68	13.5	50	600	1
Cutting preparation	1	1.6	13.5	50	600	1.3
Pile cutting	7.3	1.6	12	50	600	1.3
Recovery of monopile	1	1.6	13.5	50	600	1.3
Down-ending of monopile	0.5	1.6	13.5	50	600	-
Seafastening	0.5	1.6	13.5	10	600	-
Jack-down on site	2	1.11	12	10	600	1
Sailing to next location	0.5	2.03	16	10	600	-
...	...	...	...	...	...	...
Jack-up in port	1	1.11	13.5	10	600	1
Load out	2	1.6	12	50	600	-

Table B.5: Input list of tasks with operational limits for Galloper.

Task	Net duration [h]	Wave limit H_s [m]	Wind limit V_w [m/s]	Wind ref. height [m]	Wind avg. period [s]	Current limit V_c [m/s]
Jack-down in port	1	1.5	15	10	600	1
Leave port	0.5	2.5	15	10	600	-
Transit (35 nm, 11 kn)	3.18	2.5	20	10	600	-
DP trials	2	1.5	15	10	600	1
Jack-up on site	2	1.5	15	10	600	1
Preparation of equipment	1	2	15	50	600	-
Retrieval of marker buoy	1	2	15	50	600	-
Deployment of dredging tool	1	2	15	50	600	-
Dredging operation	2	2	15	50	600	-
Recovery of dredging tool	0.5	2	15	50	600	-
Deployment of pile cutter	1	2	15	50	600	-
Cutting preparation	1	2	15	50	600	1.5
Pile cutting	12.7	1.5	15	50	600	1.5
Recovery of monopile	1	2	15	50	600	1.5
Down-ending of monopile	0.5	2	15	50	600	-
Seafastening	0.5	2	15	10	600	-
Jack-down on site	2	1.5	15	10	600	1
Sailing to next location	0.5	2.5	20	10	600	-
...	...	...	...	...	...	...
Jack-up in port	1	1.5	15	10	600	1
Load out	2	2	15	50	600	-

Table B.6: Input list of tasks with operational limits (including alpha factors) for Galloper.

Task	Net duration [h]	Wave limit H_s [m]	Wind limit V_w [m/s]	Wind ref. height [m]	Wind avg. period [s]	Current limit V_c [m/s]
Jack-down in port	1	1.11	13.5	10	600	1
Leave port	0.5	2.03	13.5	10	600	-
Transit (84 nm, 11 kn)	3.18	2.03	16	10	600	-
DP trials	2	1.11	12	10	600	1
Jack-up on site	2	1.11	12	10	600	1
Preparation of equipment	1	1.6	13.5	50	600	-
Retrieval of marker buoy	1	1.6	13.5	50	600	-
Deployment of dredging tool	1	1.6	13.5	50	600	1
Dredging operation	1	1.6	13.5	50	600	-
Recovery of dredging tool	0.5	1.6	13.5	50	600	-
Deployment of pile cutter	1	1.6	13.5	50	600	1
Cutting preparation	1	1.6	13.5	50	600	1.5
Pile cutting	12.7	1.11	12	50	600	1.5
Recovery of monopile	1	1.6	13.5	50	600	1.5
Down-ending of monopile	0.5	1.6	13.5	50	600	-
Seafastening	0.5	1.6	13.5	10	600	-
Jack-down on site	2	1.11	12	10	600	1
Sailing to next location	0.5	2.03	16	10	600	-
...	...	...	...	...	...	...
Jack-up in port	1	1.11	13.5	10	600	1
Load out	2	1.6	12	50	600	-

C

Additional results

This chapter presents additional results that are not directly relevant to the understanding of the work, but should nevertheless be shown.

C.1. Mode shapes

Figure C.1 presents the mode shapes for the Amrumbank met mast monopile without any cutting. These mode shapes are very similar to the ones with the pile being cut, indicating not large changes in the dynamic behavior. This was confirmed by analysing the modal frequencies of these shapes and their development with the cutting progress.

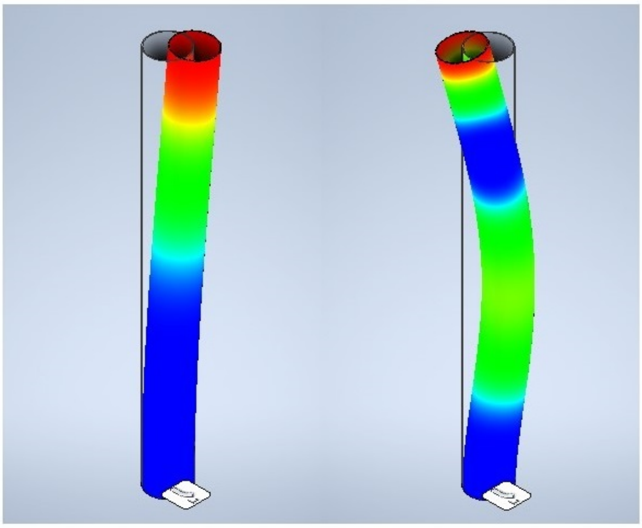

Figure C.1: Mode shapes of the uncut Amrumbank met mast monopile.

C.2. Diameter variation

Figure C.2 shows the maximum permissible moment at the cutting depth with varying monopile diameter and cutting progress. The permissible moment directly relates to the area of the cut surface. In the main body of the thesis, it was already shown, that this area increases quadratically with the diameter. When only looking at a constant cutting progress, this observation can also be made her in Figure C.2. Additionally, it can be seen that this effect largely decreases with progressing cut as the area becomes generally smaller.

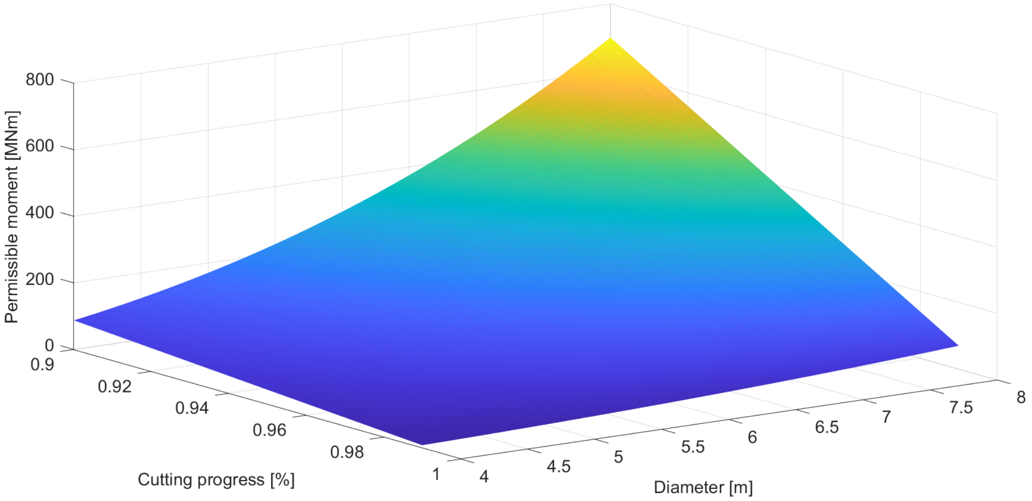

Figure C.2: Maximum permissible moment with variations of the diameter and cutting progress.

C.3. Mesh convergence

Figure C.3 and Figure C.4 present the mesh convergence checks for the Robin Rigg and Galloper case studies. Again, convergence can be observed: The frequency differences between the second smallest and smallest considered element are smaller than 1% for all four depicted plots.

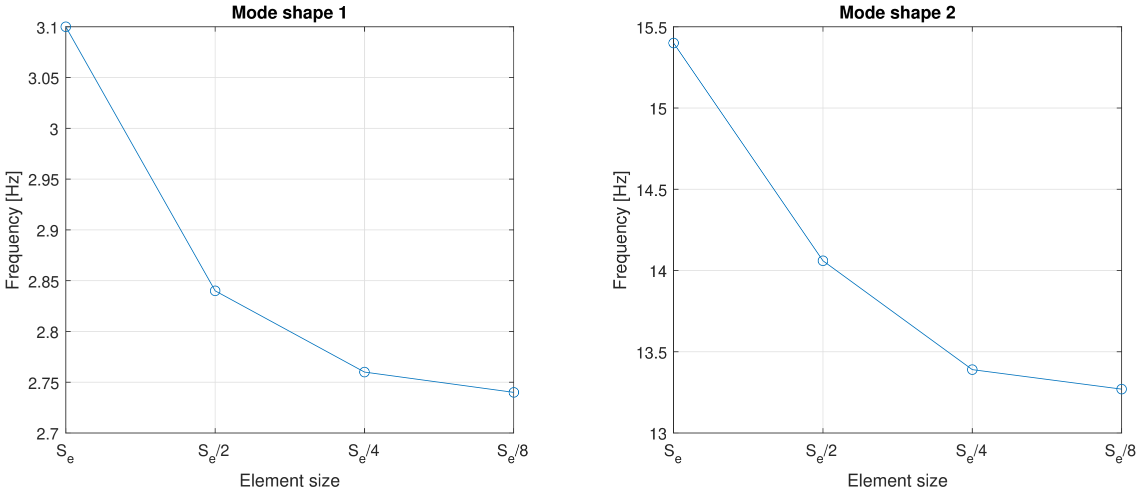

Figure C.3: Convergence study for the Robin Rigg case study monopile.

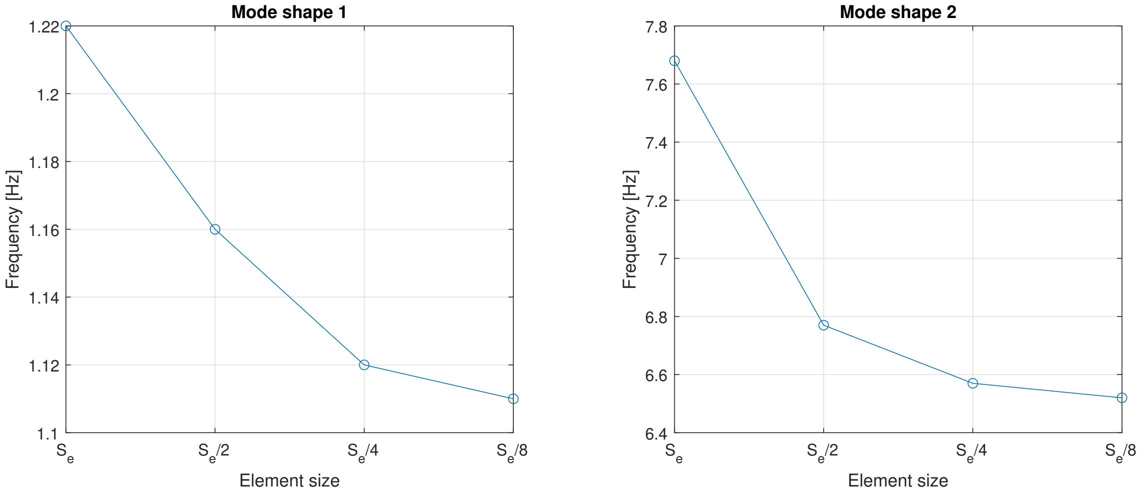

Figure C.4: Convergence study for the Galloper case study monopile.

D

MATLAB code

This chapter presents the MATLAB code that was developed in this thesis to calculated the stresses in the cut line and the hook loads during extraction of the monopile from the seabed. In the following a distinction between these two calculations is made as they are independent from each other.

D.1. Stress calculation

Here, the main script of the cutting calculation and all used functions are provided.

```matlab
%% Cutting Main Script %%

% This script calculates the stresses in the unuct sections. Tensile
% stresses and shear stresses are considered. These stresses result from
% the maximum hydrodynamic loads on the monopile and vary with the cut
% progression.

clear; clc;

set(0,'defaultTextInterpreter','none');
set(0,'DefaultLineLineWidth', 1);

%% Parameters

% General
t = 0.1:0.1:3600;                                                           % time series [s]
g = 9.81;                                                                   % gravity
    constant [m/s^2]
rho_sw = 1025;                                                              % sea water
    density [kg/m^3]
v_c = 0.03;                                                                 % cutting speed
    (3 nozzles) [m/min]

% Environmental
d = 25;                                                                     % water depth [m]
z = linspace(-d,0,200)';                                                    % z-coordinate [m
    ]
u_c = 0;                                                                    % current
    velocity [m/s]
H_s = 1; T_p = 8;                                                           % significant
    wave height [m] and peak period [s]

% Foundation
D_o_mp = 5;                                                                 % monopile outer
    diameters [m]
th_mg = 0.08; D_o = D_o_mp+2*th_mg;                                         % marine growth
    thickness and asscoiated outer diameter [m]
k_mg = 5e-2; delta_mg = k_mg/D_o_mp;                                        % marine growth
    surface roughness [m] and relative roughness [-]
```

```
Dt = 80; th_w = D_o_mp/Dt; D_i = D_o_mp-2*th_w; U_i = pi*D_i;               % D/t ratio, wall
     thickness, internal diameter and circumference [m]
cutProg = (0.9:0.001:0.99); A_c = pi/4*(D_o_mp^2-D_i^2)*(1-cutProg);        % cutting
    progress [%] and (declining) area of cut-line [m^2]
t_c = 0.1*U_i/v_c/60; n_sim = ceil(t_c*10);                                 % cutting time [h
    ] and number of simulations [-]
z_c1 = -5; d_c = 3;                                                         % distance of
    pile top below waterline and cutting depth [m]

%% Calculation

% Hydrodynamic loading

u_Mat = zeros(n_sim,length(z),length(t));
a_Mat = zeros(n_sim,length(z),length(t));
F_h = zeros(n_sim,1); M_h = zeros(n_sim,1);

for i = 1:n_sim
    % Creating matrices for eta, u and a
    [~,u_Mat(i,:,:),a_Mat(i,:,:)] = ...
        waveKinematics(t,g,d,z,H_s,T_p);
    % Finding the largest forcing
    u_w(:,:) = u_Mat(i,:,:); a_w(:,:) = a_Mat(i,:,:);
    % Drag and inertia coefficients
    condition_FCalc = 2*pi/kSolve(1/T_p,d,g)/mean(D_o);
    if condition_FCalc >= 5
        K_C = max(abs(u_w+u_c),[],'all')*T_p/mean(D_o);
        C_D = 1.05;
        if K_C <= 3
            C_M = 2;
        else
            C_M = max([2-0.044*(K_C-3),1.6-(C_D-0.65)]);
        end
    else
        C_MMFmat = [0 0; 1 0.25; 2 0.75;
            3 1.25; 4 1.7; 5 1.85];
        C_M = interp1(C_MMFmat(:,1),C_MMFmat(:,2), ...
            condition_FCalc);
        C_D = 1.05;
    end
    % Force integration
    f_mat = rho_sw*pi*D_o.^2/4*C_M.*a_w + ...
        0.5*rho_sw*D_o*C_D.*(u_w+u_c).*abs(u_w+u_c);
    F_h(i) = max(trapz(z(z<=z_c1),f_mat(z<=z_c1,:)));
    M_h(i) = max(trapz(z(z<=z_c1),f_mat(z<=z_c1,:).*(d+z(z<=z_c1))));
end

% Stresses

[M_max,idx] = max(M_h+F_h*d_c);
F_v = M_max/(0.75*D_o_mp);
sigma_y = zeros(length(A_c),1);
sigma_t = zeros(length(A_c),1);

for i = 1:length(A_c)
    sigma_y(i) = F_v/(A_c(i)/3)/10^6;
    sigma_t(i) = F_h(idx)/A_c(i)/10^6;
end
```

```
function [eta_w,u_w,a_w] = waveKinematics(t,g,d,z,H_s,T_p)

% This function calculates time series of the wave kinematics. These
% consist of the free surface elevation eta_w, the particle velocity u_w
% and the particle acceleration a_w.

f_HC = 1; dur = max(t); df = 1/dur; f = df:df:f_HC;                         % cut off
    frequency for JONSWAP spectrum, frequency step size and vector
eps_w = rand(1,length(f))*2*pi;                                             % random
    unidirectional phase

% Calculation of the gamma factor of the JONSWAP spectrum
```

```
if T_p/sqrt(H_s) <= 3.6
    gamma_JS = 5;
elseif T_p/sqrt(H_s) > 3.6 && T_p/sqrt(H_s) < 5
    gamma_JS = exp(5.75-1.15*T_p/sqrt(H_s));
elseif T_p/sqrt(H_s) >= 5
    gamma_JS = 1;
end

[~,amp] = jonswap(H_s,T_p,f,df,gamma_JS);
k = kSolve(f,d,g); omega = 2*pi*f;

% Determination of wave theory (linear or Stokes)
cond_1 = H_s/(g*T_p^2);
cond_2 = d/(g*T_p^2);
el_MH = 0.0214;

if cond_1 > 0.001 || (cond_1 > cond_2*el_MH) % Stokes
    etaHat_l = amp.*exp(1i*eps_w);                                     % complex form of eta_w
    etaHat = etaHat_l+amp.^2.*k/4.*cosh(k*d)./sinh(k*d).^3.* ...
        (2+cosh(2*k*d)).*exp(2*1i*eps_w);
    etaHat = pad2(etaHat,length(t));
    M = length(etaHat);

    eta_w = real(ifft(etaHat))*M;                                      % inverse FFT of eta_w to obtain time series

    u_w = zeros(length(z),length(t));
    a_w = zeros(length(z),length(t));

    for i = 1:length(z)
        uHat_l = omega.*amp.*cosh(k.*(z(i)+d))./sinh(k*d).*exp(1i*eps_w);   % complex form of u_w
        uHat = uHat_l + 3*omega.*k.*amp.^2/4.* ...
            cosh(2*k.*(z(i)+d))./sinh(k.*d).^4.*exp(2*1i*eps_w);
        uHat = pad2(uHat,length(t));
        M = length(uHat);
        u = real(ifft(uHat))*M;                                        % inverse FFT of u_w to obtain time series
        u_w(i,:) = u;
    end

else % linear
    etaHat = amp.*exp(1i*eps_w);                                       % complex form of eta_w
    etaHat = pad2(etaHat,length(t));
    M = length(etaHat);

    eta_w = real(ifft(etaHat))*M;                                      % inverse FFT of eta_w to obtain time series

    u_w = zeros(length(z),length(t));
    a_w = zeros(length(z),length(t));

    for i = 1:length(z)
        uHat = omega.*amp.*cosh(k.*(z(i)+d))./sinh(k*d).*exp(1i*eps_w);     % complex form of u_w
        uHat = pad2(uHat,length(t));
        M = length(uHat);
        u = real(ifft(uHat))*M;                                        % inverse FFT of u_w to obtain time series
        u_w(i,:) = u;
    end
end

for i = 1:length(z)
    u_calc = u_w(i,:);
    a_calc = gradient(u_calc,t);                                       % numerical derivation of u_w to obtain a_w
    a_w(i,:) = a_calc;
end
```

```matlab

end
```

```matlab
function [S,amp] = jonswap(H_s,T_p,f,df,gamma_JS)

% This function produces the JONSWAP spectrum for a given set of sea
% conditions. From that, the amplitudes for eta_w, u_w and a_w, which are
% needed in the waveKinematics function, are calculated.

S = zeros(1,length(f));
fp = 1/T_p;

for i = 1:length(f)
    if f(i) <= fp
        sigma = 0.07;
        pwrJS = exp(-0.5*((f(i)/fp-1)/sigma)^2);
        S(i) = 0.3125*H_s^2*T_p*(f(i)/fp)^-5*exp(-1.25*(f(i)/fp)^-4)* ...
            (1-0.287*log(gamma_JS))*gamma_JS^pwrJS;
    else
        sigma = 0.09;
        pwrJS = exp(-0.5*((f(i)/fp-1)/sigma)^2);
        S(i) = 0.3125*H_s^2*T_p*(f(i)/fp)^-5*exp(-1.25*(f(i)/fp)^-4)* ...
            (1-0.287*log(gamma_JS))*gamma_JS^pwrJS;
    end
end

amp = sqrt(2*S*df);

end
```

```matlab
function [k_vec] = kSolve(f,d,g)

% This function calculates the wave numbers by solving the implicit
% dispersion relation numerically.

omega_vec = 2*pi*f;
k_vec = zeros(size(omega_vec));

for i = 1:length(omega_vec)

    % Dispersion Relation == 0
    eq = @(k,omega,g,d) omega^2-g*k*tanh(k*d);

    % Calculation of Omega
    omega = omega_vec(i);

    % FindZero Function
    fun =  @(k) eq(k,omega,g,d);
    k = fzero(fun,0.00001);
    k_vec(i) = abs(k);

end

end
```

```matlab
function aPad=pad2(a,M)

% This function pads a with one zero in front and trailing zeros in the
% back to obtain a vector of length M.
% aPad = [0 a 0 0 0 0 0 ...]

if length(a)+1 > M
    disp('M too small to pad vector')
    stop
end

if iscolumn(a)
    aPad = zeros(M,1);
else
    aPad = zeros(1,M);
```

```
end

n = length(a);

aPad(1) = 0;
aPad(2:n+1) = a;

return
```

D.2. Extraction loads calculation

Here, the main script of the extraction loads calculation and all used functions are provided.

```
%% Extraction Main Script %%

% This script calculates the loads on the crane hook during the extraction
% of the monopile. The loads are due to the buoyant pile weight and the
% friction due to the embedment in sand or clay. They are presented as
% masses in the unit tons.

clear; clc;

set(0,'defaultTextInterpreter','none');
set(0,'DefaultLineLineWidth', 1);

%% Parameters

% General
g = 9.81;                                                                   % gravity constant [m/s^2]

% Environmental
d = 25;                                                                     % water depth
th_mg = 0.08;                                                               % marine growth thickness [m]
rho_sw = 1025;                                                              % sea water density [kg/m^3]
rho_mg = 1400;                                                              % marine growth density [kg/m^3]

% Foundation
rho_s = 7850;                                                               % steel density
D_o_mp = 5;                                                                 % monopile outer diameters [m]
D_o = D_o_mp+2*th_mg;                                                       % outer diameter including marine growth [m]
Dt = 80; th_w = D_o_mp/Dt; D_i = D_o_mp-2*th_w; U_i = pi*D_i;               % D/t ratio, wall thickness, internal diameter and circumference [m]
z_c1 = -5; d_c = 3;                                                         % distance of pile top below waterline and cutting depth [m]
L = d + z_c1 + d_c;                                                         % length of the pile to be removed

% Soil
beta = 0.46; gamma_s = 10e3;                                                % friction coefficient [-] and buoyant weight of sand [N/m^3]
s_u = 50e3; gamma_c = 12e3;                                                 % undrained shear strength [Pa] and buoyant weight of clay [N/m^3]

%% Calculation

% Weight of pile and soil friction

W_p = pileWeightCalc(rho_s,rho_sw,rho_mg,L,d_c,D_o,D_i,D_o_mp);
W_s = sandWeightCalc(D_o,beta,gamma_s,d_c);
W_c = clayWeightCalc(D_o,s_u,gamma_c,d_c);
```

```
function W = pileWeightCalc(rho_s,rho_sw,rho_mg,L,L_e,D_o,D_i,D_o_mp)

% This function calculates the buoyant weight of the pile that is extracted
```

```
% from the seabed.

% areas of monopile and marine growth
A = pi/4*(D_o_mp^2-D_i^2);
A_mg = pi/4*(D_o^2-D_o_mp^2);

% weight calculcation
W_p = A*L*(rho_s-rho_sw)/1000;
W_mg = A_mg*(L-L_e)*(rho_mg-rho_sw)/1000;
W = W_p + W_mg;

end
```

```
function W_s = sandWeightCalc(D_o,beta,gamma,L_e)

% This function calculates the soil friction on the pile due to it being
% extracted from sand.

Q_sfe = pi*D_o*1/2*beta*gamma*L_e^2;
W_s = Q_sfe/9810;

end
```

```
function W_s = clayWeightCalc(D_o,s_u,gamma,L_e)

% This function calculates the soil friction on the pile due to it being
% extracted from clay.

z = linspace(0,L_e);
tau = 1/2*s_u^0.75*(gamma*z).^0.25;
Q_sfe = pi*D_o*trapz(z,tau);
W_s = Q_sfe/9810;

end
```